Catalysts and Materials Development for Fuel Cell Power Generation

by

Steven E. Weiss

B. S. Chemical Engineering
University of Illinois at Urbana-Champaign, 1998

Submitted to the Department of Chemical Engineering
in Partial Fulfillment of the Requirements for the Degree of

Doctor of Philosophy in Chemical Engineering

at the

MASSACHUSETTS INSTITUTE OF TECHNOLOGY

June 2005

Author: _____
Department of Chemical Engineering
May 19, 2005

Certified by: _____
Prof. Jackie Y. Ying
Adjunct Professor of Chemical Engineering
Thesis Supervisor

Accepted by: _____
Prof. Daniel Blankschtein
Professor of Chemical Engineering
Chairman, Departmental Committee on Graduate Studies

Catalysts and Materials Development for Fuel Cell Power Generation

by

Steven E. Weiss

B.S. Chemical Engineering
University of Illinois at Urbana-Champaign, 1998

Submitted to the Department of Chemical Engineering on May 19, 2005
in Partial Fulfillment of the Requirements for the Degree of
Doctor of Philosophy in Chemical Engineering

Abstract

Catalytic processing of fuels was explored in this thesis for both low-temperature polymer electrolyte membrane (PEM) fuel cell as well as high-temperature solid oxide fuel cell (SOFC) applications. Novel catalysts were developed to generate hydrogen for PEM applications from the oxidative steam reforming of methanol. The activity of lanthanum nickel perovskite ($LaNiO_3$) was examined in both dilute fuel and full fuel conditions. Autothermal operation was successfully achieved with higher hydrogen selectivity than conventional Pd-based catalysts. The selected complex oxide catalyst was applied as a thin film onto a 0.2 μm-thick Pd membrane. Pure hydrogen effluent was obtained from the resulting microreactor as desired for PEM applications.

SOFC systems would be of interest for portable power generation if the thermal cycling and slow start-up issues could be addressed. One potential solution is the development of Si-supported ultrathin electrolyte structures (~ 100 nm-thick) of low thermal mass. Due to the low maximum fabrication temperature (< 600°C), electrodes cannot be applied by traditional ceramic processing techniques. Alternative wet-chemical approaches were explored for the electrode deposition. In particular, ceria sol-gel and yttria-stabilized zirconia (YSZ) colloid were developed as inorganic binders for cathode application at temperatures below 600°C. The YSZ sol provided adhesion strength for $La_{0.8}Sr_{0.2}Fe_{0.8}Co_{0.2}O_3$ (LSCF) in excess of 1000 psi. However, the low-temperature calcination process did not provide the LSCF cathode with sufficiently high electrical conductivity. As an alternative, porous Pt thin films with excellent conductivity were developed as the cathode for micro-SOFC applications.

To reduce the stack cost, improve the lifetime, and minimize the coking problem of hydrocarbon-based SOFC systems, it is important to reduce the operating temperature from 1000°C to 800°C. Novel anode systems were examined for their ability to process dry methane at the lower operating temperature. Specifically, three different anode formulations were developed for anode-supported SOFC architectures with 10–40 μm-thick YSZ electrolytes. These included ceramic nanocomposite anodes, $CeO_2/LaCrO_3$ and $Sm\text{-}CeO_2/La\text{-}CaTiO_3$. The former gave rise to Cr(VI) formation due to the intimate mixing of the different ceramic nanoparticles. The latter was limited in applicability due to its low electrical conductivity. Thus,

a novel cermet system, Ni-Sn/YSZ, was investigated as the anode. Unlike Ni/YSZ, it did not lead to the formation of crystalline carbon, and successfully sustained 1.5 h of methane exposure at 800°C without mechanical damage to the YSZ electrolyte. Power densities comparable to the best existing direct hydrocarbon SOFC systems were achieved by the Ni-Sn/YSZ cermet.

Thesis Supervisor: Jackie Y. Ying
Title: Adjunct Professor of Chemical Engineering

Acknowledgments

I am greatly indebted to Prof. Jackie Y. Ying for her mentoring and support. I am also grateful for the opportunity to work in her research laboratory. Very few people have the ability to gather and lead such a talented group, and I feel very lucky to have been a part of it. Indeed, the Nanostructured Materials Research Laboratory (NMRL) is unique at MIT in many regards, and I have learned many valuable lessons from Prof. Ying and my colleagues in this laboratory over the course of this thesis.

I would like to thank the members of my thesis committee, Prof. William H. Green, Jr., Prof. Jack B. Howard and Prof. Jefferson W. Tester for their advice. I appreciate the opportunity of working with Prof. Klavs Jensen, Prof. Harry Tuller, Prof. Martin Schmidt, Prof. Mark Spearing and Prof. Paul Barton on the MURI Program. I would also like to acknowledge Prof. Richard Masel for his encouragements and advice over the past two years.

I am very thankful for all my friends at MIT who made it a very special place. I would like to acknowledge the guidance from the senior members of NMRL, Dr. Larry Panchula, Dr. Andrey Zarur, Dr. Michael Wong, Duane Myers, Dr. Chen-Chi Wang, Dr. Edward Ahn, Dr. Mark Fokema, Dr. Neeraj Sangar and Dr. John Lettow for their help in getting me up to speed in the laboratory. I appreciate the chance of working with Dr. Justin McCue, Dr. Jason Sweeney, Dr. Pemakorn Pitukmanorom, Dr. Yee San Su, Dr. Suniti Moudgil, Jianyi Cui, Hong He, Noreen Zaman, Cindy Ren, Dr. Tseh-Hwan Yong and Dr. Xiaohua Huang. I thank Linda Mousseau for her assistance, and Eboney Smith and Henry Bergquist for their contribution to my research.

I would like to acknowledge Michael Frongillo, Elizabeth Shaw and Yin-Lin Xie of the MIT/NSF Center for Materials Science and Engineering for their help with the electron microscopy, X-ray photoelectron spectroscopy and furnace facilities, respectively. Financial support from the U.S. Army Research Office (MURI grant no. DAAD19-01-1-0566) and the National Science Foundation Graduate Fellowship was also greatly appreciated

Last but not least, I wish to thank Iraida Alvarez and my parents, Janet and Donald, for their love and dedication. Their patience and support have made it possible for me to successfully complete this thesis.

Table of Contents

Chapter 3 – Materials Development for Micro-Solid Oxide Fuel Cells

Chapter 4 – Novel Anode Materials for Direct Hydrocarbon Solid Oxide Fuel Cells

List of Figures

List of Tables

Chapter 1 – Background and Research Motivation

1.1. Introduction

Worldwide energy consumption is expected to grow by 54% by 2025 [1]. Both new energy sources and advanced technologies for more efficient power conversion would be needed to meet this demand. Fuel cells are of great interest as they could convert fuels directly to electricity without moving parts. They produce power from the electrochemical combustion of a stream of fuel and oxidant.

Fuel cells are being developed for many applications. They are often associated with the hydrogen economy. However, such fuel cell systems are limited by the energy density of hydrogen and the lack of fueling infrastructure. Nevertheless, two types of fuel cells are of interest for further development, polymer electrolyte membrane (PEM) and solid oxide fuel cells (SOFC). Low-temperature PEM fuel cells are applicable as battery replacements for many portable devices. High-temperature SOFC systems are targeted for combined heat power applications.

In PEM fuel cells, the polymer electrolyte conducts protons produced at the anode from hydrogen. In contrast, oxygen ions are transported in SOFC through a ceramic electrolyte (see Figure 1.1). Oxygen from the air feedstream is reduced to O^{2-} species at the cathode. The electrons required for this reduction are supplied from the oxidation of O^{2-} at the anode.

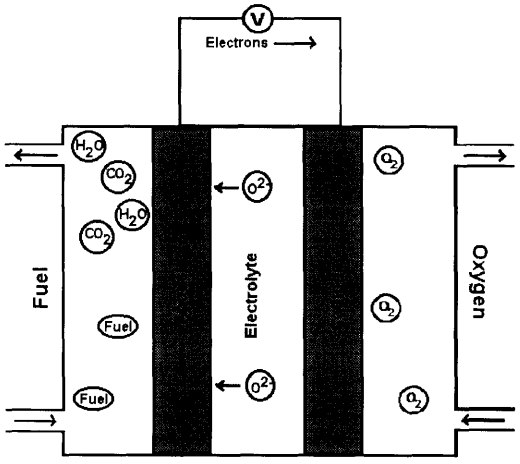

Figure 1.1. Schematic of a SOFC.

1.2. Hydrogen Generation for PEM Fuel Cells

PEM fuel cells typically require ultrapure hydrogen as a fuel. Noble metal catalysts are needed for the low-temperature oxidation involved. These materials are easily poisoned by CO. The fuel cell's power density at 0.7 V may be reduced by 45% in the presence of 50 ppm of CO [2]. As hydrogen is mainly generated from hydrocarbon reforming, this presents some challenges. Hydrogen storage has limited capacity for many applications, and successful reforming schemes typically require complicated engineering.

Portable hydrogen generators often use partial oxidation to reform hydrocarbons to hydrogen. The exothermic nature of partial oxidation also allows for rapid start-up and simpler reactor design compared to steam reforming. As partial oxidation creates large quantities of CO, the water-gas shift reaction is often employed to lower the CO concentration to acceptable levels. Copper is by far the most active metal for the water-gas shift reaction. However, dispersed copper is highly pyrophoric. Rapid reoxidation of the shift bed can result in temperature rises of 800–900°C [3]. Industrially, the shift catalyst is decommissioned slowly using 0.1% oxygen in steam over the course of 24 h. This is clearly not practical in a reactor designed for numerous on/off cycles.

Therefore, alternative catalysts should be developed for the generation of hydrogen from methanol. They would not involve expensive noble metal or pyrophoric copper catalysts. Potential catalysts were screened for high volumetric activity and tested in a plug flow reactor without a pre-reduction step. This would illustrate if these catalysts would be suitable for portable hydrogen generation. La-based perovskites were selected as the catalyst candidates. They were examined for sustained autothermal conversion of methanol to hydrogen by oxidative reforming. The optimized catalyst was also developed as a coating for application in a micro-reactor equipped with a Pd membrane, so as to demonstrate the possibility of hydrogen generation and purification in one unit operation on the micro-scale.

1.3. SOFC

SOFC systems show good power densities with hydrogen. They can also operate on hydrocarbon fuels. However, hydrocarbon utilization typically requires internal

reforming. Sufficient steam is fed with the hydrocarbon to generate hydrogen and carbon oxides over a nickel-based anode. This system suffers from mechanical problems due to the large endotherms associated with the reforming process [4]. Significant stresses are developed due to mismatch in thermal expansion coefficient between the electrolyte and electrode layers.

An unavoidable drawback of SOFC is that the fuel stream is diluted by the oxidant stream, greatly lowering the power density obtained and ultimately limiting the fuel conversion to < 80%. Higher fuel utilization would result in oxidation and spallation of the Ni/YSZ anode. As power density determines the size and the cost of the fuel cell stack required for a particular power rating, maximizing the power density would lead to a compromise in overall system efficiency. Figure 1.2 shows the decrease in the power density with increasing hydrogen utilization for one of the most advanced anode-supported fuel cells operating at 0.7 V [5].

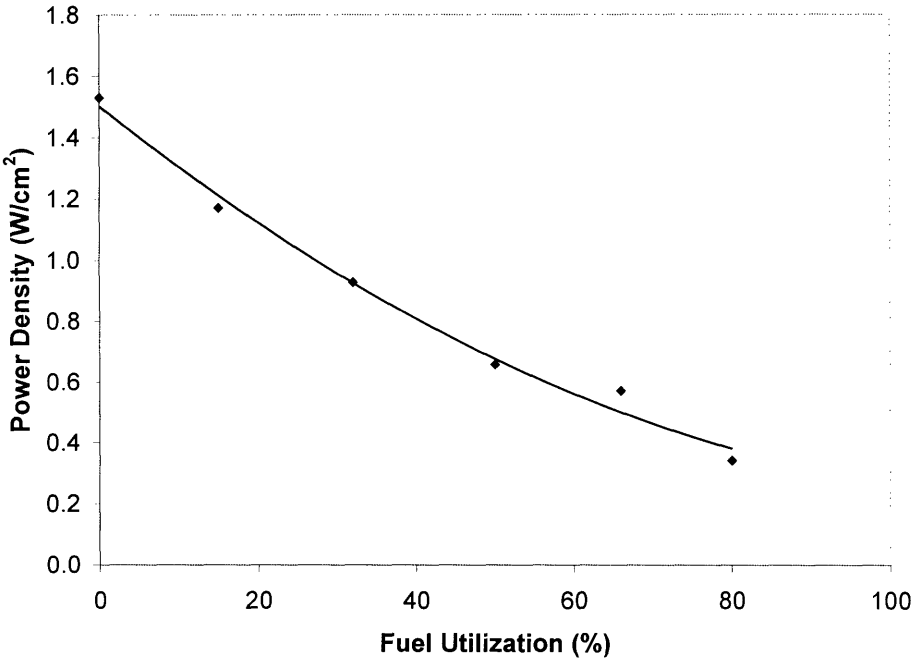

Figure 1.2. Power density versus fuel utilization for advanced anode-supported SOFC operating on hydrogen at 800°C [5].

1.3.1. Micro-Solid Oxide Fuel Cells

By miniaturizing their components, SOFC systems may be designed in a form factor capable of battery replacement for certain applications. Conventional ceramic processing techniques have produced yittria-stabilized zirconia (YSZ) electrolytes of 10–20 μm-thick. Deposition techniques used in semiconductor processing (such as sputtering, pulsed laser deposition and e-beam deposition) have enabled the generation of self-supporting YSZ electrolytes of 100–400 nm-thick. Such a dramatic decrease in electrolyte thickness would allow for lower temperature operation and reduce the system's thermal mass, greatly shortening the start-up time of the device.

Although the semiconducting processes are adept at producing dense films, they cannot generate high surface area porous electrodes easily. Therefore, wet-chemical techniques were developed for depositing electrodes for micro-solid oxide fuel cells (μSOFC). Traditional SOFC systems utilize organic binders in applying ceramic powders to the electrolytes. Calcination is then used to partially sinter the electrode layer to promote adhesion. The high temperatures involved are beyond the design limitations of the μSOFC materials. Thus, techniques for oxide wash-coats were developed to allow for low-temperature film adhesion. Besides establishing novel methods of deriving oxide-based electrodes, we have also examined approaches to create nanoporous noble metal films for low-temperature cathode applications. These systems would be of interest for their high electrical conductivity and intrinsic catalytic activity.

1.3.2. Direct Hydrocarbon Fuel Cells

Although the main attraction of SOFC systems is their ability to process many fuel streams, the fuel choice is most often a reformate stream. This is due to limitations of the current Ni/YSZ anode. When dry methane is used as the feedstream, rapid coking would cause the Ni/YSZ layer to fracture after only 10 min at 800°C. Ni metal is also not capable of being reoxidized without mechanical failure. Therefore, we have examined alternative anode-supported SOFC systems that would address these concerns through novel anode formulations.

Besides their electrochemical performance, the anode materials must have well-matched thermal expansion coefficients as the YSZ electrolyte, and must not react with

YSZ at the 1400°C fabrication temperature. Three different anode materials were investigated. The first two anode materials utilized all-ceramic formulations, and could be reoxidized. In the first case, $La_{1-x}Sr_xCr_{1-y}Mg_yO_3$ and doped ceria were used as the electrical conduit and ionic conductor, respectively, to form a composite mixed conductor. To maximize the active interface between the doped ceria and lanthanum chromate, the two ceramics were processed as a nanocomposite instead of a physical mixture. Besides this system, we have examined a second all-ceramic system, which consisted of an electrically conductive La-doped $CaTiO_3$ and doped ceria.

The third anode material studied was Ni-Sn/YSZ. This cermet utilized a Ni-Sn alloy to minimize the coking problem. Its coke resistance and dimensional stability in dry hydrocarbon were compared to those of the conventional Ni/YSZ system. The resulting anode-supported SOFC was examined for operations involving humidified hydrogen and humidified methane.

1.4. References

[1] International Energy Outlook 2004, DOE/EIA-0484 (2004).
[2] Fuel Cell Handbook 6, DOE/NETL-2002/1179 (2002).
[3] Twigg, M.V., "Catalyst Handbook Second Edition," p. 330, Manson Publishing, London, 1996.
[4] Achenbach, E., *J. Power Sources* **49**, 333 (1994).
[5] Virkar, A.V., "Polarization in Anode-Supported Solid Oxide Fuel Cells," Boston University Emerging Technology Seminar, May 30, 2003.

Chapter 2 – Nanocrystalline Perovskites for Oxidative Steam Reforming of Methanol

2.1. Introduction

Due to current limitations in battery technology, polymer-based fuel cells are developed to provide high power densities from hydrogen fuel. Unlike stationary reactors, portable reforming systems must utilize a fuel that can produce pure hydrogen in a minimal number of unit operations. Methanol is an ideal fuel for such application. It has a high energy density, is a liquid available free of impurities, and can be reformed easily at temperatures below 400°C.

The low-temperature water-gas shift catalyst can be employed to produce hydrogen from methanol steam reforming [1]. The water-gas shift reaction increases the hydrogen yield of reformate streams at the expense of CO. The copper-based catalyst for this reaction suffers from the exothermicity of the reduction step; when rapidly reduced with hydrogen, a temperature rise of 500°C may be experienced. When rapidly shut down in air, an uncontrolled oxidation can produce temperatures of 800–900°C due to the pyrophoric nature of the copper catalysts [2]. These exotherms can be avoided industrially using slow reduction and oxidation steps, but such operations would not be practicable in portable reforming applications. Thus, a novel catalyst system is needed to work stably under transient operations and frequent reactor cycling.

Additional challenges exist for portable power applications. First, hydrogen is not typically available to pre-reduce the traditional reforming and water-gas shift catalysts. Secondly, a CO remediation technique must be employed to keep CO levels below 100 ppm throughout the reactor lifetime [3]. Lastly, a high degree of system integration is needed to ensure a small form factor.

Methanol partial oxidation is the focus of this study due to its quick start-up and autothermal operation. Steam may be added to the methanol feed to boost the hydrogen selectivity, while lowering the maximum reaction temperature [4]. Various classes of metal catalysts were screened for volumetric activity with the constraint that the system might not utilize a pre-reduction step, and should not contain significant quantities of copper or noble metals. The optimized catalyst systems were then applied to a Si-based microreactor with a Pd membrane for the production and purification of hydrogen in one unit operation. Problems associated with the oxidation and methanol poisoning of the Pd membrane were avoided by utilizing a uniform active catalyst coating.

2.1.1. Classification of Methanol Reaction Schemes

Hydrogen can be produced from methanol by steam reforming, partial oxidation, or endothermic dissociation. The steam reforming reaction is preferred because it has the highest fuel efficiency and produces the least CO.

$$CH_3OH_{(g)} + H_2O \rightarrow 3\ H_2 + CO_2 \qquad (1)$$

The high efficiency results from the water-gas shift reaction, which combines CO and excess water to produce hydrogen and carbon dioxide. Steam reforming is endothermic, and has a slower reaction rate compared to partial oxidation [5]. Typical industrial catalysts for methanol steam reforming are copper-zinc oxide supported on alumina.

Partial oxidation of methanol is exothermic, and can produce hydrogen without an external heat supply [6]. The reaction scheme includes the decomposition of methanol to CO and hydrogen, followed ideally by the selective oxidation of CO.

$$CH_3OH_{(g)} + \tfrac{1}{2}\ O_2 \rightarrow 2H_2 + CO_2 \qquad (2)$$

This reaction [7] is not as well studied as steam reforming. The most active catalysts are supported copper and palladium.

Endothermic dissociation of methanol can be used to produce synthesis gas. An additional step would be required to convert the high CO content.

$$CH_3OH_{(g)} \rightarrow 2\ H_2 + CO \qquad (3)$$

Supported molten salt catalysts have shown great stability for this reaction [8]. Other catalysts for this reaction include copper/chromia.

2.1.2. Reforming Catalysts

Nickel metal catalysts are typically used in the reforming of hydrocarbons. They can be difficult to reduce, especially when supported on alumina. Their reduction is performed with hydrogen at temperatures above 600°C. Noble metal catalysts are more active and expensive than the nickel catalysts. The reforming activity with toluene as the model reactant is given by Rh > Ir > Pt > Ru. In general, active reforming catalysts would show little activity for the water-gas shift reaction [9].

The high-temperature shift catalyst is iron/chromia. The active species is magnetite (Fe_3O_4), which is formed from the reduction of haematite (Fe_2O_3). The catalyst must not be

over-reduced to FeO and metallic iron, which are less active. This system can be operated at 340–400°C, and would sinter at higher temperatures. The reduced catalyst is also pyrophoric, and re-oxidation can lead to an adiabatic temperature rise of 450°C. Therefore, re-oxidation is industrially performed slowly in a dilute air stream at low temperatures [2].

The modern copper-based low-temperature shift catalyst was introduced in 1960, and has been optimized to improve the thermal stability and poisoning resistance [10]. It is operated below 260°C to limit copper sintering. Industrially, its reduction is performed over a period of 12–24 h to prevent catalyst over-heating. Before discharge, the catalyst is re-oxidized with a dilute (0.1%) air stream so that the heat produced may be removed safely [2]. These controlled reduction/oxidation steps are not feasible in a cyclic portable system. The danger of large exotherms would prevent copper from being used as the primary catalyst component in portable reforming.

2.1.3. Catalyst Design

Although high hydrogen selectivity is desired, methanol steam reforming and water-gas shift reactions are not likely to be utilized in a compact portable system since they require copper-based catalysts. The low-temperature activity of copper towards the shift reaction is quite unique [11]. Therefore, our attention is turned towards partial oxidation of methanol.

Traditionally, noble metal systems are utilized for the partial oxidation reaction as they facilitate light-off and ensure continued autothermal operation. However, their cost is too prohibitive for most applications. This study focuses on non-noble metal combustion catalysts that belong to the perovskite family. These catalysts are employed in an oxygen-poor environment to limit complete oxidation.

CO mitigation for this application has been addressed industrially by using excess oxygen feed. Casio has presented a clean-up bed with an O_2/CO ratio of 40 [12]. Such a high excess air concentration significantly dilutes the fuel content entering the fuel cell. Alternatively, selective CO oxidation has been explored. These occur optimally below room temperature, and therefore are not realistic [13]. In this study, a palladium membrane is employed at the reaction temperature to remove CO from the reformate stream.

2.2. Experimental

2.2.1. Reactor Design and Reaction Conditions

A packed bed reactor was constructed to study the partial oxidation of methanol. Vaporization of low levels of steam and methanol could lead to substantial feed fluctuations. Such fluctuations were reduced to 5% by using a heated dead volume after the pre-heater. The oxygen stream was introduced post the dead volume to avoid possible reactions within the dead volume; blank runs indicated no conversion up to a furnace temperature of 600°C. Liquid reactants were introduced using a Harvard Apparatus syringe pump. Gas flow rates were controlled with MKS mass flow controllers. The reactor effluent was analyzed after a condenser using an Agilent 6890 gas chromatograph equipped with a mole-sieve and Carbowax columns. Reaction temperature was controlled with a thermocouple inserted just below the catalyst bed.

Nitrogen was added to the carrier gas as an inert standard to allow for accurate determination of the product distribution. Methanol feed concentration was fixed at 5% in the catalyst development studies. This level represented a good compromise that provided a uniform feed stream. Lower methanol concentrations would be desirable to further reduce the possibility of heat effects, but they would lead to unacceptably large data fluctuations.

For catalytic studies, the oxygen/methanol ratio was set at 0.3 to minimize heat effects due to the reaction. The steam/methanol ratio was 1.5. Under these conditions, catalytic activities were initiated at 400°C, and then brought to lower temperatures. Catalysts were pelletized and crushed to 60–80 mesh before testing. All runs utilizing a 5% methanol feed involved 75 mg of catalysts kept between quartz wool plugs. For the perovskite catalysts, this corresponded to a space velocity of 500,000 hr^{-1}. Optimized catalysts were compared to a commercial 5 wt% Pd/Al_2O_3 catalyst (Sigma). Following the convention of this field, hydrogen selectivity was based on the stoichiometry of partial oxidation [14]. If significant water-gas shift activity was present, the hydrogen selectivity could exceed 100%.

Full-fuel conditions were studied to examine both the exothermicity of the reaction and the ability of non-noble metal catalysts to sustain autothermal conversion. A liquid fuel with a water/methanol ratio of 3 was utilized to keep the stock solution non-flammable. A simulated air stream was used whereby nitrogen was replaced by 4% nitrogen in helium, and blended with pure oxygen to allow for evaluation of the mass balance. The catalyst powders were pelletized and sieved to a 60–80 mesh. The reactor was a ¼" quartz tube with the reactants fed either as a

liquid at room temperature or as a preheated gas at 140°C. A syringe pump was used to feed the liquid precursors through the low-volume 1/16" stainless steel tubing.

Reactions in the microreactor with palladium membrane utilized a bubbler to introduce the feed as the flow rates were ~ 10 sccm. Both chilled and room-temperature saturators were employed to produce methanol concentrations of 4% and 13%, respectively. A helium sweep was used on the permeate side, and the reformate was analyzed using a mass spectrometer. Details on the fabrication of the microreactor were published elsewhere [15].

2.2.2. Synthesis and Characterization of Catalysts

Catalysts were synthesized by techniques previously reported [16]. In general, a salt solution of the desired composition was added slowly to a base solution consisting of tetraethylammonium hydroxide (Alfa Aesar) in isopropanol. After aging, the precipitate was rinsed with isopropanol, dried and calcined to 800°C. The tetraethylammonium hydroxide was used in place of sodium hydroxide in this synthesis to avoid sodium contamination.

Catalyst coatings for the microreactor were obtained by dispersing the calcined and milled powder in methanol using a sonicator. Prior to application, a blend of catalyst and alumina (Nyacol, 50 nm) (8:1 weight ratio) was used to bind the oxide to the microreformer membrane.

X-ray diffraction (XRD) patterns of the catalysts before and after reaction were obtained with a Siemens D5000 Diffractometer (45 kV, 40 mA, Cu-Kα). Surface areas were measured using a 5-point BET (Brunauer-Emmett-Teller) method on a Micromeritics ASAP 2000 instrument. Temperature-programmed reduction was performed in a Perkin-Elmer Series 7 TGA with 2.5% hydrogen in helium at 300 sccm.

2.3. Results and Discussion

2.3.1. Thermodynamics of Oxidative Steam Reforming

Since low-temperature PEM fuel cells could be easily poisoned by CO, thermodynamics were used to understand the effect of reaction conditions on CO production. Where possible, purification processes should be avoided if the reaction conditions would allow for sufficient CO mitigation. The reaction thermodynamics were examined with the non-stoichiometric method. The heat and entropy of formation and the heat capacity for the various gases were taken from

the NIST database. All gases were considered ideal. Thermodynamics of methanol steam reforming have been published previously [17], but thermodynamics of oxidative steam reforming have not been reported.

In the partial oxidation regime without water addition, methanol conversion was complete above a temperature of 230°C. As the temperature increased, the selectivities to CO_2 and hydrogen decreased, which could be attributed to the slight exothermicity of the water-gas shift reaction. Numerous species were involved in the original model, including methane, carbon, methyl formate and dimethyl ether. Figure 2.1(a) shows the results of the full model at 600 K and 1 bar for various methanol concentrations in air. 12.3 mol% methanol feed corresponded to stoichiometric combustion, while 100% methanol feed corresponded to methanol dissociation. The major species produced at low oxygen contents were water, carbon and methane in the full thermodynamic model. Methanol was known not to coke as its C-O bond would not be broken through heterogeneous reactions [18]. Methane, however, has been observed in some reaction schemes in sub percent quantities, and was produced through a methanation mechanism [19]. As a result, a simplified model was examined that included only the main species: hydrogen, water, CO, carbon dioxide, methanol and nitrogen (Figure 2.1(b)).

A wide range of oxygen and water ratios was studied to understand the effect of having these two reactants in the same bed (see Figure 2.2). A grid of conversions was calculated at oxygen/methanol ratios of 0.00–0.75, and water/methanol ratios of 0–3. The reaction was examined at 1 bar and 500, 600, 700 and 800 K. An additional grid of data was taken at 5 bars and 600 K to determine the pressure effects. Such effects were minor and did not provide sufficient CO remediation.

High water/methanol ratios were favorable towards maximizing hydrogen and minimizing CO production. The presence of oxygen lowered hydrogen selectivity, but helped CO remediation. In general, water/methanol ratios should be > 1, with sufficient oxygen levels to keep the process exothermic for autothermal operation (O_2/methanol ratio > 0.3). However, it was not possible to keep the CO levels below 100 ppm under the conditions investigated. This meant that excessively high water and/or oxygen contents would have to be introduced to the feed to lower the CO levels. High water contents would not be feasible since a large amount of energy would be needed to vaporize the feed stream. The reformate would also be diluted with steam, reducing the hydrogen content in the product stream. Thus, to meet the requirements of

PEM fuel cells, a Pd-based membrane purifier was chosen over a chemical means for CO removal.

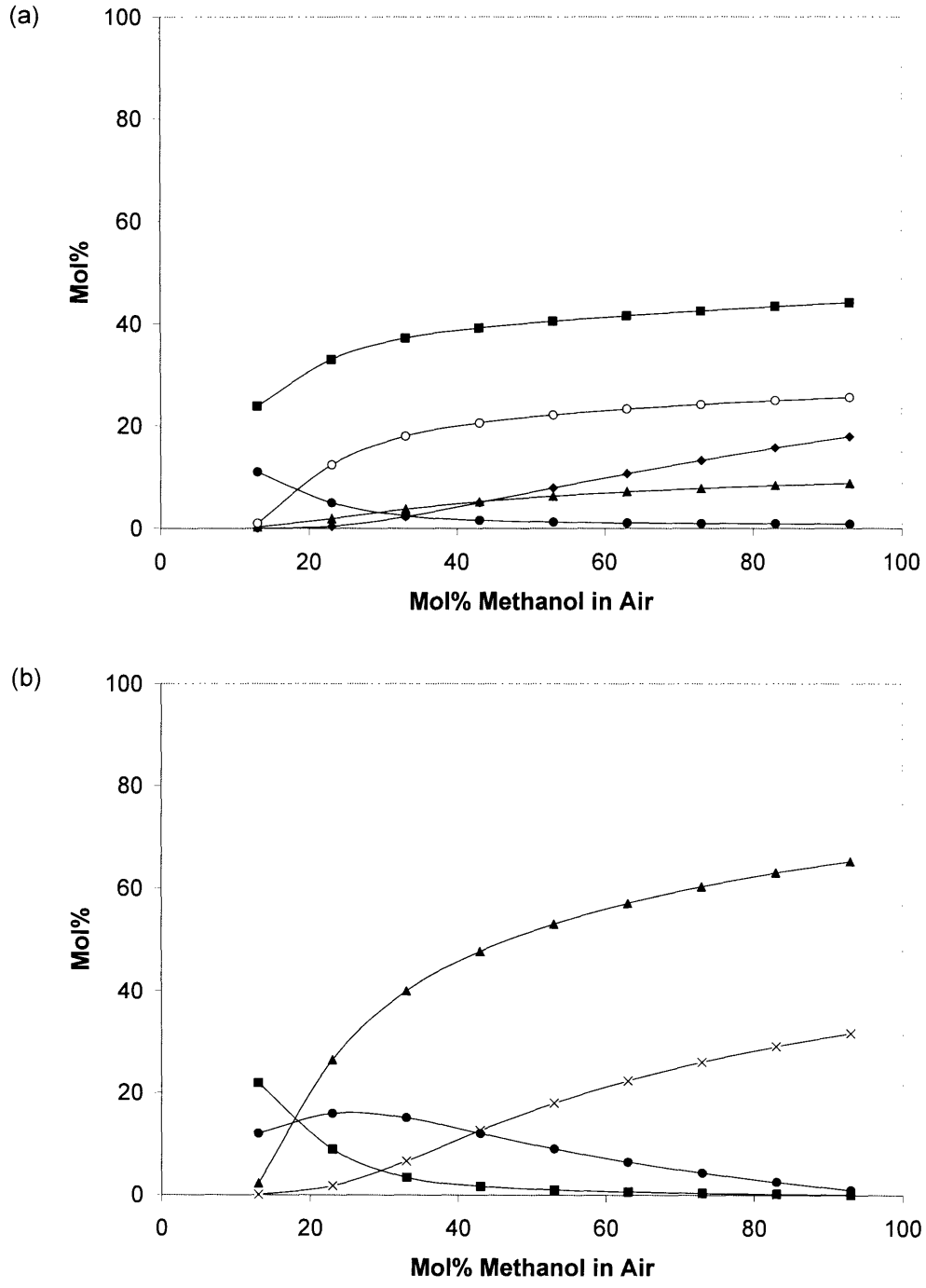

Figure 2.1. (a) Full and (b) simplified thermodynamics model of methanol reaction in air to produce (■) H_2O, (▲) H_2, (♦) CH_4, (●) CO_2, (○) carbon and (×) CO at 600 K and 1 atm.

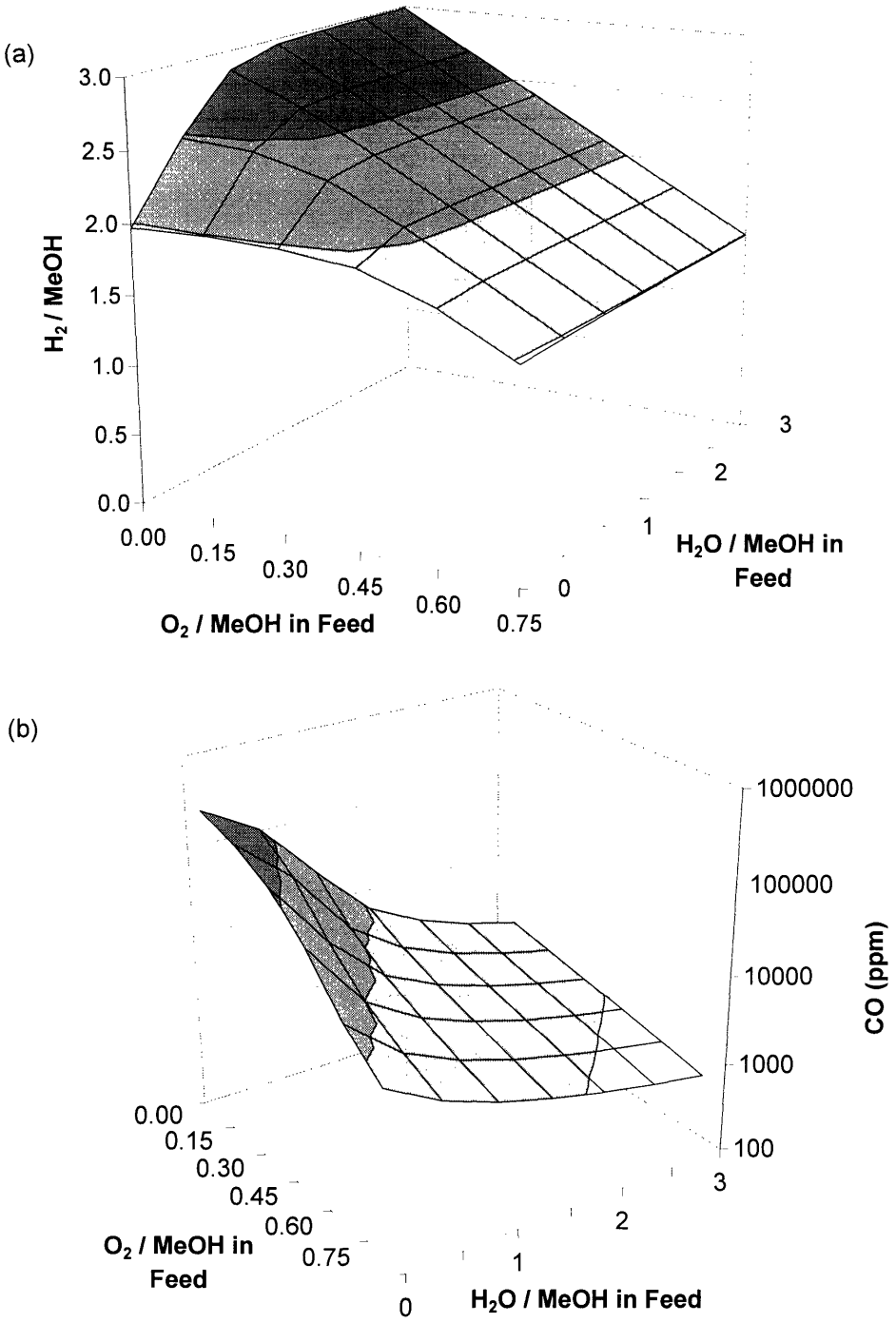

Figure 2.2. Thermodynamics model of oxidative steam reforming of methanol at 500 K and 1 bar.

2.3.2. Adiabatic Temperature Rise

The maximum possible temperature rise was evaluated to understand the effect of various feed conditions on the reaction temperature. Short contact time exothermic partial oxidation reactions approach the adiabatic conditions [20]. For comparison, stoichiometric partial oxidation of methane has a heat of reaction of -36 kJ/mol. Methanol partial oxidation has a much larger heat of reaction of -192 kJ/mol, and a larger flammability window in air.

To obtain an upper bound on the reaction temperature, the adiabatic temperature rise was calculated based solely on oxidation mechanisms. The slower endothermic dissociation and steam reforming reactions were not involved in the calculation as they would not have time to reach equilibrium at the space velocities typically employed [14]. Complete CO oxidation was calculated prior to hydrogen consumption as CO oxidation was more exothermic than hydrogen oxidation. The lower bound of perfect hydrogen oxidation selectivity reduced the curves slightly, but did not alter the results considerably.

Figure 2.3(a) was based on feeding gaseous reactants at 140°C, with air as the oxygen source. Figure 2.3(b) involved liquid feed stream and used the exothermicity of the reaction to vaporize the reactants *in situ* at the reaction zone. Some researchers have utilized a liquid feed to help cool this reaction and limit the bed temperature [4].

In vitiated air, hydrogen would ignite at 610°C, while CO and methanol would ignite at 758°C and 820°C, respectively [21]. Thus, when the reaction temperature exceeded these temperatures, homogeneous combustion of hydrogen would be expected. Commercially, the Johnson Matthey HotSpot reactor utilizes the presence of large exotherms to quickly reduce methanol concentrations [22]. However, if a water-gas shift bed is not employed, heat must be removed from the reactor to minimize the occurrence of homogeneous reactions and the loss of hydrogen selectivity.

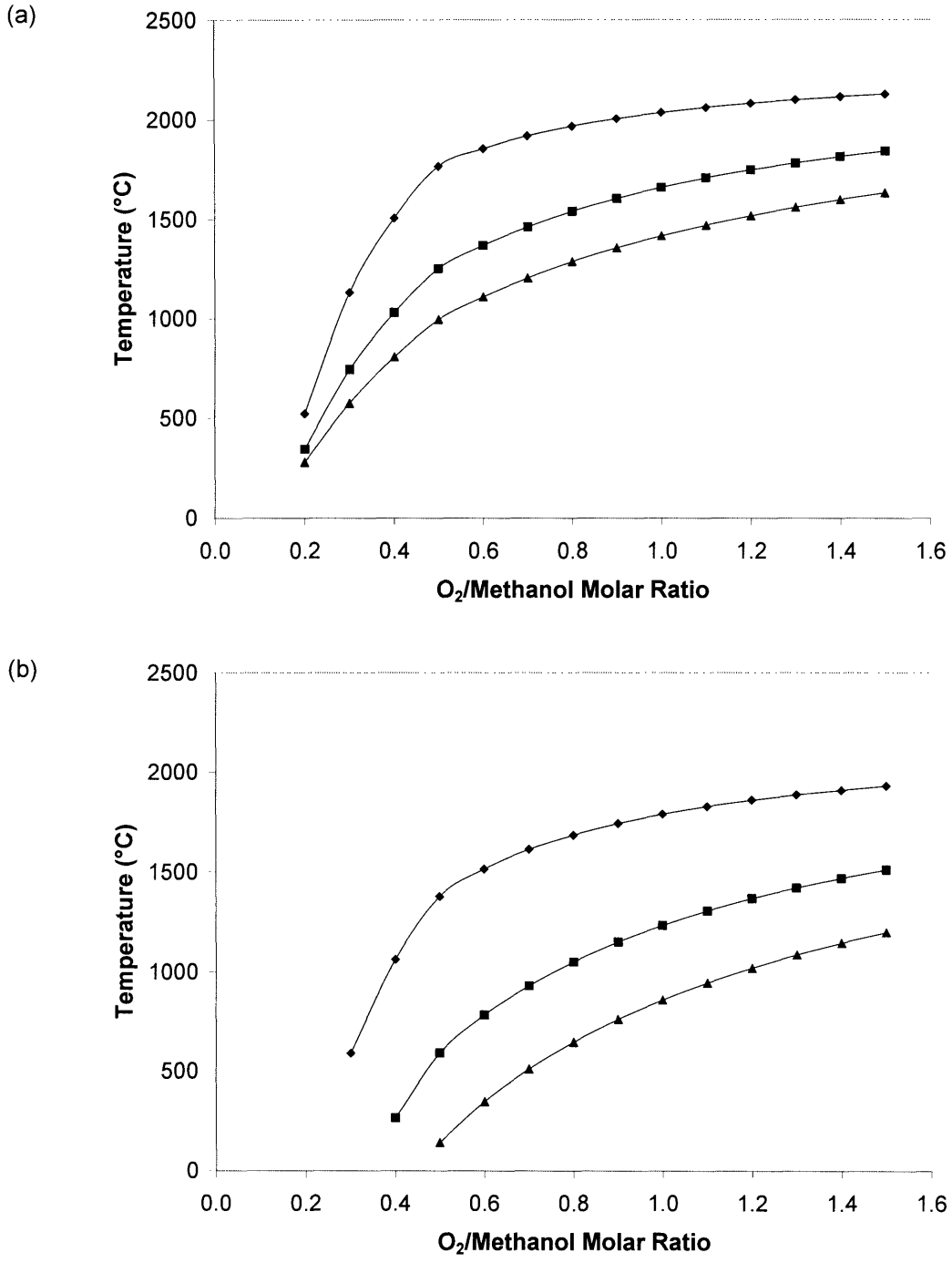

Figure 2.3. Adiabatic temperature rise with (a) preheated gaseous reactants at 140°C, and (b) liquid reactants, using a water/methanol molar ratio of (♦) 0.0, (■) 1.5 and (▲) 3.0 with air as the oxygen source.

2.3.3. Preliminary Studies

Many classes of materials were screened for the partial oxidation of methanol without water addition. Initial studies examined the activity of copper catalysts, which performed quite well but showed significant deactivation over time. A simple comparison of copper- and nickel-based catalysts were performed by synthesizing copper and nickel aluminates with excess transition metal content (M/Al = 0.625). These two aluminates were examined at 325°C due to the low-temperature constraint of the copper-based catalyst (see Figure 2.4).

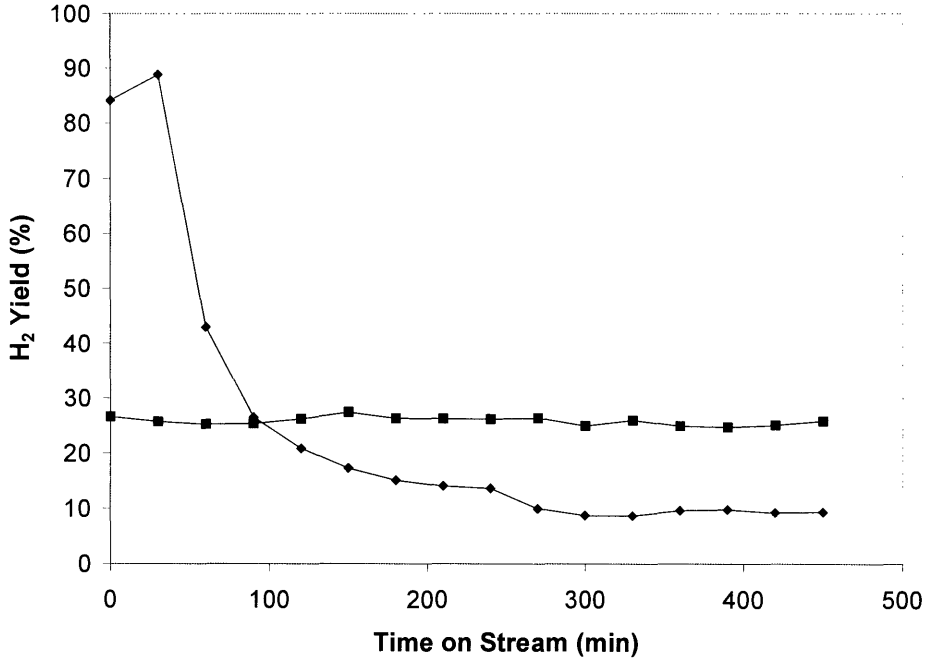

Figure 2.4. Hydrogen yield for methanol partial oxidation without steam at 325°C over (♦) copper aluminate and (■) reduced nickel aluminate at 200,000 hr^{-1} with a 5% methanol feed and an oxygen/methanol molar ratio of 0.3.

Nickel aluminate has been successfully used for the steam reforming of methane [23]. However, it could not be reduced by methanol at the reaction temperature, and the unreduced catalyst produced dimethyl ether possibly over the acidic alumina sites. When nickel aluminate was reduced with hydrogen at high temperatures prior to catalytic testing, it produced dimethyl ether and hydrogen. After reaction, the catalyst could be exposed to air and re-used without another reduction step.

The nickel aluminate catalyst was found to be much more stable than the copper aluminate catalyst. Better copper-based catalysts were synthesized, but they all exhibited rapid

deactivation over time. In particular, barium was found to be an active promoter for this reaction [24]; copper/ceria also performed well [25]. These copper-based catalysts all led to high initial hydrogen yields, but could not achieve stable activity.

2.3.4. The La-based Perovskite System

The best non-noble metal catalyst developed by us belonged to the perovskite family. Perovskites (ABO_3) have a complex crystal structure that accommodated a great variety of compositions. Lanthanum was used for the A-site since La-based perovskites have been applied as combustion catalysts with good light-off characteristics and thermal stability [26]. Nickel, iron, cobalt and manganese were used at the B-site, which could be further doped to improve the catalyst stability in reducing atmospheres.

The La-based perovskites showed that their activity towards methanol partial oxidation was heavily dependent on the B-site composition (Figure 2.5). Superior hydrogen yield was attained by $LaNiO_3$, which demonstrated full methanol conversion under the conditions tested with a hydrogen/methanol molar ratio of 2. Only CO_2, CO, H_2 and H_2O were obtained over the $LaNiO_3$ and $LaCoO_3$ catalysts; no methane or dimethyl ether was observed. Though active for methanol conversion, $LaMnO_3$ produced only combustion products with negligible hydrogen yield.

For reference, a $NiO/NiAl_2O_4$ catalyst was also shown in Figure 2.5. It contained the same Ni loading by weight as the $LaNiO_3$ catalyst and was not pre-reduced. As noted in Section 2.3.3, the unreduced $NiO/NiAl_2O_4$ only produced dimethyl ether in the absence of water. Introduction of steam decreased the dimethyl ether yield, and resulted in hydrogen production with high carbon dioxide selectivity.

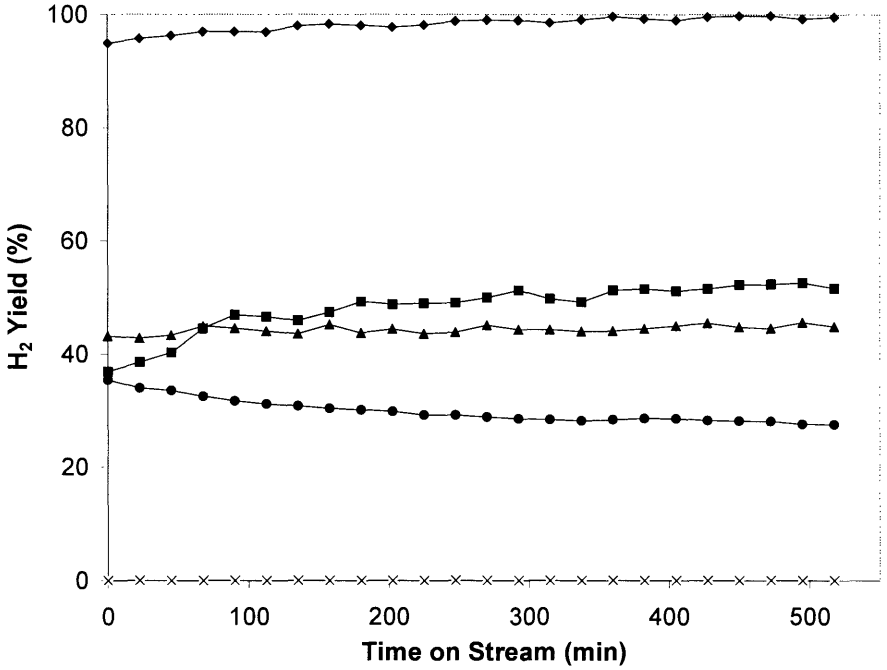

Figure 2.5. Hydrogen yield for methanol partial oxidation at 400°C over (♦) $LaNiO_3$, (■) $LaCoO_3$, (▲) $LaFeO_3$, (×) $LaMnO_3$, and (●) $NiO/NiAl_2O_4$. The reaction was conducted at a space velocity of 500,000 h^{-1} with a 5% methanol feed, a water/methanol molar ratio of 1.5, and an oxygen/methanol molar ratio of 0.3.

2.3.5. Effect of Reaction Environment on $LaNiO_3$

To understand what reaction processes occurred over the $LaNiO_3$ perovskite catalyst, the effect of reaction environment was investigated (see Figure 2.6). This catalyst showed the highest activity for the methanol partial oxidation; steam lowered the activity of methanol partial oxidation at low temperatures. $LaNiO_3$ was less active for the dissociation and steam reforming of methanol. However, since these two endothermic reactions would occur under the reaction conditions, they were expected to contribute towards the observed selectivities.

The ability of steam to increase the selectivity of the partial oxidation reaction is illustrated in Figure 2.7. At 400°C, the CO selectivity rose from 33% to 64% in the presence of steam. This suggested a significant contribution from the water-gas shift reaction to the selectivity observed at a feed oxygen/methanol molar ratio of 0.3. Further increase in the oxygen/methanol molar ratio would decrease the CO selectivity, but CO was never eliminated in the partial oxidation reaction. At the stoichiometric oxygen/methanol molar ratio of 0.5, the carbon dioxide selectivity only rose to 84%, but the hydrogen selectivity decreased to 91%. At

the high space velocities employed, the ability of the water-gas shift reaction to move the system towards equilibrium was limited [14].

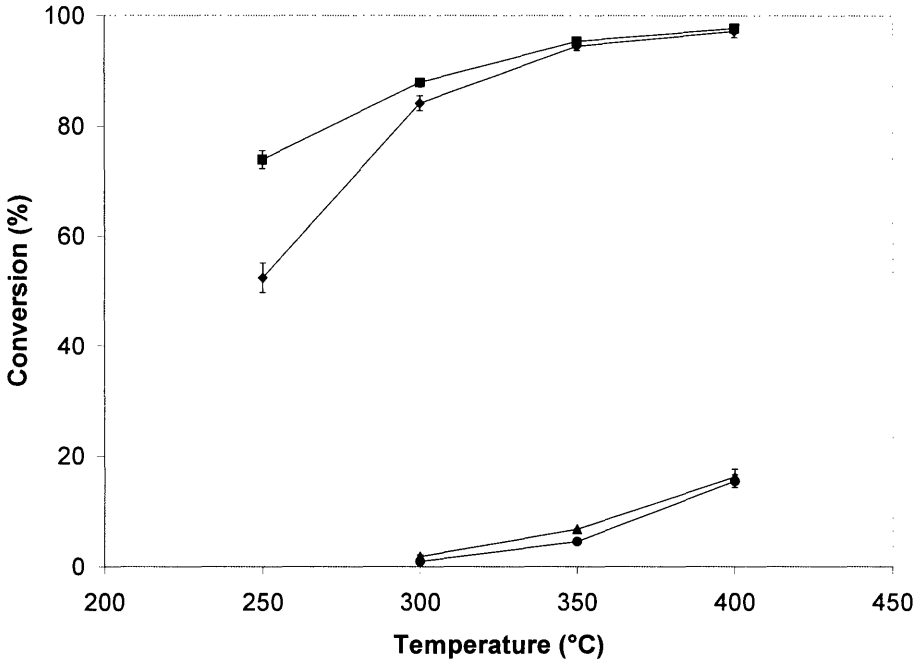

Figure 2.6. Conversion of methanol over $LaNiO_3$ for a feed stream containing (■) 5% methanol and 1.5% oxygen, (♦) 5% methanol, 1.5% oxygen and 7.5% H_2O, (▲) 5% methanol, and (●) 5% methanol and 7.5% H_2O.

The effect of high temperature and hydrogen generation on the perovskite catalyst was examined. Some surface reduction of $LaNiO_3$ to nickel metal might be desirable for the water-gas shift and steam reforming reactions. To elucidate its oxidation state under various reaction conditions, the catalyst was characterized after the reaction was quenched by a helium stream at 400°C. X-ray photoelectron spectroscopy (XPS) analyses (Kratos AXIS Ultra Imaging X-ray Photoelectron Spectrometer) were inconclusive since the main nickel peak, Ni $2p_{3/2}$, overlapped with the La $3d_{3/2}$ peak [27]. XRD showed no bulk nickel phase formation after the catalyst was subjected to different reactions (Figure 2.8). The catalyst remained similar in grain size and crystal structure after the oxidative steam reforming reaction (Figure 2.8(c)). Upon exposure to methanol and steam at 400°C, the catalyst transformed to the brownmillerite phase, $La_2Ni_2O_5$, which has a partially reduced perovskite structure (Figure 2.8(b)). The greatest phase change in $LaNiO_3$ was noted after the methanol partial oxidation, which gave rise to lanthanum carbonate

formation (see Figure 2.8(a)). In this case, the grain size of the remaining $LaNiO_3$ perovskite crystals was only 8 nm, significantly reduced from the 31 nm grain size of the fresh catalyst.

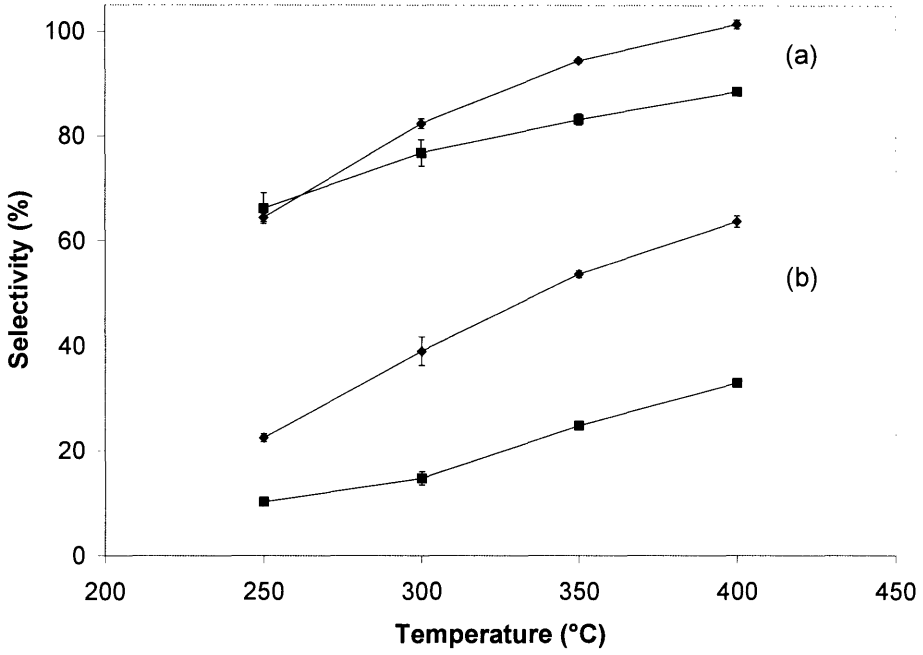

Figure 2.7. (a) Hydrogen and (b) CO selectivities for methanol partial oxidation over $LaNiO_3$. The reaction was conducted at a space velocity of 500,000 h^{-1} with a 5% methanol feed, a water/methanol molar ratio of (♦) 1.5 and (■) 0.0, and an oxygen/methanol molar ratio of 0.3.

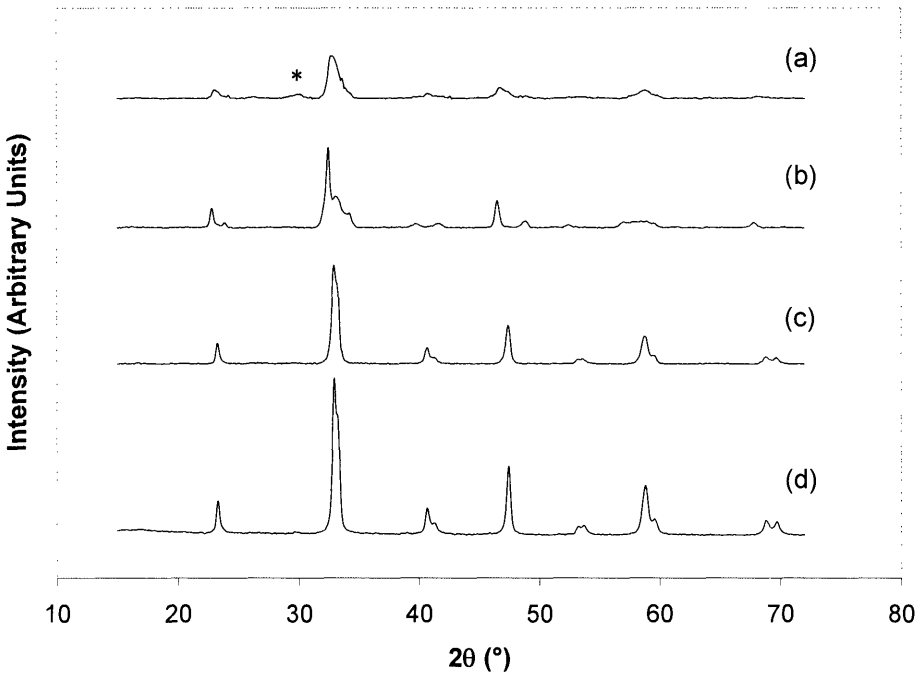

Figure 2.8. XRD pattern of $LaNiO_3$ after subjected to 400°C reaction with a feed of (a) 5% methanol and 1.5% oxygen, (b) 5% methanol and 7.5% H_2O, and (c) 5% methanol, 1.5% oxygen and 7.5% H_2O. XRD pattern of fresh $LaNiO_3$ catalyst is shown in (d). XRD peak for the main lanthanum carbonate peak is denoted by *.

2.3.6. Effect of Dopants on the Stability and Reactivity of $LaNiO_3$

To improve the stability of $LaNiO_3$, 25 cation% doping of the B-site with Mn, Fe and Al was carried out. Figure 2.9 shows that Al doping led to the greatest stability against reduction; this might be associated with its ability to stabilize the brownmillerite phase [28]. Mn and Fe doping also improved the stability of $LaNiO_3$.

The high-temperature stability of $LaNiO_3$ and $LaNi_{0.75}Al_{0.25}O_3$ to hydrogen was examined. After exposure to 5% hydrogen at 650°C for 6 h, nickel formation was noted in both catalysts (see Figure 2.10). XRD analyses indicated an average nickel grain size of 14 nm and 4 nm, respectively. Complete reduction of perovskite was not desired since large nickel grains would be produced due to the high nickel loading [29]. For applications above 650°C, aluminate supported nickel species might be preferred to the perovskite catalyst.

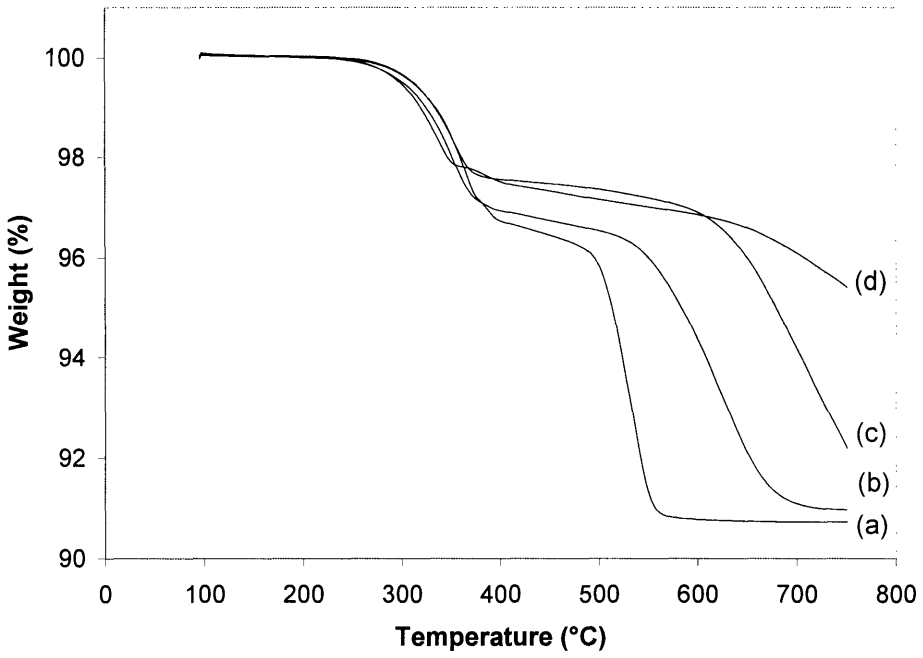

Figure 2.9. Temperature-programmed reduction of (a) $LaNiO_3$, (b) $LaNi_{0.75}Mn_{0.25}O_3$, (c) $LaNi_{0.75}Fe_{0.25}O_3$, and (d) $LaNi_{0.75}Al_{0.25}O_3$.

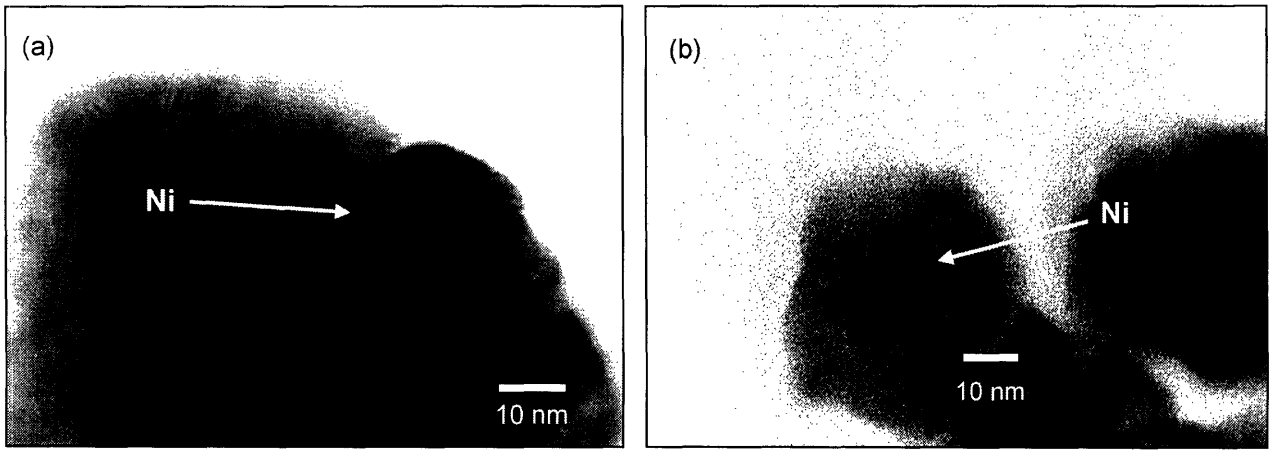

Figure 2.10. Transmission electron micrograph (JEOL 2010, 200 kV) of (a) $LaNiO_3$ and (b) $LaNi_{0.75}Al_{0.25}O_3$ after exposure to 5% hydrogen for 6 h at 650°C.

$LaNi_{0.75}Al_{0.25}O_3$ stability was tested for methanol partial oxidation in the absence of steam (see Figure 2.11). Its grain size decreased from 30 nm to 13 nm after the reaction. However, unlike $LaNiO_3$, $LaNi_{0.75}Al_{0.25}O_3$ did not give rise to large lanthanum carbonate formation. Higher levels of Al doping might be needed for long-term catalyst stability towards methanol partial oxidation without steam. However, since the catalyst selectivity and stability

were shown to be greatly improved in the presence of steam, oxidative steam reforming would be preferred to partial oxidation, and we would not have to be concerned with high levels of Al doping.

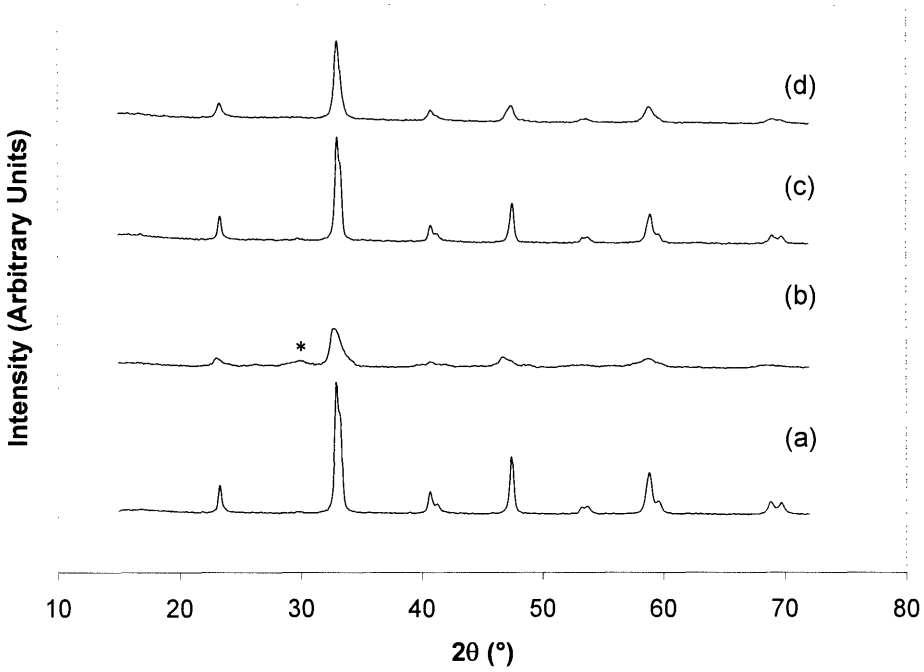

Figure 2.11. XRD pattern of (a,b) $LaNiO_3$ and (c,d) $LaNi_{0.75}Al_{0.25}O_3$ (a,c) before and (b,d) after methanol partial oxidation at 400°C without steam addition. The main lanthanum carbonate peak is denoted by *.

The activity of $LaNi_{0.75}Al_{0.25}O_3$ was compared to $LaNiO_3$ in the oxidative steam reforming of methanol (see Figure 2.12). The Al-doped catalyst had difficulty sustaining the reaction at 250°C; it also lowered the selectivities towards hydrogen and carbon dioxide. To improve the low-temperature activity of $LaNiO_3$, Co doping was employed. $LaNi_{0.95}Co_{0.05}O_3$ exhibited a much higher surface area (28 m^2/g) than $LaNiO_3$ (8 m^2/g). It gave rise to increased conversion, as well as superior selectivities towards hydrogen and carbon dioxide (Figure 2.12). Its hydrogen selectivity clearly exceeded 100% at $\geq$ 350°C, indicating a high activity for the water-gas shift reaction. Such increase in hydrogen selectivity was not observed when the Co doping level was increased to 10 cation% or higher.

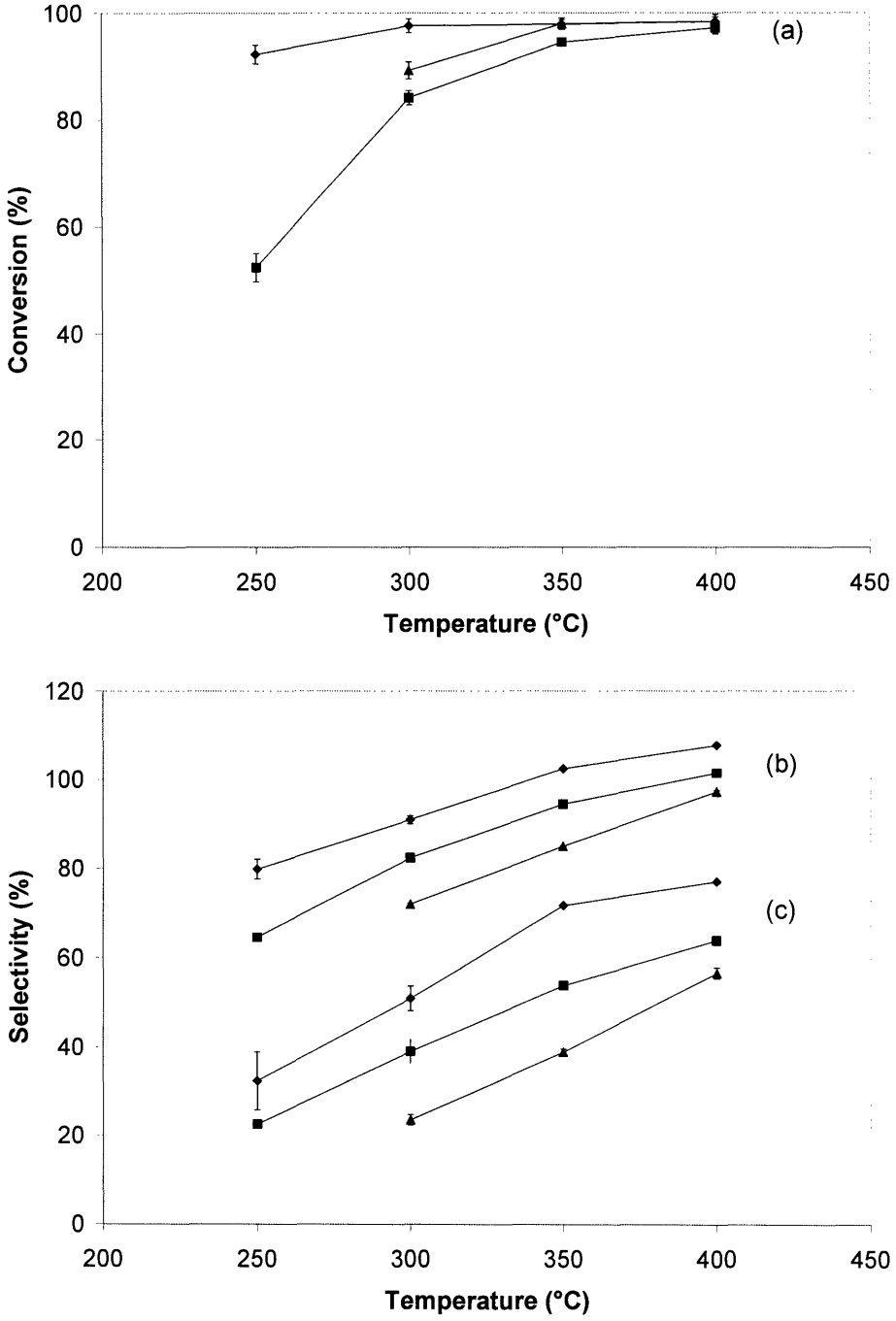

Figure 2.12. (a) Conversion, and (b) hydrogen and (c) carbon dioxide selectivities for oxidative steam reforming of methanol over (■) $LaNiO_3$, (▲) $LaNi_{0.75}Al_{0.25}O_3$, and (♦) $LaNi_{0.95}Co_{0.05}O_3$. The reaction was conducted at a space velocity of 500,000 h^{-1} with a 5% methanol feed, a water/methanol molar ratio of 1.5, and an oxygen/methanol molar ratio of 0.3.

2.3.7. Comparison to Noble Metal System

The optimized perovskite catalyst, $LaNi_{0.95}Co_{0.05}O_3$, was compared to commercially available noble metal catalyst, 5 wt% Pd/Al_2O_3 [30]. The latter lighted off easily with the preheated gaseous feed stream, whereas the perovskite systems only showed activity at 250°C or above (see Figure 2.13).

$LaNiO_3$ and $LaNi_{0.95}Co_{0.05}O_3$ perovskites showed superior hydrogen selectivities to the noble metal catalyst for 250–400°C. Although the perovskite catalysts were inferior to the noble metal system at low-temperature light-off, they were more active at ~ 250°C and above. The perovskites also possessed high density; their catalyst bed volumes were only 2/5 that of the noble metal system. The space velocities over the perovskites and Pd/Al_2O_3 were 500,000 h^{-1} and 200,000 h^{-1}, respectively. Thus, the perovskites offered major advantages in compactness, cost and selectivity over the noble metal system, and would be attractive especially for portable power generation applications.

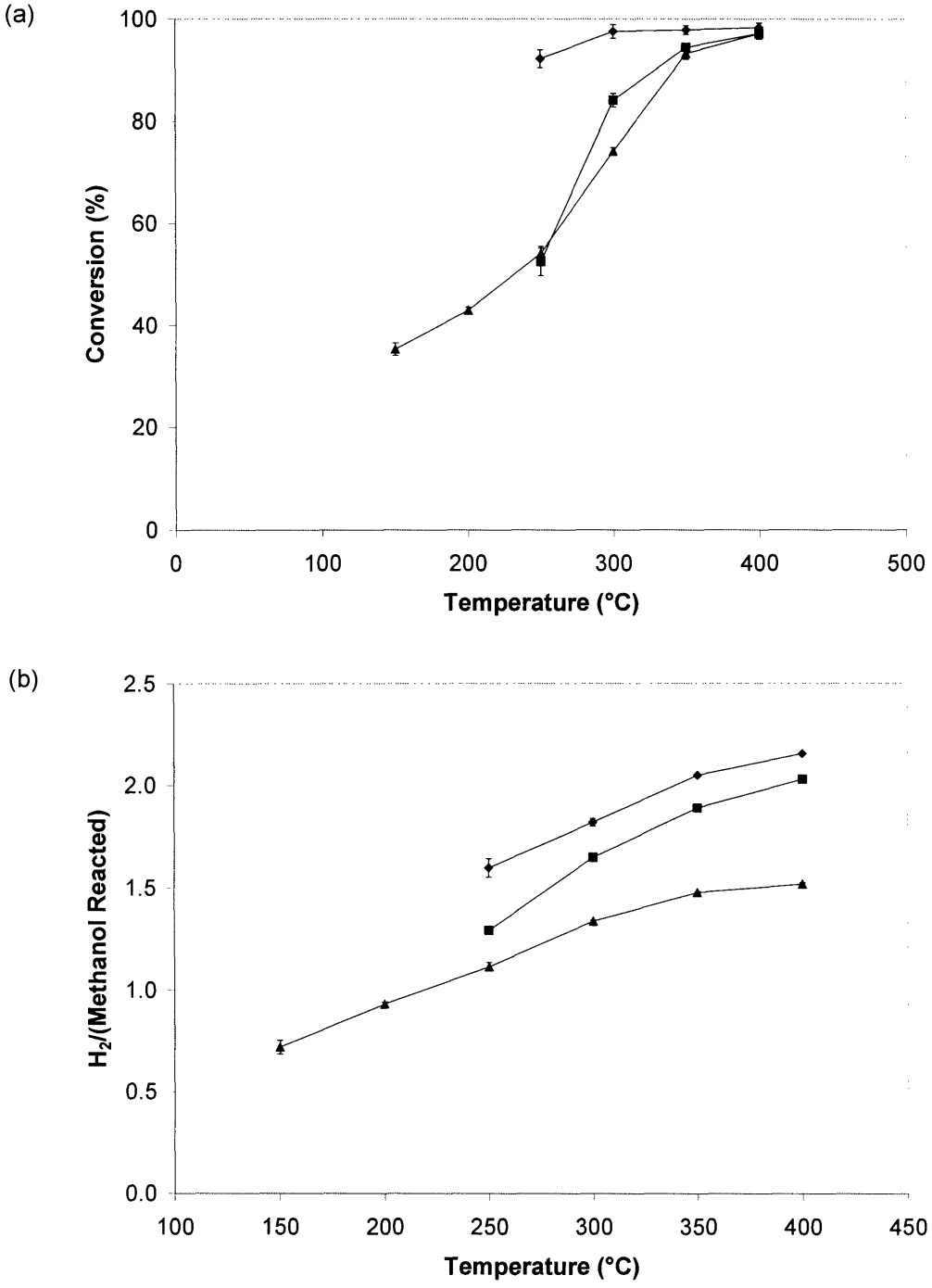

Figure 2.13. (a) Conversion and (b) hydrogen selectivity for oxidative steam reforming of methanol over (■) $LaNiO_3$, (♦) $LaNi_{0.95}Co_{0.05}O_3$, and (▲) 5 wt% Pd/Al_2O_3. The reaction was conducted at a space velocity of 500,000 h^{-1} for $LaNiO_3$ and $LaNi_{0.95}Co_{0.05}O_3$ and 200,000 h^{-1} for 5 wt% Pd/Al_2O_3, with a 5% methanol feed, a water/methanol molar ratio of 1.5, and an oxygen/methanol molar ratio of 0.3.

2.3.8. Oxidative Steam Reforming of Methanol under Full-Fuel Conditions

To examine the ability of the perovskite system to self-sustain the partial oxidation, full-fuel conditions were explored at high space velocities. A 3:1 mixture of water and methanol was preheated with simulated air to 140°C and fed to the reaction zone. Initial studies clearly demonstrated the presence of water-gas shift reaction over both $LaNiO_3$ and 5 wt% Pd/Al_2O_3 catalysts. The carbon dioxide selectivity increased with increasing bed length even after oxygen and methanol were completely depleted. Therefore, the catalysts were compared at the same high space velocity of 1,500,000 h^{-1}. As suggested by the dilute methanol feed studies, the noble metal system was able to light-off from the preheated gas stream, while the perovskite system required external heating. Once ignited, the external heating was removed and replaced with cloth insulation. Both catalysts self-sustained autothermally, and data were collected by increasing the oxygen/methanol ratio over time. A hot spot was observed at the bed entrance, indicating that the entrance temperatures were much higher than those measured just after the catalyst bed under full-fuel conditions.

The perovskite system again outperformed the noble metal catalyst for oxygen/methanol molar ratios of ~ 0.5 (see Figure 2.14). The hydrogen yields for $LaNiO_3$ and 5 wt% Pd/Al_2O_3 were 84% and 71%, respectively. $LaNiO_3$ also demonstrated a much higher CO_2 selectivity over the noble metal system and its performance was slightly enhanced with low levels of cobalt doping. The post-bed temperatures, although sensitive to thermocouple placement and insulation, followed the trend in CO_2 selectivity. As noted earlier, CO combustion would be more exothermic than hydrogen oxidation.

The undoped perovskite catalyst presented some deactivation at an O_2/methanol molar ratio of 0.8. The temperature did not increase further, and oxygen began to bleed from the catalyst bed. The methanol conversion decreased to 99% at an oxygen/methanol molar ratio of 0.95. The perovskite catalyst with low levels of cobalt doping did not demonstrate this deactivation. The temperature continued to rise with increased O_2/methanol molar ratios. The hydrogen selectivity of all three catalysts became similar at elevated O_2/methanol molar ratios.

(a)

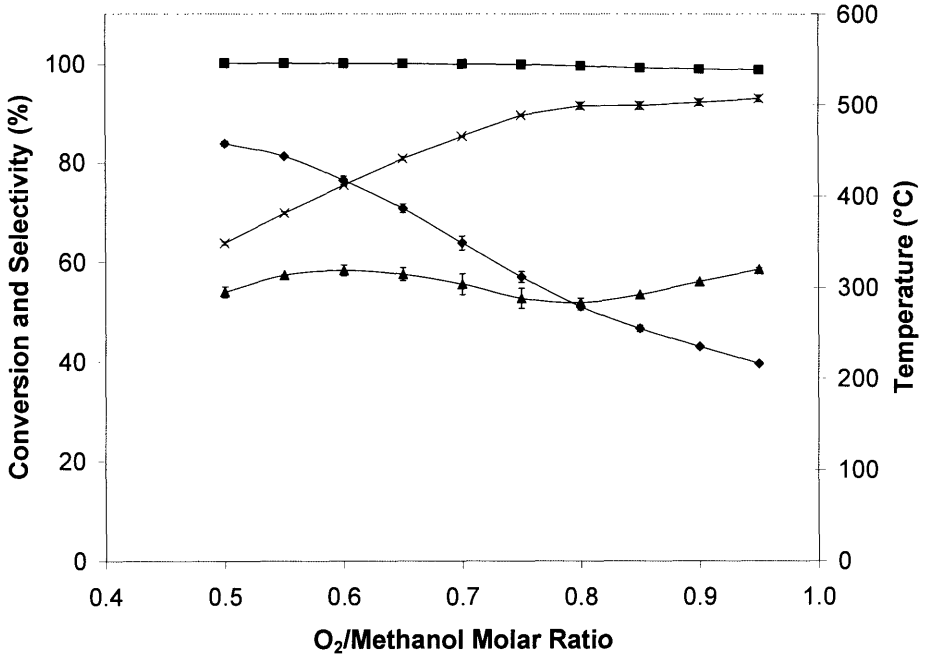
Conversion and Selectivity (%)
Temperature (°C)
O2/Methanol Molar Ratio
0
20
40
60
80
100
0
100
200
300
400
500
600
0.4
0.5
0.6
0.7
0.8
0.9
1.0

(b)

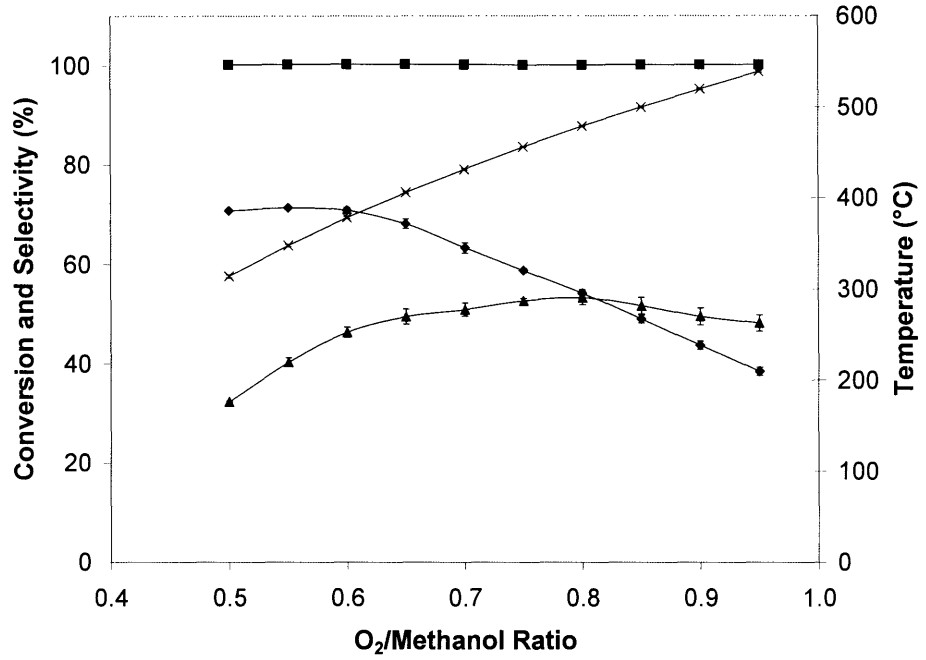
Conversion and Selectivity (%)
Temperature (°C)
O2/Methanol Ratio
0
20
40
60
80
100
0
100
200
300
400
500
600
0.4
0.5
0.6
0.7
0.8
0.9
1.0

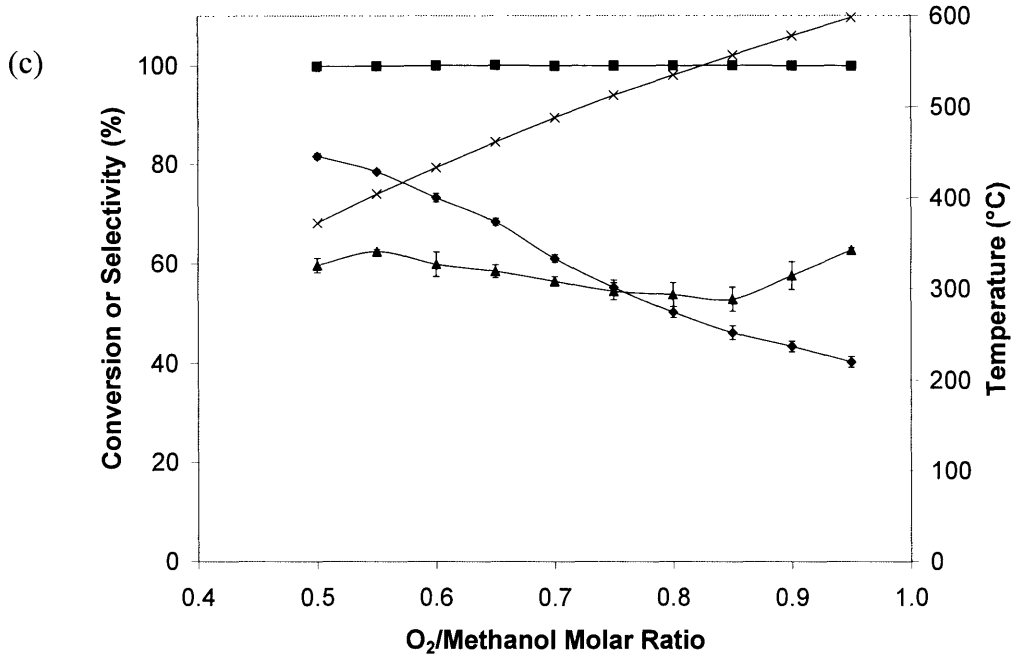

Figure 2.14. (■) Conversion, (♦) hydrogen and (▲) carbon dioxide selectivities, and (×) post-bed temperature for oxidative steam reforming of methanol over (a) $LaNiO_3$, (b) 5 wt% Pd/Al_2O_3, and (c) $LaNi_{0.95}Co_{0.05}O_3$ under full-fuel conditions. The reaction was conducted at a space velocity of 1,500,000 h^{-1} with a water/methanol molar ratio of 3 using simulated air as the oxygen source.

For both catalysts, there was a steady decrease in hydrogen selectivity with increasing oxygen/methanol molar ratio. The carbon dioxide selectivity did not change as significantly. Hydrogen was preferentially oxidized as more oxygen was fed to the system. In attempt to limit homogeneous combustion, pure perovskite granules were loaded in the same mass as in the previous run, but diluted by a factor of 4 in mass with low surface area, high-purity alumina. The composite bed of perovskite and alumina should lower the maximum temperature of the hot spot formed. However, the presence of inert alumina channels in the diluted bed would increase the mixing of the hydrogen product with the oxygen feed. This would lead to more opportunities for oxygen to combust hydrogen heterogeneously in the reaction zone.

Figure 2.15 shows that hydrogen and carbon dioxide selectivities were significantly increased for the alumina-diluted $LaNiO_3$ bed, compared to the undiluted $LaNiO_3$ bed (Figure 2.14(a)). Although the perovskite loading by mass was the same under both experiments, the post-bed temperatures were lower for the alumina-diluted $LaNiO_3$ bed under full-fuel conditions.

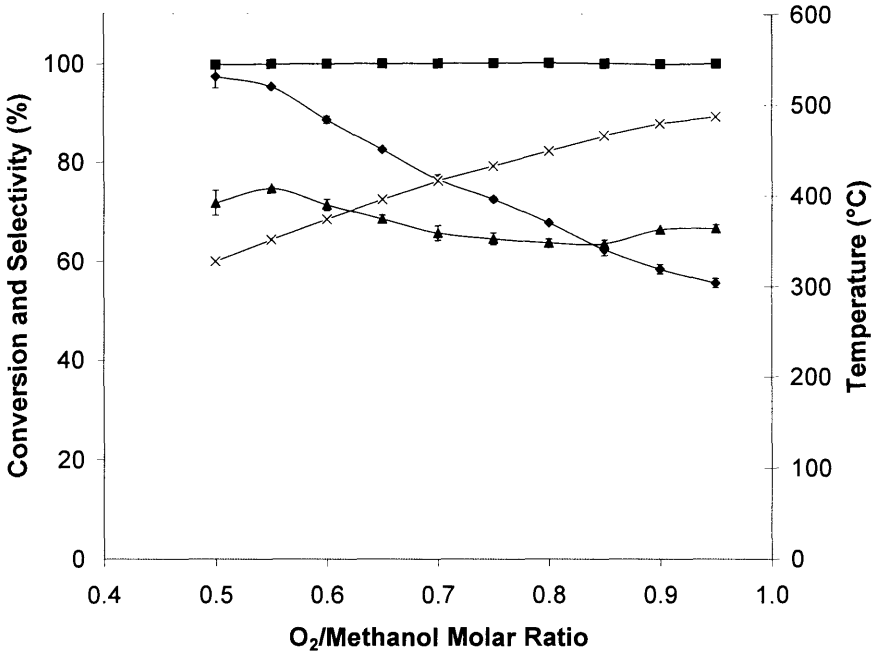

Figure 2.15. (■) Conversion, (♦) hydrogen and (▲) carbon dioxide selectivities, and (×) post-bed temperature for oxidative steam reforming of methanol over alumina-diluted $LaNiO_3$ bed under full-fuel conditions. The reaction was conducted at a space velocity of 1,500,000 h^{-1} with a water/methanol molar ratio of 3 using simulated air as the oxygen source.

If a hot spot was formed at the bed entrance and consumed the methanol and oxygen homogeneously, then a larger portion of the catalyst would be available in the alumina-diluted bed for the water-gas shift reaction. For an oxygen/methanol molar ratio of 0.5, a carbon dioxide selectivity of 72% would imply a hydrogen selectivity of 86%. The measured hydrogen selectivity in the alumina-diluted $LaNiO_3$ bed was 97% (Figure 2.15). In the undiluted $LaNiO_3$ bed, the carbon dioxide selectivity was 54%, implying a hydrogen selectivity of 77%. The hydrogen selectivity observed in this experiment was 84% (Figure 2.14(a)). Water-gas shift activity was increased in the alumina-diluted perovskite bed.

Clearly, in addition to catalyst development, reaction engineering plays a significant role on the system performance for this short contact time partial oxidation reaction. At temperatures where homogeneous reactions were active, the effect of catalyst on selectivity would diminish. To realize the high selectivity demonstrated by the perovskite system for the case of dilute methanol feed, methods for reducing the hot-spot formation were explored. As a first attempt, the liquid precursors were fed directly to the reaction zone. The heat of reaction has been

demonstrated in larger reactors to volatilize the reactants fed [4]. In our experiments, the reaction tended to be quenched over the perovskite bed at an oxygen/methanol molar ratio of 0.5 without using a pre-vaporizer. Furthermore, the vaporization of the liquid fuel produced large bursts in the perovskite bed; this would likely cause serious mechanical degradation to the catalyst film or structure. Channeling was also observed; parts of the bed appeared wet, while other areas maintained a red glow. This suggested that direct feeding of liquid precursors to the catalyst bed without a vaporization zone would not be practical. Other techniques were required to limit the maximum reaction temperature to maintain high hydrogen selectivity.

2.3.9. Hydrogen Generation in a Pd Membrane Microreactor with $LaNiO_3$ Catalyst Film

Another method to lower the maximum reaction temperature was to increase the heat transfer from the reaction zone. This was investigated with a microreactor with a 0.2 μm-thick palladium membrane supported on silicon [15]. A thin film of $LaNiO_3$ catalyst (see Figure 2.16) was deposited in the microreactor channel using an alumina sol. This technique produced a porous coating that did not significantly lower the membrane permeability; the resulting decrease in hydrogen flux was only ~ 20%. The catalyst film showed some aggregation in the corners of the channel due to the deep walls, but its coverage in the center of the Pd membrane was well-suited for this application. The uniform catalyst coating prevented methanol corrosion of the palladium membrane, which would otherwise result in membrane failure under reaction conditions.

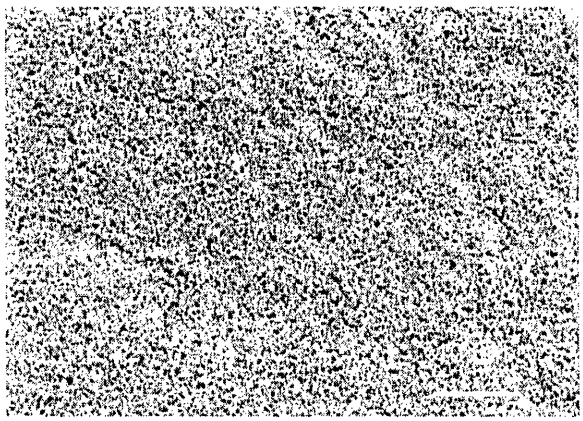

Figure 2.16. $LaNiO_3$ film was deposited with fine porosity to catalyze conversion without substantially lowering the permeability of the underlying Pd membrane.

By this approach, one-step conversion of pure hydrogen from methanol was successfully demonstrated for the first time on the microscale. The presence of a palladium film and fuel bypass altered the system selectivity compared to the packed bed results, but Figure 2.17 illustrates that good hydrogen selectivity was still obtained in the microreactor channel. Moreover, the selectivity to carbon dioxide now showed a strong dependence on the oxygen content.

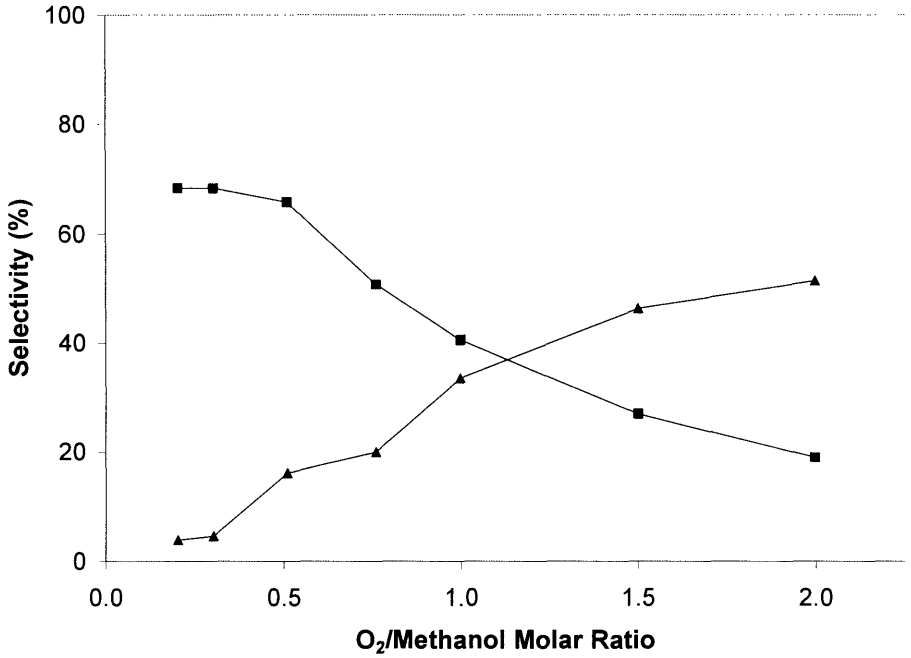

Figure 2.17. (■) Hydrogen and (▲) carbon dioxide selectivities obtained on the reformate side of the Pd membrane microreactor at 400°C. The reaction was conducted at a space velocity of 350 L/(g_{cat}·hr) using a dilute 4% methanol feed without steam addition.

The exothermicity of the reaction was not able to keep the reactor at the desired temperature due to high heat transfer when using either the Pd/Al_2O_3 catalyst or the perovskite catalysts. Even at a feed of 13% methanol (not shown), the reaction still required on-chip heaters to maintain conversion due to the low catalyst loading limit in the current chip design. Overall, the microreactor produced 0.36 sccm of hydrogen from a methanol feed of 0.60 sccm. Future experiments would be required to optimize the microreactor design and catalyst loading to obtain a controlled autothermal operation.

2.4. Conclusions

The pyrophoric nature and stringent upper temperature bound posed major limitations to copper's application in portable reforming. This study examined La-based perovskites as alternatives to copper-based catalysts for the partial oxidation of methanol to hydrogen and carbon dioxide. In particular, $LaNiO_3$ showed very high volumetric activity. The addition of steam increased the catalyst selectivity and stability under the reaction conditions. Compared to 5 wt% Pd/Al_2O_3, $LaNiO_3$ has superior selectivity to hydrogen at 2/5 the catalyst bed volume for dilute (5%) methanol feeds.

Under full-fuel conditions, both perovskite and noble metal catalysts were able to self-sustain the partial oxidation. They gave rise to hot spot formation, which would control the systems' selectivity. To limit the maximum bed temperature to mitigate such effects, a palladium membrane microreactor was developed with $LaNiO_3$ catalyst film. The first microscale production of pure hydrogen from methanol was successfully demonstrated. Microreactor design would be optimized in future studies to increase the catalyst loading to enable autothermal operations.

2.5. References

[1] Idem, R., Bakhshi, N., *Can. J. Chem. Eng.* **74**, 288 (1996).

[2] Twigg, M.V., "Catalyst Handbook Second Edition," p. 330, Manson Publishing, London, 1996.

[3] Camara, G.A., Ticianelli, E.A., Mukerjee, S., Lee, S.J., McBreen, J., *J. Electrochem. Soc.* **149**, A748 (2002).

[4] Jiang, C., Trimm, D.L., Wainwright, M.S., *Chem. Eng. Technol.* **18**, 1 (1995).

[5] Huang, T.J., Chren, S.L., *Appl. Catal. A* **40**, 43 (1998).

[6] Cubeiro, M.L., Fierro, J.L.G., *J. Catal.* **179**, 150 (1998).

[7] Huang, T.J., Wang, S.W., *Appl. Catal. A* **24**, 287 (1986).

[8] Pena, M.A., Gomez, J.P., Fierro, J.L.G., *Appl. Catal. A* **144**, 7 (1996).

[9] Barbier, J., Duprez, D., *Appl. Catal. B: Environ.* **4**, 105 (1994).

[10] Velu, S., Suzuki, K., Okazaki, M., Kapoor, M.P., Osaki, T., Ohashi, F., *J. Catal.* **194**, 373 (2000).

[11] Grenoble, D.C., Estadt, M.M., Ollis, D.F., *J. Catal.* **67**, 90 (1981).

[12] Ogura, N., Kawamura, Y., Igarashi, A., Katsumata, T., "Hydrogen Production by Methanol Reforming for Small PEMFC," Fuel Cell Seminar 2002, Palm Springs, 2002.

[13] Haruta, M., Yamada, N., Kobayashi, T., Lijima, S., *J. Catal.* **115**, 301 (1989).

[14] Deluga, G.A., Salge, J.R., Schmidt, L.D., Verykios, X.E., *Science* **303**, 993 (2004).

[15] Wilhite, B.A., Schmidt, M.A., Jensen, K.F., Ind. Eng. Chem. Res. **43**, 7083 (2004).

[16] Fokema, M.D., Chiu, E., Ying, J.Y., *Langmuir* **16**, 3154 (2000).

[17] Amphlett, J.C., Evans, M.J., Jones, R.A., Mann, R.F., Weir, R.D., *Can. J. Chem. Eng.* **59**, 720 (1981).

[18] Masel, R.I., "Principles of Adsorption and Reaction on Solid Surfaces," Wiley Interscience, New Jersey, 1996.

[19] Velu, S., Suzuki, K., Osaki, T., *Catal. Lett.* **69**, 43 (2000).

[20] Deutschmann, O., Schmidt, L.D., *AIChE J.* **44**, 2465 (1998).

[21] Glassman, I., "Combustion," p. 589. Academic Press, San Diego, 1996.

[22] Edwards, N., Ellis, S.R., Frost, J.C., Golunski, S.E., van Keulen, A.N.J., Lindewald, N.G., Reinkingh, J.G., *J. Power Sources* **71**, 123 (1998).

[23] Myers, D.B., "Steam Reforming of Methane with Nickel Aluminate-Based Catalysts," M.S. Thesis, Massachusetts Institute of Technology, 2000.

[24] Gotti, A., Prins, R., *J. Catal.* **175,** 302 (1998).

[25] Shan, W., Feng, Z., Li, Z., Zhang, J., Shen, W., Li, C., *J. Catal.* **228**, 206 (2004).

[26] Ling, T.R., Chen, Z.B., Lee, M.D., *Appl. Catal. A* **136**, 191 (1996).

[27] Tejuca, L.G., Fierro, J.L.G., *Thermochim. Acta* **147**, 361 (1989).

[28] Martinez-Lope, M.J., Casais, M.T., Alonso, J.A., *Eur. J. Sol. State Inorg.* **32**, 521 (1995).

[29] Choudhary, V.R., Uphade, B.S., Belhekar, A.A., *J. Catal.* **163**, 312 (1996).

[30] Cubeiro, M.L., Fierro, J.L.G., *Appl. Catal. A* **168**, 307 (1998).

Chapter 3 – Materials Development for Micro-Solid Oxide Fuel Cells

3.1. Introduction

To achieve significant market shares, fuel cell technology must be able to produce electricity at competitive costs. While the average US consumers pay under 10 cents/kWh for electricity in their homes, they pay around $300/kWh for portable power produced from batteries. There is also consumer dissatisfaction with the existing battery lifetime. Most developments in the portable power market have been centered on low-temperature polymer electrolyte membrane (PEM) fuel cells [1], which are limited by their high fuel purity requirements. Some recent efforts have been devoted to the miniaturization of solid oxide fuel cells (SOFC) [2]. This chapter is focused on materials development in fabricating Si-supported micro-solid oxide fuel cells (μSOFC).

Traditionally, planar SOFC utilize a thick self-supporting yttria-stabilized zirconia (YSZ) electrolyte of 150–400 μm thick. The electrodes are applied to the YSZ electrolyte, and the stacks are fabricated using interconnects and flow manifolding. As thick self-supporting electrolytes introduce significant ohmic losses at lower temperatures, current research has focused on reducing the electrolyte thickness to significantly improve power densities [3]. A general guideline has been proposed to illustrate the relationship of electrolyte thickness on overall cell resistivity. Figure 3.1 shows the electrolyte thickness required at a given temperature to maintain a low electrolyte contribution to ohmic losses [4].

Conventional ceramic processing techniques have produced YSZ electrolytes of 10–20 μm thick [5]. Semiconductor deposition techniques such as sputtering, pulsed laser deposition and e-beam deposition have produced self-supporting YSZ electrolytes with thickness of 100–400 nm [6]. Such a dramatic reduction in electrolyte thickness might allow for lower temperature operation, and lower the system's thermal mass, greatly reducing the start-up time of the device.

While sputtering is well-suited for the deposition of dense layers, it is difficult to create porous electrodes by sputtering without the use of patterned masks [2]. Furthermore, the porosity introduced by patterned masks only approaches what is commonly achieved with traditional ceramic pastes. In order to fully realize the potential of thinner electrolytes, the electrode structures have to be improved as well. Thus, we have examined wet-chemical

deposition techniques to more flexibly control the microstructure and composition of materials than the semiconductor processing techniques. This would be very useful towards the deposition of catalyst, anode, electrolyte and cathode layers within the micro-reformer and micro-fuel cell systems.

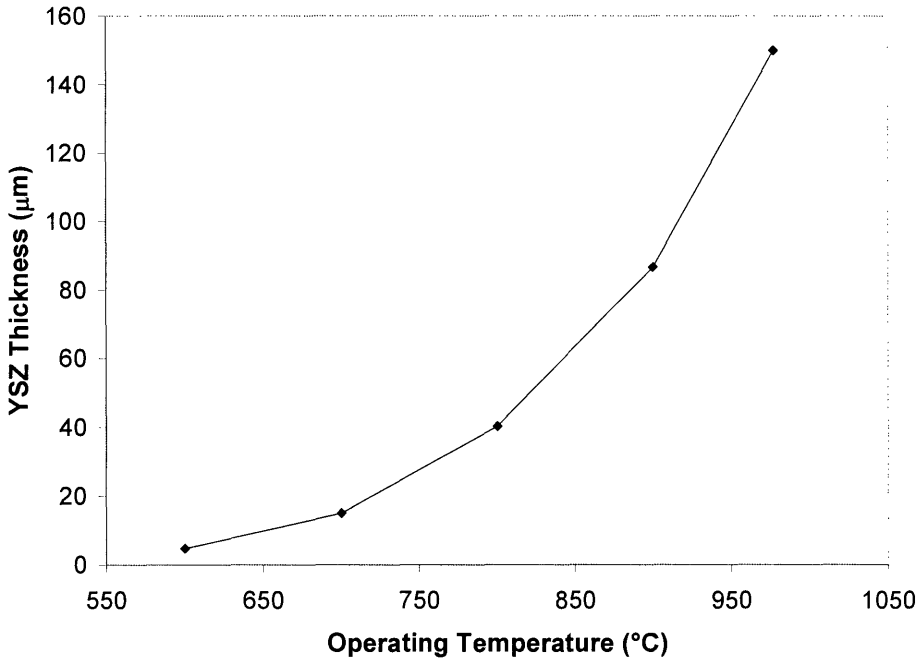

Figure 3.1. YSZ electrolyte thickness required to limit area-specific resistance to 0.15 $\Omega \cdot cm^2$ at various operating temperatures.

3.1.1. Materials Processing Techniques

Incorporation of the catalyst or electrode films into a system is an iterative process where the films may alter the device design. In general, the first priority is to create a defect-free electrolyte film of a few hundred nm thick, which requires a perfectly flat and non-porous support. A sample of a sputtered YSZ electrolyte is shown in Figure 3.2; the YSZ film became buckled right after its silicon support has been removed. Depositing this dense electrolyte onto a traditionally applied wet-chemical thick film would be challenging. However, deposition of electrolyte onto a sol-gel derived thin film of 500 nm-thick may be possible.

Another important design consideration is related to the conductivity of the electrodes. If the electrodes are on the order of a few hundred nanometers, they would have extremely large resistivity in the X-Y plane, requiring the use of complicated current collectors to limit ohmic losses. For the geometry above, the resistance of the cathode plane could be calculated assuming

that perfect current pathways existed on the outer two sides of the supported electrolyte (see Figure 3.3). A resistance of 200 Ω was estimated for a dense $La_{0.8}Sr_{0.2}MnO_3$ (LSM) cathode of 250 nm-thick at 600°C. To avoid such high resistance, thicker films should be utilized for the perovskite cathode materials.

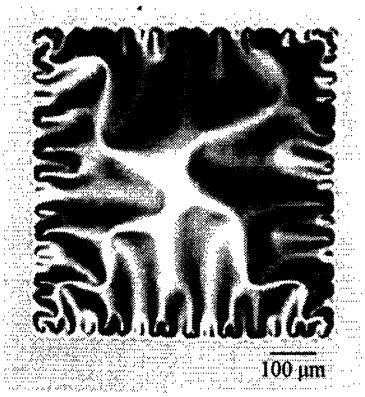

Figure 3.2. 100 nm-thick YSZ electrolyte produced by sputtering [6].

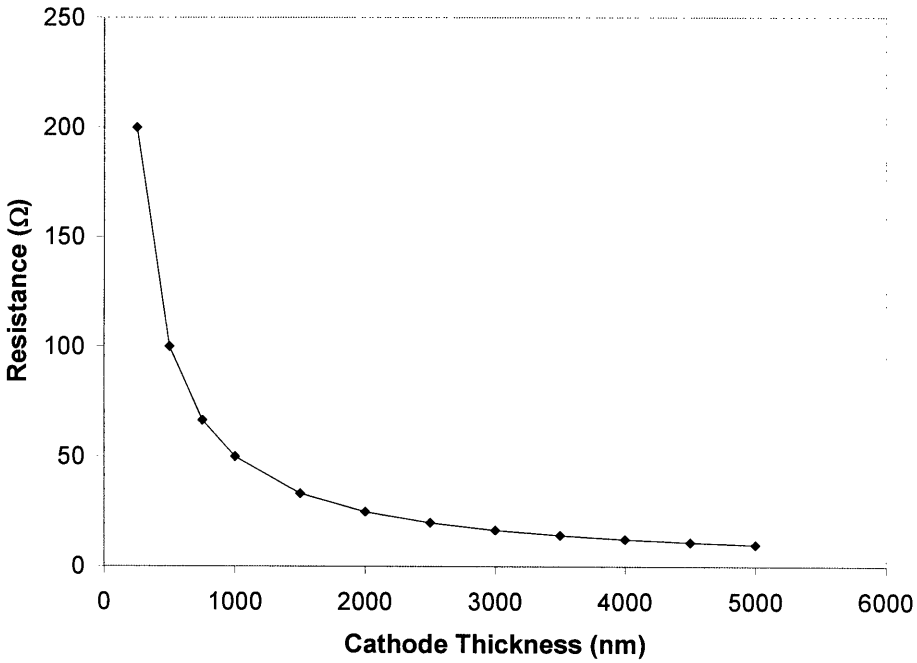

Figure 3.3. Calculated resistance of a dense LSM cathode at 600°C for a 550 nm x 550 nm YSZ electrolyte with parallel current collectors.

Traditional SOFC electrodes are processed using oxide powder dispersion with an organic binder (typically ethylcellulose) [7]. Upon calcination, the binder is removed and the

powder is partially sintered to form a film. Table 3.1 shows the firing temperatures of conventional electrode materials. Such high temperatures must be avoided to prevent damage to the electrolyte and heater elements in the μSOFC system [6]. Thus, alternative approaches have to be developed to achieve adhesion of the desired electrode materials to the electrolyte at temperatures significantly below those needed for partial sintering.

Table 3.1. Recommended firing temperatures of commercially available electrode inks.

Electrode Composition	Firing Temperature (°C)
Ni/YSZ	1300
$La_{0.8}Sr_{0.2}MnO_3$ (LSM)	1000
$La_{0.8}Sr_{0.2}Fe_{0.8}Co_{0.2}O_3$ (LSCF)	900

We have applied thick catalyst films using an inorganic binder instead of an organic binder. Upon calcination, the inorganic binder would transform into an oxide material to promote low-temperature adhesion. Similar concepts have been used in binding catalyst coating onto catalytic converter honeycomb in automotive exhaust remediation [8,9,10]. This approach would allow strong adhesion to be achieved at temperatures below the sintering temperature to retain the high catalyst activity. Films produced are typically > 5 μm in thickness.

3.1.2. Inorganic Binders

As sols are traditionally employed as inorganic binders for catalyst coatings, they would be explored in this study. Other techniques that might offer greater compositional flexibility would also be developed for μSOFC application.

3.1.2.1. Colloidal Sols

Sols are colloidal dispersions of particles. The colloidal crystallinity depends on the heat treatment that the sol has been subjected to. The sol may involve partially hydrolyzed salt precursors or crystalline oxide particles. Pre-formed sols have well-defined particle sizes and are stabilized over time via electrostatic repulsion [11]. Addition of coagulating salts, changes in pH or solvent evaporation may cause a sol to gel. A much higher oxide yield is obtained from colloidal sols compared to metallorganic precursors (which have high carbon contents).

The most common sol formulation involves acid peptization of precipitated materials [12,13,14]. This is achieved by first preparing an agglomerated precipitated powder with a fine primary particle size. This powder is then washed to remove ion impurities, and then dispersed in hot acid (typically acetic or nitric acid). The acid anion acts as the supporting electrolyte for the dispersion. Once charged, the agglomerates become dispersed and a viscous sol is produced, which can be used for spin-coating or dip-coating [15].

The acid peptization step limits the sol composition to one component since different precipitates would be leached differently. For example, acid treatment has been shown to leach the Sm dopants preferentially in ceria-based sols [16].

3.1.2.2. Sol-Gel Processing

Sol-gel processing involves the hydrolysis and polycondensation of metal alkoxide precursors, producing alcohols as by-products. Sol-gel derived films show a good oxide yield upon heat treatment. Simple coating formulations of alumina, titania and silica involve partially hydrolyzed metal alkoxides prior to application [17]. In the processing of multicomponent perovskites, 2-methoxyethanol is commonly used in forming the alkoxide precursors as it readily reacts with most metal sources [18].

3.1.2.3. Chelation

Chelation is frequently used to limit the rate of hydrolysis of a reactive precursor in sol-gel processing. A classic example would be the chelation of titanium isopropoxide with acetic acid to produce lead zirconium titanate (PZT) [19]. Without chelation, the titanium precursor would react too quickly to produce a homogeneous multicomponent oxide. Complete chelation of a metal precursor has also been employed to provide for stability in air for spin-coating applications. For example, ceria has been processed using diethanolamine to chelate cerium ethoxide [20]. In our applications, the chelating solutions were found to exhibit wetting problems with the substrates.

3.1.2.4. The Pechini Method

The Pechini method is often employed as a non-air-sensitive technique for processing multicomponent films [21]. It uses an aqueous medium and commonly available metal salts.

Citric acid and ethylene glycol are added to the salt solution, which dehydrates to form a polyester upon drying. This polymer can then be dissolved in formic acid or other non-aqueous solvents to redilute the system prior to spin-coating. Strong chelators, such as ethylenediame, are often needed to ensure complete solubilization. In an ideal formulation, a polymer film is produced that associates randomly with the various inorganic elements by the carboxylic groups.

3.1.2.5. Metallorganic Decomposition

Metallorganic decomposition (MOD) involves the thermal decomposition of metallorganic precursors to produce an oxide film. Metal carboxylates or metal β-diketonates are typically employed as the precursors since they promote oxide formation by bonding to the metal ion through an oxygen moiety. To limit the organic content, metal acetate and metal acetylacetonate are frequently used. Although β-diketonates are monomeric, metal carboxylates can produce extended structures due to the bridging of carboxylic groups (see Figure 3.4) [22]. This oligomerization can produce viscous solutions and even subsequent precipitation/gelation when the carboxylates are solubilized in non-aqueous solvents. This technique is limited by the availability of the metal salts, and the stability of the precursor solutions. It may be difficult to obtain the desired oxide phase, depending on the homogeneity of the carboxylate mixture and the respective decomposition temperatures of the precursors involved [18].

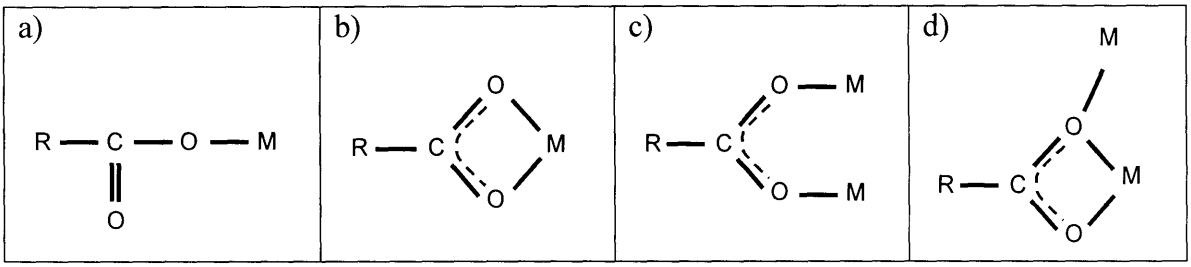

Figure 3.4. Possible binding configurations in metal carboxylates: (a) monodentate, (b) chelating, (c) bridging, and (d) bridging-chelating configurations.

3.1.2.6. Transformation to the Desired Oxide Phase

For all the techniques described above, the inorganic precursor has to be converted to a film with the desired oxide phase. Managing this transformation requires manipulating the oxide precursors, since it is difficult to control the phase transformation and purity based solely on the initial film properties. For example, once the barium metallorganic precursors are converted to barium carbonate during calcination, the desired phase would not be obtained since barium

carbonate is highly stable. To counter such challenge, an alternative precursor that produces an intermediate barium oxyflourite has been developed to prevent carbonate formation [23].

3.1.3. Coating Design and Material Selection

The most accessible electrode for wet-chemical processing is the top electrode. Since the cathode is known to contribute the most to cell losses at low temperatures, cathode materials are the focus of this study [24,25]. For SOFC operation below 800°C, composite cathodes are preferred over the conventional single-phase LSM. Composite electrode designs allow for the maximum number of interfaces to be established between the gas phase, the electronic conductor, and the ionic conductor. The most common composite cathode for low-temperature operation involves the mixing of LSCF with the electrolyte material [26]. In this study, we focus on developing nanocomposites of LSCF with YSZ or Sm-doped ceria (SDC).

To maximize the perovskite loading in the cathode film, the LSCF source will be a preformed powder. To promote the cathode film adhesion, the electrolyte precursor will be used as the inorganic binder. Colloidal sols will be employed when utilizing YSZ as the inorganic binder. For SDC incorporation, metallorganic decomposition of Ce and Sm acetates will be examined. Sol-gel precursors are not developed for inorganic binder processing since they are too air-sensitive. The Pechini method is also not employed as it involves exothermic decomposition [27] and produces low oxide yields.

As mentioned previously, novel electrode structures would be required to realize the full potential of ultrathin electrolytes. Decreasing YSZ thickness below 8 μm at 800°C did not lead to improved SOFC performance even when the most advanced perovskite composite cathodes were used [28]. At the desired μSOFC operating temperatures, the limited ionic conductivity of the cathode material suggested that the majority of oxygen reduction would occur along the electrode surface paths [29,30,31]. Thus, it would be of interest to develop noble metal films with good catalytic activity towards oxygen. Platinum films would be created with fine porosity and metallic conductivity, so that complicated current collectors would not be required.

3.2. Synthesis and Characterization of Oxide Films

For the development of SDC binder, the acetate precursors were refluxed in anhydrous acetic acid at various concentrations. Ammonium hydroxide was added at set molar ratios to the

metal ions to increase the viscosity of the precursor solution, which was measured using a Bohlin viscometer. The solutions were filtered with a Pall Acrodisc syringe filter (0.2 μm). Spin coating was performed on Si substrates using a Headway Research spin coater (≤ 7500 rpm) to examine the effects of synthesis parameters on the film properties. Thin film morphology was observed by atomic force microscopy (AFM) using a Digital Instruments Nanoscope IIIa Scanning Probe Microscope. The crystalline phase of the thin films was examined by X-ray diffraction (XRD) with a Rigaku rotating anode X-ray diffractometer (18 kW).

Thick films were developed by creating a dispersion of the ceria MOD precursor solution, LSCF powders (Praxair Specialty Oxides) and SDC powders (Nextech) in a SPEX 8000 high-energy ball mill with zirconia jar and media. Both the LSCF and SDC oxide powders have a median particle size, D_{50}, of < 1 μm. The LSCF powders were not very stable upon prolonged exposure to the concentrated acetic acid. Therefore, SDC powders were used for adhesion studies. The adhesion strength of 400°C-calcined SDC films to glass substrates was measured using an Instron machine. Carefully aligned rectangular rods were attached to the coated and uncoated sides of the glass substrate using epoxy, and the force required to detach the oxide film was measured. LSCF films with good adhesion properties were also produced, but preferably by dip-coating and brushing.

Commercially available sols were used to develop the YSZ-based inorganic binder. Nyacol's Y10/14 was used as the yttria source; it has a particle size of 10 nm and an oxide loading of 14 wt%. Nyacol Zr10/20 (10 nm, 20 wt%) and Zr100/20 (100 nm, 20 wt%) sols were used as the zirconia source. The commercial sols were mixed to produce 8 mol% YSZ (8YSZ).

YSZ particles were also prepared by chemical precipitation. Tetraethylammonium hydroxide (TEAH) was dissolved in isopropanol (0.4 M); zirconium nitrate and yttrium nitrate were dissolved in water (2.25 M). These solutions were mixed at various TEAH-to-metal cation ratios, aged, and washed three times in methanol by centrifugation. An IKA homogenizer was used to facilitate the deagglomeration and rinsing steps. Particle size of the resulting dispersion was measured with dynamic light scattering (DLS) using a Lexel 95 argon ion laser, a Brookhaven high-precision photomultiplier at 90°, and a Brookhaven 9000AT correlator.

Thick films were produced by mixing the commercial sols with the LSCF powders. Ethylene glycol was added to slow down the drying rate. Thick films were applied by brushing, and their adhesion strengths were measured with an Instron machine. Electrical conductivity

measurements were performed using a Heidolph MR3001 hot plate, multimeter and Pt electrodes. The film morphology and composition were examined by scanning electron microscopy (SEM) (JOEL 5910).

Noble metal films were generated using Pt (M603B), Cu (A6052A) and Ni (OL-58A) resinates from Engelhard. The precursors were filtered with quartz wool and a calcium chloride bed, and diluted with dichloromethane. Ni or Cu resinate (20 vol%) was blended with Pt resinate, and the resulting film was calcined at 550°C. Ni or Cu was then etched in hot nitric acid (2 N) to create porosity within the film. The film morphology and composition was examined by high-resolution SEM (JEOL 6320FV with EDX).

The polymeric film mask for sputtering was developed with polystyrene (MW = 350,000) and poly(methylmethacrylate) (PMMA, MW = 15,000) from Sigma-Aldrich. The polymers were mixed at a weight ratio of 50:50 and diluted to 1 wt% in toluene. The films were applied onto Si by spin coating at 2000 rpm, and vacuum dried at 50°C overnight. The polystyrene component in the films was then removed with cyclohexane.

3.3. Results and Discussion

3.3.1. Spin Coating

Initial experiments were performed using hydroxide suspensions as the spin-coating precursor. The hydroxide precursors for LSCF were prepared using methods similar to those discussed for the colloidal YSZ. They were spin-coated onto a pristine Si substrate at different rpm, and calcination to 550°C (see Figure 3.5). Thicker films with more shrinkage in the X-Y plane were obtained at the lower rpm. Overall, poor Si adhesion was noted for films derived from hydroxide suspensions in methanol.

Improved coatings were obtained using hydroxide suspensions peptized with acetic acid. The resulting films adhered well to Si substrates. Adherent films were also achieved with viscous solution of metal acetates in acetic acid with ammonium hydroxide addition. The film quality showed little dependence on the order of processing for this composition. In general, these LSCF films were translucent and hard, with better adhesion to the substrates than those derived with the hydroxide precursors without acetic acid.

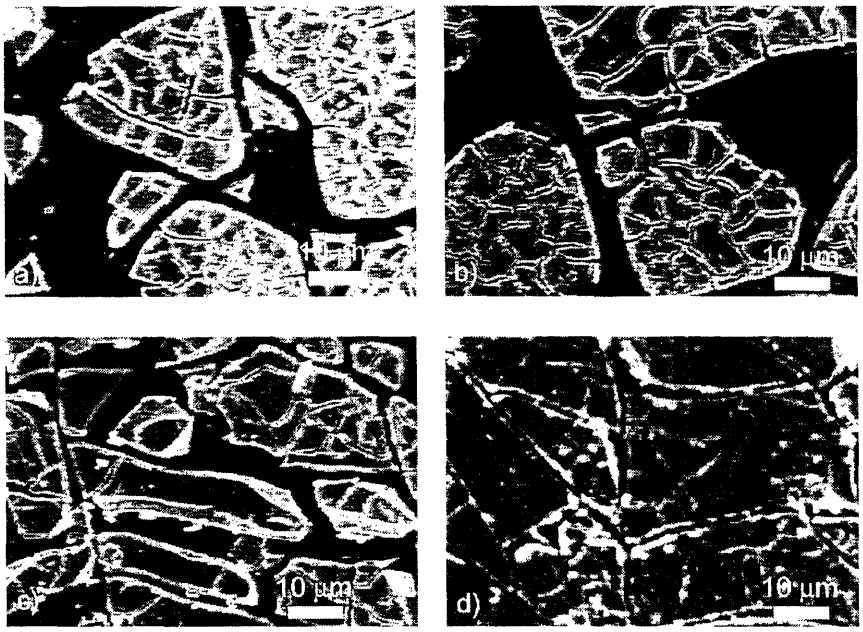

Figure 3.5. LSCF films coated onto Si substrates at (a) 1000 rpm, (b) 2000 rpm, (c) 3000 rpm, and (d) 4000 rpm.

3.3.2. Acetate Solution as Inorganic Binder for Thick Film Deposition

3.3.2.1. MOD Acetate Solution Optimization for SDC

Given the successful application of LSCF films using (i) the acid-peptized hydroxide suspension and (ii) the acetate solution with ammonium hydroxide, SDC films were developed using similar approaches.

Ammonium hydroxide is used commonly as an additive in the MOD of acetates for spin coating. The effect of this additive on SDC film characteristics was studied. Figure 3.6 shows that the viscosity of the SDC precursor solution in acetic acid increased with the acetate concentration. Cerium acetate is known to form linear coordination polymers [32]. Figure 3.6 also shows that the viscosity of the acetate precursor solution increased more dramatically with the acetate concentration when ammonium hydroxide was introduced.

To understand the extent of solution thickening caused by the ammonium hydroxide addition, samples were prepared with the same ammonium hydroxide concentration in acetic acid without the acetate precursor. The viscosity of the ammonium hydroxide solution was then subtracted from the viscosity of the acetate precursor solution with ammonium hydroxide addition. Figure 3.7 shows that the resulting viscosity curves were still dependent on the

NH_4OH/acetate molar ratios, indicating that there was substantial interaction between the metal acetates and the ammonium hydroxide, possibly changing the physical form of the cerium acetate or the structure of the coordination complex.

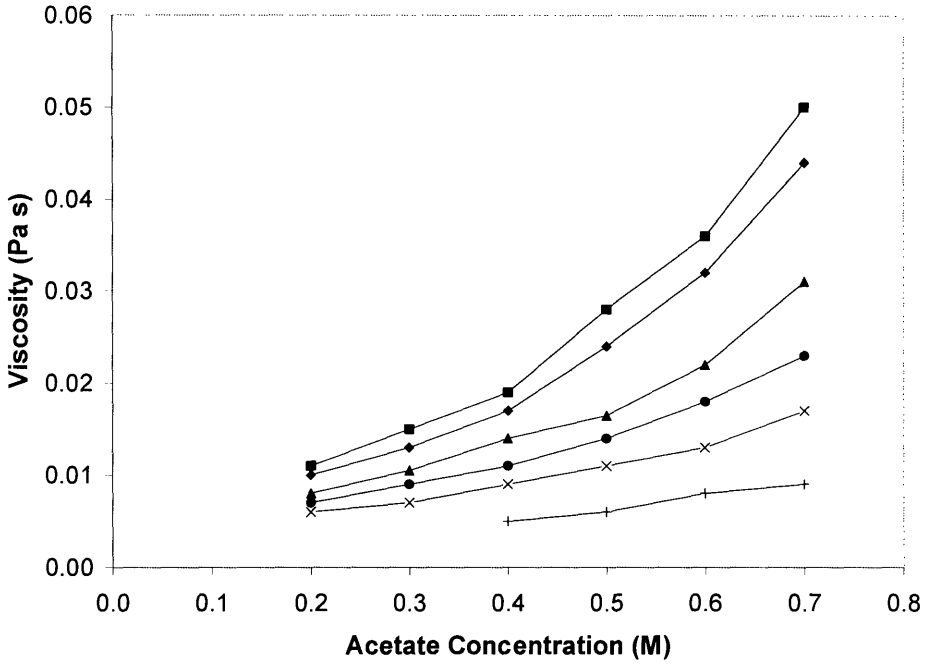

Figure 3.6. Viscosity of the acetate precursor solution for SDC at a NH_4OH/acetate molar ratio of (+) 0, (×) 0.8, (●) 1.6, (▲) 2.5, (♦) 3.3, and (■) 4.1.

Interestingly, this effect shows up in a basic property obtained from the viscosity measurements. The intrinsic viscosity is a measure of the hydrodynamic volume of solutes in a solution at a dilute concentration, where the solutes do not interact with each other. For 1 g of solutes, it is the effective volume that these non-interacting solutes possess in solution, calculated as:

$$[\eta] = \lim (\eta_{sp}/c) \text{ as } c \rightarrow 0 \qquad (1)$$

where $\eta_{sp} = (\eta-\eta_o)/\eta$, and $\eta_o =$ the viscosity of the acetic acid solvent.

For a true polymer solution, the intrinsic viscosity is related to the polymer molecular weight by the following empirical formula,

$$[\eta] = k M^a \qquad (2)$$

Thus, once k and a are known for a polymer-solvent mixture, the polymer molecular weight can be calculated. In our case, the intrinsic viscosity could be plotted versus the NH_4OH/acetate molar ratio, which was held constant across the dilutions.

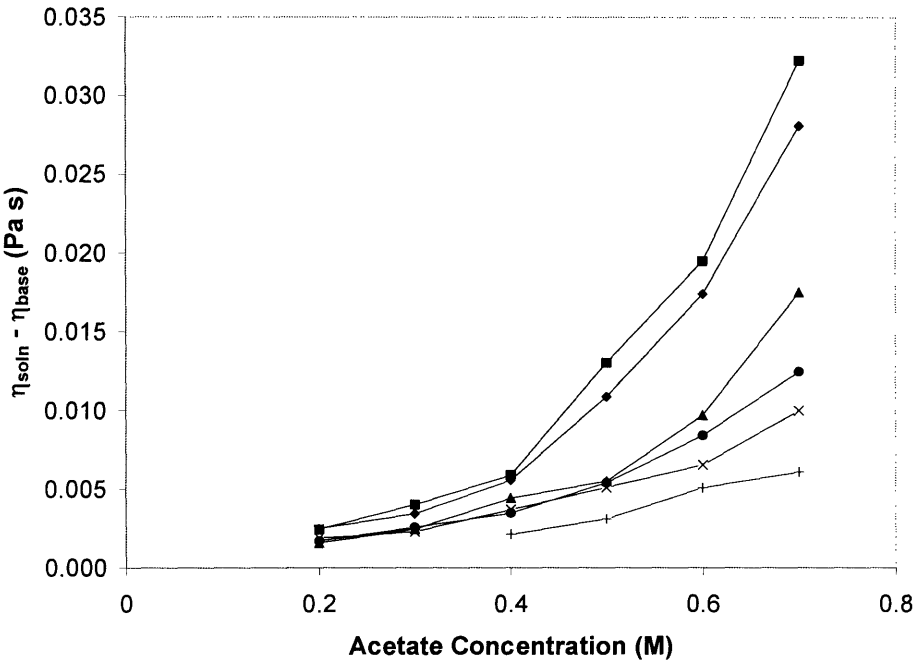

Figure 3.7. Viscosity of the acetate precursor solution for SDC at a NH_4OH/acetate molar ratio of (+) 0, (×) 0.8, (•) 1.6, (▲) 2.5, (♦) 3.3, and (■) 4.1, after subtracting the viscosity of the ammonium hydroxide solution.

Figure 3.8 shows that the intrinsic viscosity of the solution was almost zero when there was no ammonium hydroxide addition, suggesting that the acetate molecular weight would be close to zero. In essence, the acetate precursor solution without ammonium hydroxide addition was merely a dissolved salt in acetic acid with no long-range coordination.

In the concentrated acetate solutions, ammonium and cerium ions would both be present upon the addition of ammonium hydroxide, possibly leading to a new mixed cation coordination denoted by $[Ce^{+3}(O_2CCH_3)_n]^{(3-n)}[NH_4^+]_{(n-3)}$ [33,34]. The coordination polymer involving cerium and ammonium ions would likely be different from the original linear cerium acetate structure. If the cerium chains were effectively crosslinked or branched by the ammonium ion, the viscosity would increase.

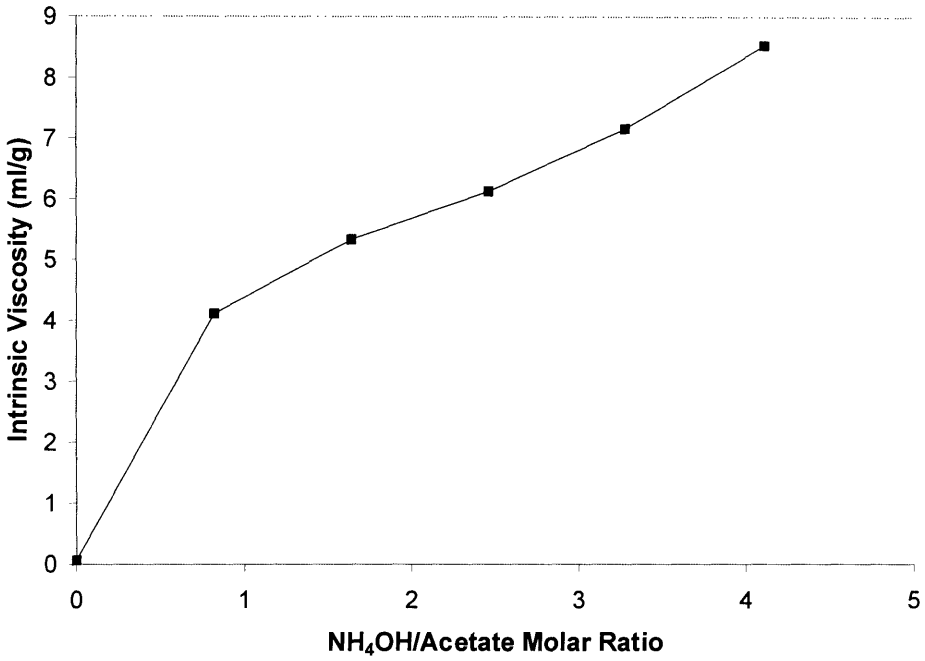

Figure 3.8. Intrinsic viscosity of the acetate precursor solution as a function of the NH_4OH/acetate molar ratio.

The other possible cause for the viscosity increase was the hydrolysis of cerium ions in solution upon the ammonium hydroxide addition. This would depend on whether the cerium ion or acetic acid was the stronger acid. The possible reactions are denoted as follows:

$$Ce[H_2O]_x^{+3} \rightarrow CeOH[H_2O]_{x-1}^{+2} + H^+ \quad (3)$$

$$H_3CCO_2H \rightarrow H_3CCO_2^- + H^+ \quad (4)$$

$$NH_4OH \rightarrow NH_4^+ + OH^- \quad (5)$$

$$OH^- + H^+ \rightarrow H_2O \quad (6)$$

For Ce(III), no hydrolysis has been known to occur at a pH below 6 [35]. Above a pH of 6 but below the precipitation pH of 7, only 1% of the metal ions hydrolyze to $Ce_3(OH)_5^{+4}$ [36]. Thus, for the Ce(III) acetate MOD precursor solution, the increase in viscosity in acetic acid from ammonium hydroxide addition was not a result of hydrolysis or subsequent oligomerization of a hydrolyzed cerium ion. Therefore, the viscosity increase upon the ammonium hydroxide addition was attributed to the change in the coordination structure of the mixed cation solution.

3.3.2.2. Spin Coating of SDC with MOD Acetate Solution

The applicability of the various MOD precursors for SDC was compared. Ammonium hydroxide addition greatly improved the film quality and coverage, but diluted the inorganic content. The films deposited with high ammonium hydroxide content showed significant cracking upon drying. Instead of using ammonium hydroxide, methanol could be added to improve the surface coverage of the Si substrate while also increasing the stability of the precursor solution. A good recipe would involve diluting a 1.5-M precursor solution to 0.7 M with methanol, similar to that developed by [37]. This solution was cooled and filtered before coating application. The 400°C-calcined SDC film has a fine grain size and some pinholes (see Figure 3.9); its crystallinity was confirmed by XRD.

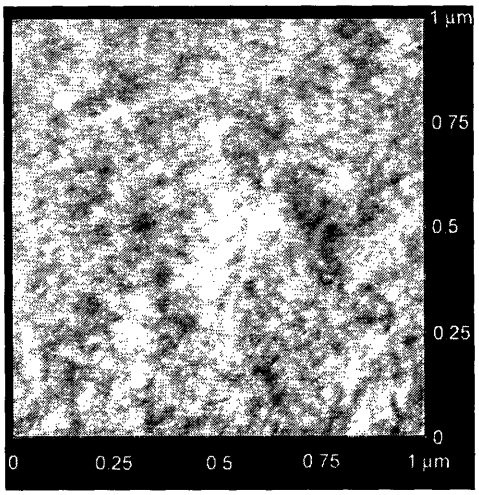

Figure 3.9. AFM of 400°C-calcined SDC film.

3.3.2.3. MOD Acetate Solution as Inorganic Binder for Thick Film Deposition

The MOD acetate precursor solution was used as an inorganic binder for SDC thick film deposition. 4 g of fine SDC oxide particles were dispersed in 10 ml of SDC MOD acetate solution to form a slurry. The paint was formulated so that the binder (MOD acetate solution) contributed to 15 wt% of the final SDC yield. Since this dispersion contained particles, it did not apply well to the substrate by spin-coating. Air-brushing was then explored for film deposition. Figure 3.10 shows that the viscosity of the slurry was lowered with ammonium hydroxide addition, due to increased particle dispersion from more effective electrostatic repulsion. The coating strength improved with increasing ammonium hydroxide content. Since the slurry would dry rapidly as it approached the target in air-brushing, solution stability would be critical in this

technique. The solution with low ammonium hydroxide content would dry faster and precipitate easier than that with high ammonium hydroxide content. Thus, the latter would lead to SDC films with better adhesion. LSCF thick films were subsequently produced utilizing the MOD solutions of SDC as the inorganic binder for LSCF oxide particles. This coating solution exhibited similar properties as outlined above, but required more rapid application due to LSCF's instability upon prolonged exposure to concentrated acid.

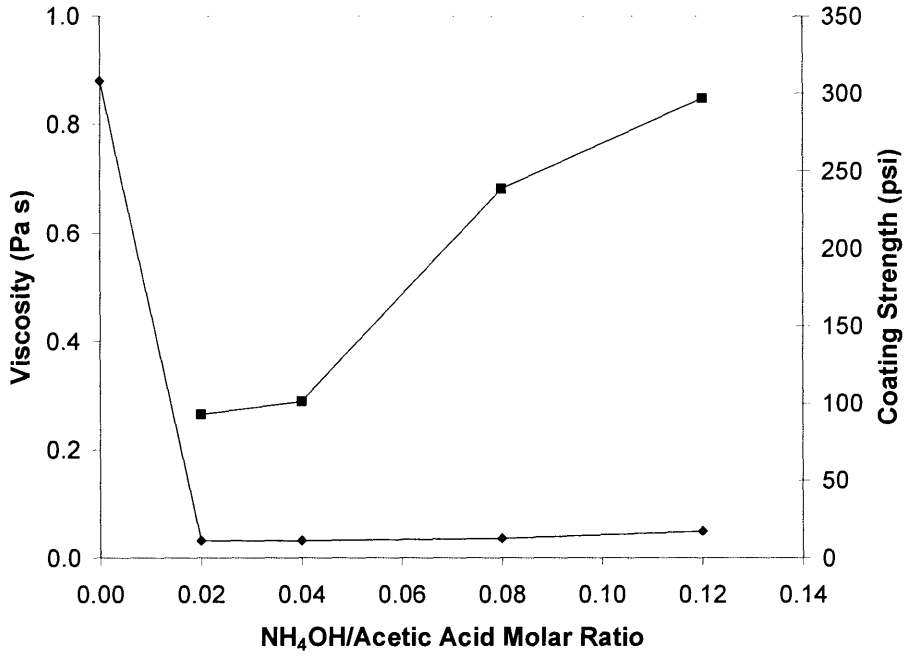

Figure 3.10. Viscosity (♦) and adhesion strength (■) of the 400°C-calcined SDC films as a function of the NH_4OH/acetic acid molar ratio in the MOD SDC acetate solution.

3.3.3. Colloidal Sol as Inorganic Binder for Thick Film Deposition

Beside the stability issue, MOD acetate solution gave rise to a low oxide yield when used as a binder. Thus, colloidal sol was developed as an alternative inorganic binder, given its high oxide yield and precursor density.

3.3.3.1. Synthesis of YSZ Colloidal Sol

Zirconia and yttria sols, as well as partially stabilized zirconia (e.g. 3 mol% yttria-stablized zirconia or 3YSZ) sols are commercially available. Typically, these sols are prepared by first precipitating the hydroxide at a pH of 8. After washing the precipitate, the powder is

peptized in nitric acid solution to create a stable sol [38]. The nitric acid digests the particles as well as provided the required surface charge for the dispersion. In the extreme, the acid might produce a zirconium oxynitrate, a commercially available zirconium salt precursor. Thinking of the zirconia sols as oligormerized nitrate salts would be fairly accurate for the fine particulate dispersions. The nitrate-to-zirconium molar ratios for Zr10/20 and the oxynitrate salt precursor are 1 and 2, respectively.

We have developed a technique for producing YSZ sol without using an acid peptization step. This was important in retaining a mixed oxide dispersion since treatment of precipitate in hot acid might preferentially etch away the yttrium component [39]. In our study, precipitation of metal(III) nitrate with a basic hydroxide (BOH) was employed as the starting point,

$$M^{+3}(NO_3)_3 + (3+x)BOH \rightarrow M^{+3}(OH)_3 \downarrow + (3+x)B^+ + 3NO_3^- + xOH^- \qquad (7)$$

By limiting the excess base, x, we could attempt to precipitate the hydroxide with excess nitrate ligands to mimic the composition of a zirconia sol. This was facilitated by precipitating in a medium with low dielectric constant, for example by combining a near-saturated aqueous salt solution with an organic base solution (e.g. tetraethylammonium hydroxide (TEAH) in isopropanol). This approach was first developed to precipitate LSM with the desired stoichiometry [40]. The low dielectric constant of the precipitation medium prevented strontium hydroxide solubilization, which would have occurred in an aqueous medium.

To select the appropriate excess base, a titration curve was generated for 8YSZ using TEAH. Various base concentrations were examined and normalized to the base concentration required to achieve a pH of 10 (see Table 3.2) [41,42].

Table 3.2. Base equivalent and the respective final pH based on titration.

Base Equivalent	0.80	0.85	0.90	0.95	1
Final pH	5.1	5.9	7.0	8.3	10

For the precipitation experiment, a 2.25 M salt solution was added to different base equivalents of 0.4 M TEAH in isopropanol. A hydroxide suspension was formed upon rinsing in methanol, but it was difficult to collect with centrifugation. Figure 3.11 shows that the deagglomerated precipitates have average particle sizes of 50 nm and 110 nm at base equivalents of 0.80 and 0.90, respectively. Thermogravimetric analysis (TGA) determined the oxide yield

and the nitrate content for the latter precipitates (base equivalent = 0.9) to be 71 wt% and ~ 17 wt%, respectively. In comparison, the Zr100/20 commercial sol has an oxide yield of 81 wt% and a nitrate content of 11 wt%, while the zirconium oxynitrate salt has an oxide yield of only 40 wt%.

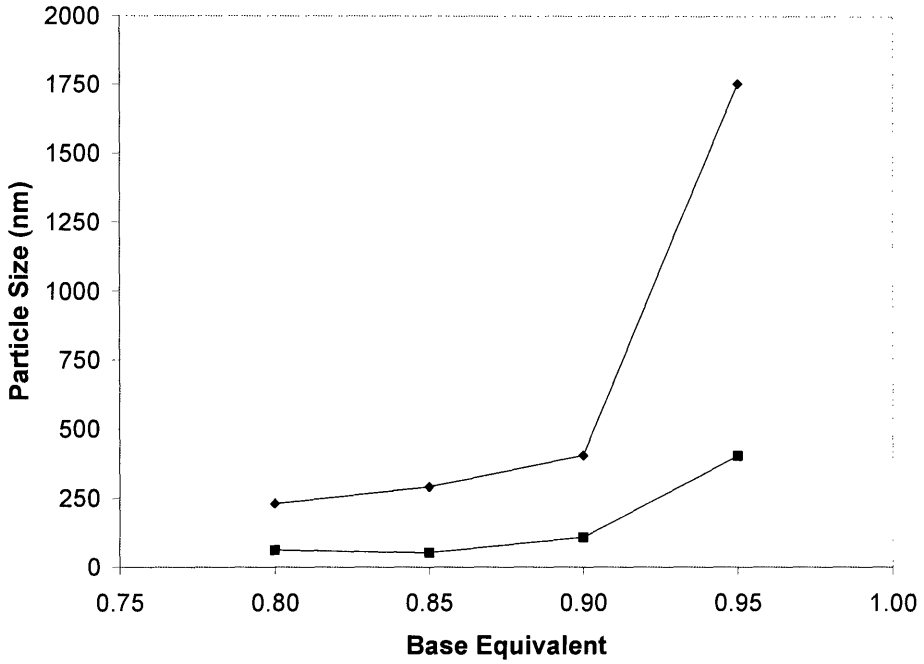

Figure 3.11. Particle size of YSZ precipitates achieved at different base equivalents, measured (♦) for the centrifuge supernatant and (■) after resuspension with a homogenizer.

3.3.3.2. YSZ Colloidal Sol as Inorganic Binder for LSCF

Three YSZ suspensions were investigated for use as an inorganic binder. First, a YSZ suspension was prepared using the techniques developed in Section 3.3.3.1. Additionally, two other suspensions were prepared by mixing commercially available zirconia sols (Nyacol 10/20 or 100/20) with a yttria sol (Nyacol Y10/14) to obtain a final sol composition of 8YSZ.

Poor film adhesion was observed when YSZ colloids with coarser grains were used. Good film adhesion was obtained only when the yttria sol was mixed with the fine-grained zirconia sol, Zr10/20. The yttria sol was found to destabilize the Zr10/20 sol. Figure 3.12 shows that the minimum gelation time was obtained for a mixed zirconia and yttria sol with ~ 13.75 wt% or 8 mol% yttria. Such gel transformation has been shown to be effective in silica systems towards stabilizing composite structures [43].

In the optimized thick-film deposition, low surface area LSCF oxide powder was dispersed in the zirconia sol with a small amount of ethylene glycol (which was added to slow the drying process for gelation to occur). The yttria sol was then added, and the slurry was applied to the substrate. The slurry contained 70 wt% LSCF oxide powder, 21 wt% Zr10/20 sol, 4.8 wt% Y10/14 sol, and 4.2 wt% ethylene glycol. The YSZ binder loading in the calcined film was 6.5 wt%.

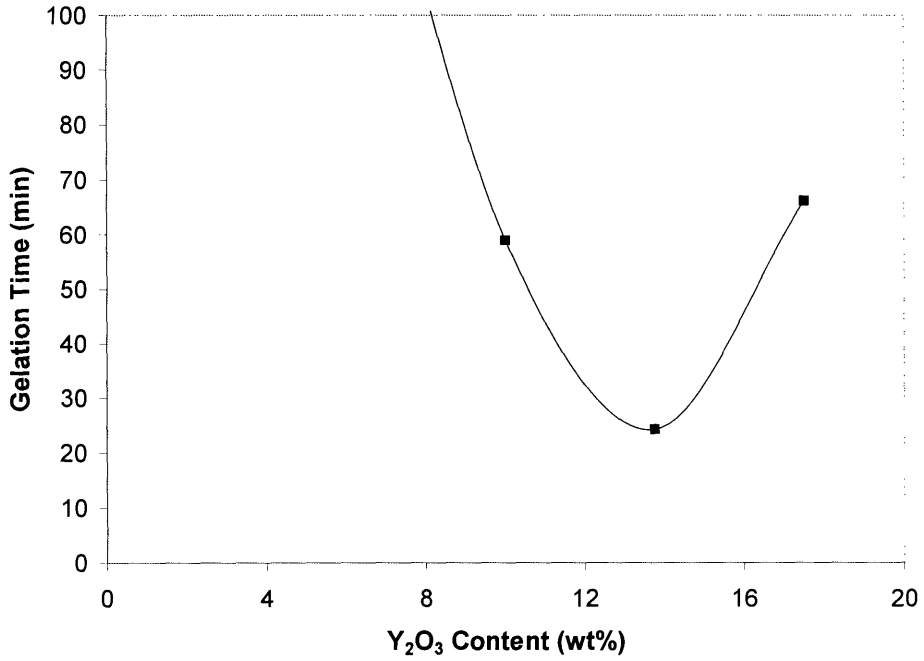

Figure 3.12. Gelation time for mixed zirconia and yttria sols with different yttria contents.

3.3.3.3. Deposition and Properties of LSCF/YSZ Thick Films

Compared to the MOD-based slurries, the YSZ-based inorganic binder gave rise to superior film adhesion. Since the typical composite cathode involved a 50:50 mixture of YSZ and LSCF by weight, the YSZ loading in our cathode film could be increased by using a mixture of LSCF and YSZ oxide powders. Two different YSZ powders were selected, one with a median particle size of 8 μm and another with a finer particle size of 0.4 μm. Figure 3.13 shows that the film adhesion on glass was optimized when a fine-grained YSZ powder loading of 20 wt% was used in the LSCF/YSZ composite film. A higher loading (30 wt%) of fine-grained YSZ powders actually led to a reduced film adhesion strength, possibly due to the lower packing density of this YSZ powder.

SEM indicated the presence of cracks in composite cathode films containing fine-grained YSZ. Cracking was avoided by using coarse-grained YSZ powder for the composite films (see Figure 3.14). Films of ~ 100 μm in thickness were achieved successfully by this approach.

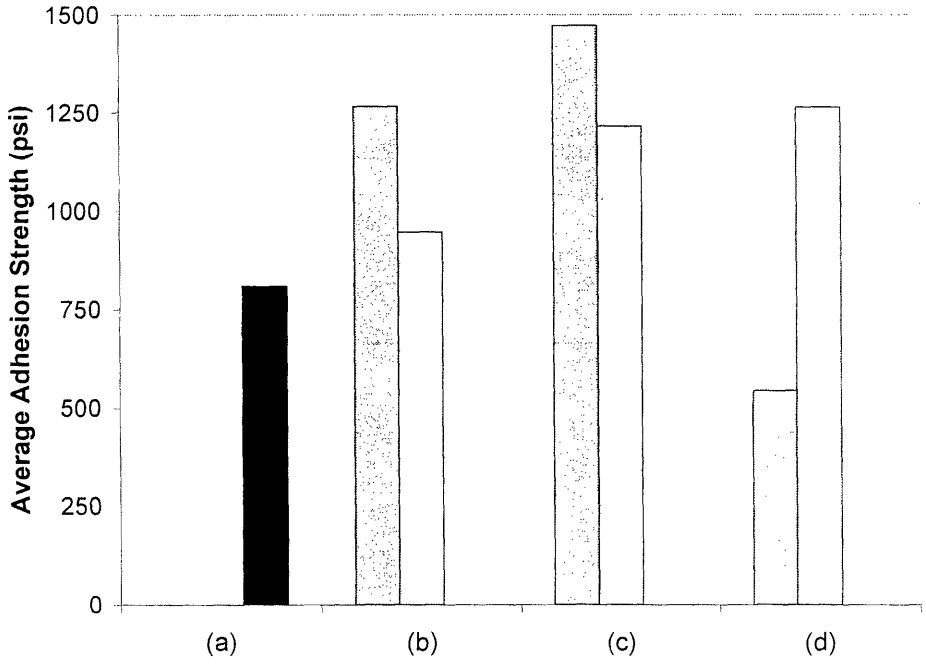

Figure 3.13. Adhesion strength of 550°C-calcined LSCF/YSZ composite films containing (a) 0 wt%, (b) 10 wt%, (c) 20 wt% and 30 wt% YSZ, prepared without YSZ (black), with 0.4-μm YSZ (dark grey), and with 8-μm YSZ (light grey).

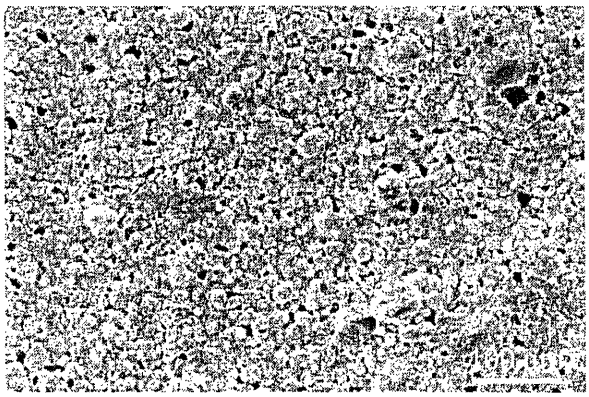

Figure 3.14. Surface morphology of a 550°C-calcined, thick LSCF/YSZ film produced with 30 wt% coarse-grained YSZ.

As the original motivation for studying thick films was to prevent large ohmic losses, the electrical conductivity of LSCF/YSZ composite films was measured at 300°C to determine their

suitability for μSOFC applications (Figure 3.15). Compared to pure LSCF film, LSCF/YSZ composite films showed a much lower conductivity when fine-grained YSZ was used. Although this was expected with YSZ being an electrical insulator, it was more likely due to the presence of cracks in the latter. In contrast, LSCF/YSZ composite films with 10 wt% and 20 wt% loadings of coarse-grained YSZ demonstrated higher conductivity than the pure LSCF film. This could be attributed to the absence of film shrinkage and cracking in these composite systems.

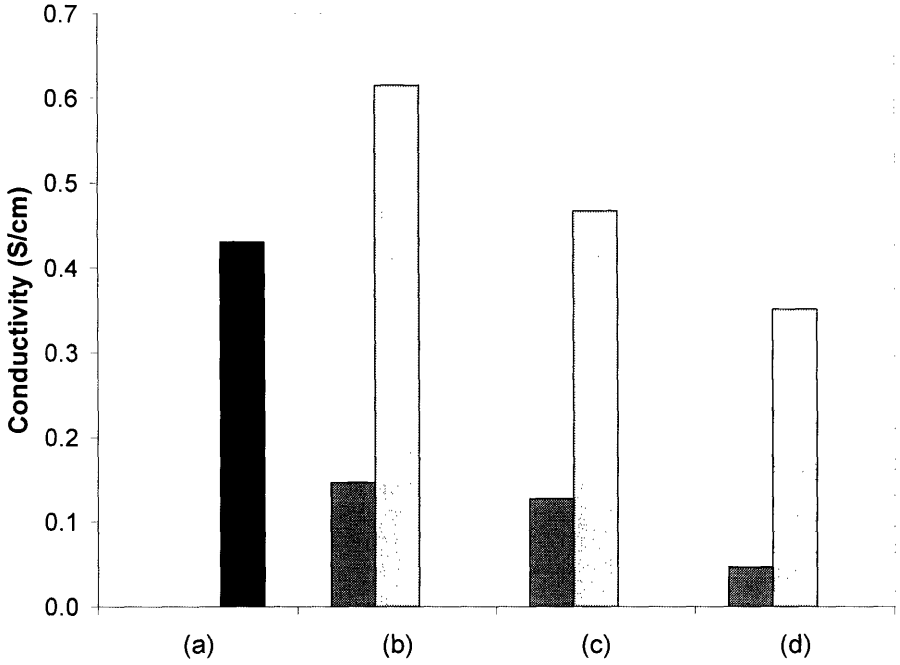

Figure 3.15. Electrical conductivity of the 550°C-calcined LSCF/YSZ composite films containing (a) 0 wt%, (b) 10 wt%, (c) 20 wt% and 30 wt% YSZ, prepared without YSZ (black), with 0.4-μm YSZ (dark grey), and with 8-μm YSZ (light grey).

This study showed that colloidal YSZ sol worked successfully as an inorganic binder in promoting LSCF film adhesion below its sintering temperature. The optimized system provided for adhesion strengths of over 1450 psi on glass. However, only moderate electrical conductivity was observed (< 1 S/cm), indicating the poor electrical contact of the LSCF particles in the film. Dense LSCF has a conductivity of ~ 100 S/cm at 300°C. Thus, partial sintering of the LSCF powder might be necessary to promote good contact between the LSCF particles in the film. In summary, the wet-chemical methods developed would not be able to produce suitable μSOFC cathode materials if restricted to the existing semiconducting oxide formulations.

3.3.4. Development of Noble Metal Films for μSOFC Electrodes

Traditional cathode materials show minimal oxygen conductivity at the low operating temperatures of the μSOFC. A porous Pt film could be a much more viable electrode material for the μSOFC system. It would allow an ultrafine catalytic material to be intimately mixed with the electrolyte to produce a significant volume fraction of triple-phase boundaries. Furthermore, the thin film material could be much less costly than the conventionally prepared material. Commercial Pt paints could be used to produce highly porous films (see Figure 3.16), but their Pt particle size would be ~ 10 times larger than the thickness of the sputtered YSZ electrolyte; this would not be suitable for μSOFC applications.

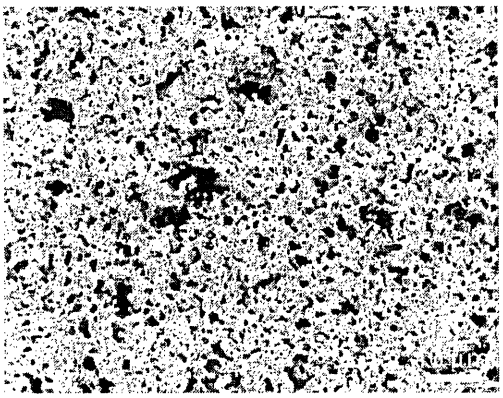

Figure 3.16. Porous Pt film produced from commercial Pt paint.

Therefore, a new approach was developed to obtain a Pt film with finer pore size but similar porosity. It involved the use of Pt and Ni resinates, which were diluted with a co-solvent (dichloromethane), without which these incompatible resinates would precipitate. The mixed resinates were then spin-coated onto a substrate as a film of ~ 540 nm-thick (Figure 3.17(a)). After calcining the film at 550°C, Ni was etched away in hot nitric acid to generate a fine porosity in the coating (see Figure 3.17(b)). EDX analysis illustrated the removal of the Ni component after acid etching (see Figure 3.18).

The incompatibility of the metal components was essential in this approach. For example, Cu was found to form an alloy with Pt upon calcination. It was then impossible to etch Cu away significantly in hot nitric acid to yield porosity in the film.

The porous Pt film produced by etching Ni porogen showed a mirror finish and metallic conductivity. This porous film was also deposited onto a 100 μm-thick YSZ electrolyte for potential μSOFC applications. Preliminary experiments indicated that the area-specific

resistance of the nanoporous Pt films was 1–2 orders of magnitude lower than films derived from the traditional Pt paints for cathode applications.

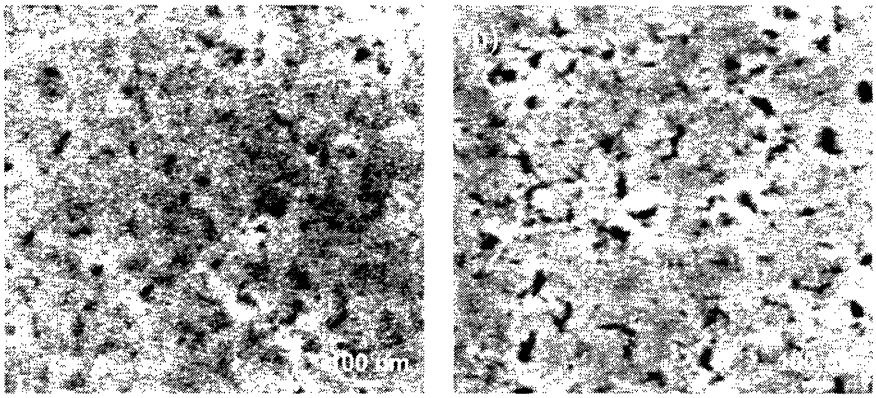

Figure 3.17. Thin Pt-Ni film (a) before and (b) after etching away Ni in nitric acid.

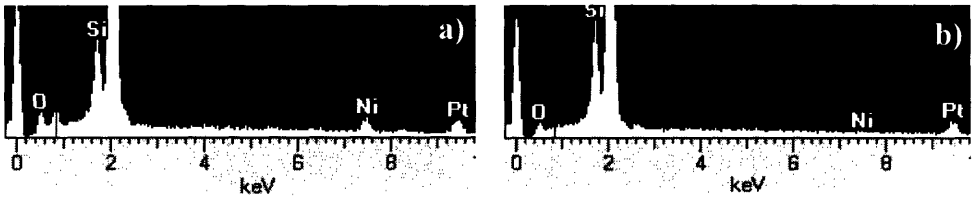

Figure 3.18. EDX spectrum of the thin Pt-Ni film (a) before and (b) after etching away Ni in hot nitric acid.

3.3.5. Polymer-Templated Porosity in Sputtered Films

To develop fine porosity in films using semiconductor processing techniques, a porous polymer template was created for use with sputtering. Porous polymer templates have been created by using di-block and tri-block copolymers, which are very expensive [44,45]. Therefore, we have developed cheaper alternatives based on the phase segregation between polystyrene and polymethylmethacrylate (PMMA) [46]. Toluene was used as a co-solvent for a 50:50 mixture of polystyrene (MW = 350,000) and PMMA (MW = 15,000) (by weight) at 1 wt% total polymer loading. The solution was filtered and spin-coated onto a Si substrate at 2000 rpm. The resulting film was dried overnight in vacuum at 50°C. The polystyrene phase was removed by exposing the dried film to cyclohexane. The resulting porous PMMA film is illustrated by AFM in Figure 3.19. The porous polymer template could be used for producing the next generation of sputtered Pt/YSZ composite electrodes.

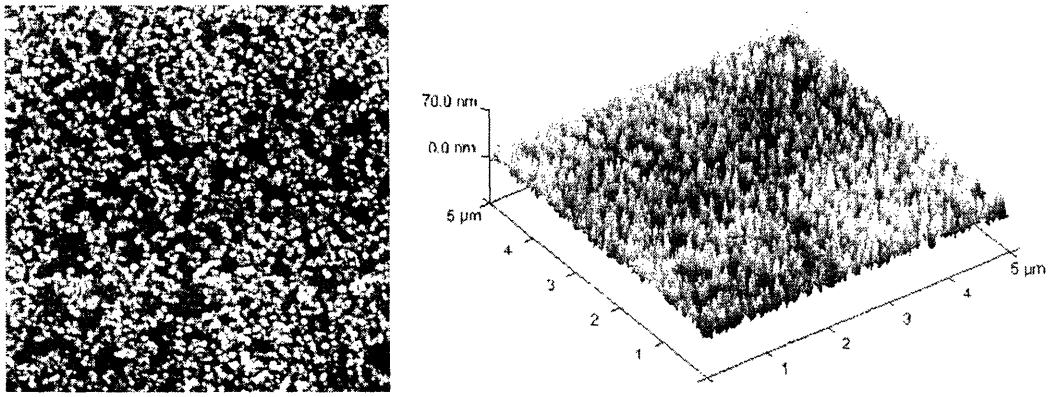

Figure 3.19. AFM image of a porous PMMA film (image area: 5 µm x 5 µm).

3.4. Conclusions

Several experimental techniques have been developed for materials processing that might be suitable for µSOFC applications. The goal was to improve the microstructure and/or composition of current electrode materials, instead of just relying on reducing electrolyte thickness to increase power output at low temperatures. Initially, traditional binder systems were explored for this purpose, but the processing temperatures required were too high for device compatibility. Thus, an inorganic binder technique was developed to promote adhesion of the desired cathode materials below the traditional firing temperatures. Metallorganic precursors worked quite well, but were limited in applicability due to the high acidity and low stability of these systems. Colloidal zirconia sols were then explored as an inorganic binder. Its gelation was promoted by destabilizing the zirconia sol with the addition of a yttria sol. The resulting LSCF/YSZ composite thick films have an adhesion strength exceeding 1450 psi. However, such films would require high-temperature sintering to achieve high conductivities, and as such, were limited in compatibility with µSOFC applications.

To attain high conductivities at low temperatures, porous noble metal films were developed. With their high electrochemical activity, these films showed excellent potential for use with YSZ electrolytes. Porous polymer templates were also developed to assist the fabrication of similar films using semiconductor processing techniques, such as sputtering.

3.5. References

[1] Maynard, H.L., Meyers, J.P., *J. Vac. Sci. Technol. B* **20**, 1287 (2002).
[2] Jankowski, A.F., Graff, R.T., Hayes, J.P., Morse, J.D., "Solid Oxide Fuel Cells VI," p. 32, Electrochemical Society, New Jersey, 1999.
[3] DeSouza, S., Visco, S.J., DeJonghe, L.C., *Solid State Ionics* **98**, 57 (1997).
[4] Steele, B.C.H., Heinzel, A., *Nature* **414**, 345 (2001).
[5] Will, J., Mitterdorfer, A., Kleinlogel, C., Perednis, D., Gauckler, L.J., *Solid State Ionics* **131**, 79 (2000).
[6] Baertsch, C.D., Jensen, K.F., Hertz, J.L., Tuller, H.L., Srikar, T.V., Spearing, S.M., Schmidt, M.A., *J. Mater. Res.* **19**, 2604 (2004).
[7] Seabaugh, M., Swartz, S.L., US Patent Application 20030027033, 2003.
[8] Kuma, T., Higashi-Ku, M., Fukoka-Ken, F., US Patent 5,194,414, 1993.
[9] Agrafiotis, C., Tsetsekou, A., *J. Eur. Ceram. Soc.* **22**, 423 (2002).
[10] Murrell, L.L., *Catal. Today* **35**, 225 (1997).
[11] Monaco, S.J., Ko, E., *Chem. Mater.* **9**, 2404 (1997).
[12] Goebbert, C., Nonninger, R., Aegerter, M.A., Schmidt, H., *Thin Solid Films* **351**, 79 (1999).
[13] Baratto, C., Lottici, P.P., Bersani, D., Antonioli, G., Gnappi, G., Montenero, A., *J. Sol-Gel. Sci. Techn.* **13**, 667 (1998).
[14] Frost, R.L, Dutt, S.M., *J. Colloid. Interf. Sci.* **198** (1998) 330.
[15] Kundu, D., Manna, T., De, G., *J. Sol-Gel. Sci. Techn.* **23**, 145 (2002).
[16] Woodhead, J.L., US Patent 3,761,571, 1973.
[17] Klein, L.C., "Thin Film Processes II," p. 501, Academic Press, Boston, 1991.
[18] Schwartz, R.W., *Chem. Mater.* **9**, 2325 (1997).
[19] Yi, G., Sayer, M., *Am. Ceram. Soc. Bul.* **70**, 1173 (1991).
[20] Ozer, N., Cronin, J.P., Akyuz, S., *Proc. SPIE.* **3788**, 103 (1999).
[21] Liu, M., Wang, D.S., *J. Mater. Res.* **10**, 3210 (1995).
[22] Mehrotra, R.C., "Metal Carboxylates," p. 12, Academic Press, London, 1983.
[23] McIntrye, P.C., Cima, M.J., Smith, J.A., Hallock, R.B., *J. Appl. Phys.* **71**, 15 (1992).
[24] Shao, Z., Haile, S.M., *Nature* **431**, 170 (2004).
[25] Ralph, J.M., Schoeler, A.C., Krumpelt, M., *J. Mater. Sci.* **36**, 1161 (2001).
[26] Dusastre, V., Kilner, J.A., *Solid State Ionics* **126**, 163 (1999).
[27] Catania, P., Hovnanian, N., Cot, L., *Mater. Res. Bull.* **25**, 631 (1990).
[28] Virkar, A.V., "Polarization in Anode-Supported Solid Oxide Fuel Cells," Boston University Emerging Technology Seminar, May 30th, 2003.
[29] Fleig, J., *Annu. Rev. Mater. Res.* **33**, 361 (2003).
[30] Teraoka, Y., Honbe, Y., Ishii, J., Furukawa, H., Moriguchi, I., *Solid State Ionics* **152**, 681 (2002).
[31] Teraoka, Y., Zhang, H.M., Okamoto, K., Yamazoe, N., *Mater. Res. Bull.* **23**, 51 (1988).
[32] Li, X., Zou, Y.Q., Zheng, B., Hu, H.M., *Acta. Cryst.* **C60**, M197 (2004).
[33] Ekstrom, L., Olin, A., *Chemica Scripta.* **13**, 10 (1978).
[34] Baker, E.N., Baker, H.M., Anderson, B.F., Reeves, R.D., *Inorganica Chimica Acta* **78**, 281 (1983).
[35] Kragten, J., Decnop-Weever, L.G., *Talanta* **25**, 147 (1978).
[36] Biedermann, G., Newman, L., *Arkiv. Kemi.* **22**, 303 (1964).
[37] Haertling, G.H., *Ferroelectrics* **116**, 51 (1991).

[38] Chen, K.L., Chiang, S.T., Tsao, H.K., *J. Nanopart.* **3**, 119 (2001).
[39] Kato, E., Hirano, M., Kobayashi, Y., Asho, K., Mori, M., Nakate, M., *J. Am. Ceram. Soc.* **79**, 972 (1996).
[40] Sangar, N., "Nanocrystalline Perovskites for Catalytic Combustion and Oxygen Separation," Ph.D. Thesis, Massachusetts Institute of Technology, 2002.
[41] Rasmussen, M.D., Akinc, M., Hunter, O., "Processing of Metal and Ceramic Powders," Metallurgical Society of AIME, Warrendale, 1982.
[42] Fokema, M.D., Chiu, E., Ying, J.Y., *Langmuir* **16**, 3154 (2000).
[43] Morris, C.A., Anderson, M.L., Stroud, R.M., Merzbacher, C.I., Rolison, D.R., *Science* **284**, 22 (1999).
[44] Shin, K., Leach, K.A., Goldbach, J.T., Kim, D.H., Jho, J.Y., Tuominen, M., Hawker, C.J., Russell, T.P., *Nano. Lett.* **2**, 933 (2002).
[45] Hamley, I.W., *Nanotechnology* **14**, R39 (2003).
[46] Li, X., Han, Y., An, L., *Polymer* **44**, 8155 (2003).

Chapter 4 – Novel Anode Materials for Direct Hydrocarbon Solid Oxide Fuel Cells

4.1. Introduction

Fuel cell systems powered by hydrogen present a great deal of limitation. No hydrogen fuel distribution network exists currently, and hydrogen storage has been a major materials and engineering challenge [1]. The fuel cell power plant currently consists of fuel reformers, fuel cell stacks, and power conditioners. Eliminating the reforming units may present significant benefits in cost savings and energy efficiency. Unlike polymer electrolyte membrane (PEM) fuel cells, solid oxide fuel cells (SOFC) do have the potential to operate on any fuel. This has not been achieved from a practical standpoint, and current SOFC operates on reformate gases. The latter is derived from steam reforming or partial oxidation of hydrocarbons, and comprises of carbon oxides, hydrogen and steam or nitrogen diluents. The main obstacle to utilizing a dry hydrocarbon feed for SOFC power generation is the high nickel content in the traditional anode ceramic/metal composites (cermets). This material undergoes rapid coking, which is exacerbated at elevated temperatures in the absence of steam. Mitigating the coking problem would enable a much simpler SOFC design.

There are two approaches to direct hydrocarbon SOFC. In the internal reforming SOFC, sufficient steam is co-fed with the hydrocarbon fuel to minimize coking. This system is based on insights from industrial methane reforming to produce hydrogen over supported nickel catalysts. Internal reforming dilutes the fuel content in the anode stream, and introduces large endotherms that create mechanical stresses in the SOFC membrane [2].

Direct oxidation SOFC employs hydrocarbons (typically methane) without steam addition. This nomenclature is complicated in that a dry hydrocarbon feed can still rely on steam to mitigate coking problems. Under normal fuel cell operation, high current flows introduce oxygen into the anode layer to produce sufficient carbon dioxide and water *in situ* to prevent coking. This concept has been shown to be effective on fuel cells with Ni/yttria-stabilized zirconia (YSZ) anodes operating on humidified methane at 800°C [3]. The otherwise stable fuel cell would break in 10 min in the absence of the current flow. At lower temperatures, the fuel cell would survive slightly longer as coking would be less severe.

Efforts on direct oxidation SOFC are focused on replacing the nickel metal in the anode, for example with a Cu/ceria cermet [4]. Higher hydrocarbons such as decane have been used as

fuels successfully at 700°C [5]. Since copper and its oxide would melt below typical SOFC fabrication temperatures, the dense YSZ electrolyte in this system is fabricated on a porous YSZ host. The host is then impregnated with copper and cerium nitrates and calcined; numerous cycles of impregnation and calcination are needed to achieve the desired structure.

This study is devoted to the development of novel anode materials for the direct oxidation SOFC. The goal is to allow for the direct use of methane feed to simplify the balance of plant. This would also minimize energy and capital requirements by removing the heat-exchange equipment required for creating and recuperating large quantities of steam. The ideal anode material should have good low-temperature activity, good electronic and ionic conductivity, and a thermal expansion coefficient similar to the YSZ electrolyte. It should be able to be oxidized between runs, unlike the Ni-based system that requires shutdown in an inert atmosphere. We have developed various metallic and ceramic anodes without using complex, unconventional fabrication methods. The optimized anode systems were tested for power production from hydrogen and methane feeds.

4.1.1. Electrochemical and Architecture Requirements of Direct Hydrocarbon Anodes

4.1.1.1. Implication of Gas-Phase Pyrolysis on SOFC Architecture

Operating on a dry hydrocarbon fuel presents a major challenge to the SOFC anode design. Considerable gas-phase pyrolysis of hydrocarbons takes place above 800°C [6]. This must be avoided as entrained particulates are expected to damage the SOFC structures and limit the stack lifetime. Thus, the SOFC operating temperature has to be lowered from the traditional range of ~ 1000°C to 600–800°C. The lower operating temperature in turn necessitates the use of ultrathin electrolyte to achieve good performance [7] (see Figure 3.1).

Three general SOFC planar architectures are possible (see Figure 4.1). The simplest design involves an electrolyte-supported stack, which is achieved by tape casting and sintering of a thick YSZ electrolyte, followed by screen-printing of the electrodes.

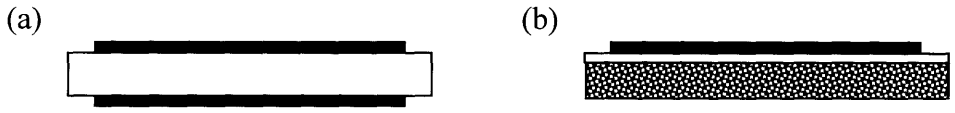

Figure 4.1. (a) Electrolyte-supported and (b) electrode-supported architectures.

In cathode-supported SOFC, a 1–2 mm-thick cathode is used to support a 10–40 μm-thick electrolyte. The electrolyte is introduced by chemical vapor deposition (CVD) [8] onto a sintered $La_{0.8}Sr_{0.2}MnO_3$ (LSM) tube.

In the anode-supported SOFC, the anode provides the support for a thin YSZ electrolyte. This design is the most feasible from a fabrication standpoint since NiO/YSZ composite can be co-fired to the sintering temperature of the YSZ electrolyte without undesired interfacial reactions. Commercially, laminates of anode and electrode tapes are used to produce such stacks. The cathode is subsequently applied at a lower temperature to prevent interfacial reactions. On the laboratory scale, YSZ dispersions are applied to the NiO/YSZ support and then co-fired [9]. Porosity in the support is introduced upon reducing NiO to Ni metal.

We will focus on developing anode-supported SOFC since it does not require special fabrication techniques, such as CVD, and allows for ultrathin electrolyte to be generated. This approach, however, places stringent requirements on the anode material in terms of both mechanical and electrochemical performances. The selected material should not react with YSZ at the 1400°C sintering temperature. It cannot melt or lose porosity, and must match the thermal expansion coefficient of the electrolyte.

4.1.1.2. Electrochemical Requirements of the Anode System

The anode has three roles in the electrochemical oxidation of the fuel. First, it must conduct oxygen ions from the electrolyte to the reaction zone. Secondly, it must conduct the electrons produced from oxidation to the current collector. Thirdly, it must possess high catalytic activity. No single material has satisfied all these requirements; thus, most anode systems typically involve composite materials.

In the Ni/YSZ cermet, the only region that is capable of oxidizing the fuel is the triple-phase boundary (illustrated by the black dots on either side of the metal clusters in Figure 4.2(a)). The reaction is limited to this region because it requires both oxygen ions and electrical conduits for the hydrogen anode reaction,

$$O^{2-} + H_2 \rightarrow H_2O + 2e^- \qquad (1)$$

The nickel metal conducts the electrons produced from the electrochemical oxidation. It is impervious to the fuel and oxy-anions. The electrolyte, an electrical insulator, provides the oxy-anions for the combustion. Porosity is required to supply the fuel, thus limiting the reaction zone

as depicted. The performance of anode cermets can be improved with the addition of a mixed ionic and electronic conductor (MIEC) (Figure 4.2(b)). Since the mixed conductors can conduct both oxy-anions and electrons, the complete electrochemical oxidation can occur on their surfaces, greatly expanding the active zone. A suitable MIEC material has to be stable under the highly reducing atmosphere present at the anode. The most promising mixed conductors for such application are ceria-based materials.

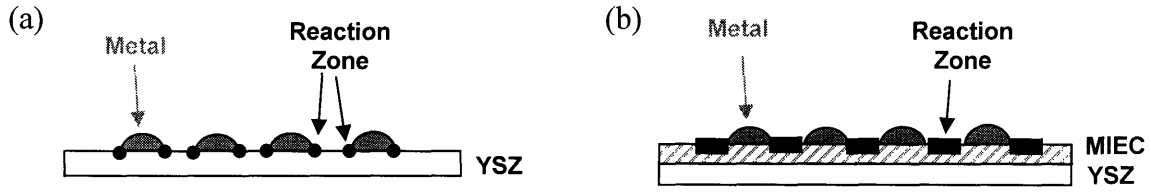

Figure 4.2. Schematic of (a) a conventional cermet anode, and (b) a cermet anode made from a MIEC material.

4.1.2. Potential Anode Materials

4.1.2.1. Ceria

Ceria has been used in both the cathode and the anode of SOFC. It has also been employed as a low-temperature electrolyte. It is often applied as a buffer layer between the YSZ electrolyte and a reactive cathode composition [10]. For electrolyte applications, ceria is doped with Sm or Gd to provide good ionic conductivity with only minimal electronic conductivity below 700°C [11,12]. The electronic conductivity of ceria depends on its extent of reduction, and is 1 S/cm in reducing atmosphere at 1000°C [13]. Ceria has shown good activity as an anode for hydrogen, but not for methane [14], since it could be more effectively reduced by hydrogen. A maximum power output of 80 mW/cm^2 has been achieved at 1000°C for direct hydrocarbon applications with Gd-doped ceria anodes [15]; the YSZ electrolyte was 180 μm-thick, and a steam/methane ratio of 0.1 was employed.

Catalytic studies have demonstrated that the extent and rate of reduction of ceria can be increased with the addition of catalytic metals [16,17,18]. The oxygen ions from ceria are transferred to the metal surface where they react more readily with the reducing stream. A zirconia stabilizer is often added to fine-grained ceria to prevent rapid grain growth in reducing atmospheres [19,20]. Nanocrystalline ceria has demonstrated greater reducibility than coarse-grained ceria [21,22], leading to higher anode electrochemical activity.

For SOFC applications, the bulk reduction of ceria with hydrocarbons may require the use of metal catalysts. Indeed, Pt addition to ceria anode has led to good performance with methane [23]. This affect is complicated by the ability of the noble metal to crack methane to hydrogen at the reaction temperatures. Ceria-based anodes have to be as thin as 20 μm, and a metallic current collection layer is required to avoid large resistive losses. Thicker anode-supported cells would need a higher conductivity than that obtainable from a single-phase ceria.

4.1.2.2. Existing SOFC Perovskites

Researchers have examined perovskite cathode materials and interconnect materials as anode materials. Sr-doped lanthanum manganate (LSM) is the cathode material most stable against reduction. Undoped lanthanum manganate decomposes in reducing atmosphere at 720°C [24], and $La_{0.6}Sr_{0.4}Co_{0.2}Fe_{0.8}O_3$ (LSCF) has shown even lower stability [25]. Recent studies have attempted at stabilizing manganese in the perovskite structure with Cr addition at the B-site. The optimized anode composition, $La_{0.75}Sr_{0.25}Cr_{0.5}Mn_{0.5}O_3$, is stable in humidified 5% H_2 to 900°C [26].

Doped lanthanum chromate is known to be stable under anode conditions. As an interconnect material, it has demonstrated good electronic conductivity in both oxidizing and reducing atmospheres with good chemical stability. The catalytic activity of the chromates has been studied for anode applications [27]. Researchers have attempted to improve the activity of chromates by adding ruthenium oxide [28], but the chromate system has yet to demonstrate good anode performance [29]. Composite anodes of chromate and ceria have been examined with a 500 μm-thick ceria electrolyte [30]. A power density of 50 mW/cm^2 was achieved with methane at 750°C, which could be increased to 125 mW/cm^2 with the addition of nickel to the composite anode.

4.1.2.3. Membranes for the Oxidative Coupling of Methane

In oxidative coupling of methane, methane and oxygen react to produce methyl radicals that combine to form higher hydrocarbons and water. To minimize undesired combustion, mixed-conducting membranes have been used to introduce the oxygen along the reactor length. Typical membrane formulations include LSCF, (Y,Sm)-doped bismuth oxide, and $(Ba,Sr)(Co,Fe)O_3$ [31,32]. The membranes are designed to have an oxygen flux similar to that

required for methane conversion over an anode of low surface area. However, these materials would decompose to carbonates and base metals under the direct hydrocarbon SOFC conditions.

4.1.2.4. Strontium Titanate

Titanate-based perovskites represent another class of promising anode materials. La-doped $SrTiO_3$ has a thermal expansion coefficient similar to YSZ. It also has a high electronic conductivity when sintered in hydrogen [33], which is associated with the ability of Ti^{+4} to be reduced and stabilized in a +3 valence in a reducing atmosphere at high temperatures. Titanium is not reduced in an oxidizing atmosphere, and both the perovskite and the excess strontium oxide that segregates to the perovskite grains are insulating [34]. These reactions are represented in the following equations for 30 at% La doping at the A-site.

H_2: $0.15\ H_2 + 0.3\ LaO_{1.5} + 0.7\ SrO + TiO_2 \rightarrow La_{0.3}Sr_{0.7}Ti_{0.7}^{+4}Ti_{0.3}^{+3}O_3 + 0.15\ H_2O$ (2)

O_2: $0.3\ LaO_{1.5} + 0.7\ SrO + TiO_2 \rightarrow La_{0.3}Sr_{0.55}Ti^{+4}O_3 + 0.15\ SrO$ (3)

Constructing an anode-supported cell with strontium titanate would be difficult due to the processing required. YSZ cannot be sintered in a reducing atmosphere with strontium titanate. It also cannot be processed in an oxidizing atmosphere due to its expected reactivity with the segregated strontium oxide. Application of strontium titanate in an electrolyte-supported SOFC has produced a low power density of 15 mW/cm^2 [33]. However, greatly improved performance (170–700 mW/cm^2) was achieved by forming a composite anode of strontium titanate and ceria.

4.1.2.5. Vanadium and Niobium Oxides

Vanadate and niobate ceramics are also of interest for anode applications, but they do not possess appropriate mechanical properties. Strontium vanadate has an extremely high conductivity of 1000 S/cm in a reducing atmosphere, but decomposes in oxygen [35]. Niobium titanate (Nb_2TiO_7) has a conductivity of over 100 S/cm when reduced, but has a very low thermal expansion coefficient (3×10^{-6} mm/mm/K) [36].

4.1.2.6. Cermet Systems

The traditional anode material is a cermet, Ni/YSZ. Its power density is found to increase monotonically with the Ni loading [37]. The best anode-supported SOFC thus employs a graded anode structure [38]. The support comprises of 80 vol% metal, and the

electrochemically active layer consists of 60 vol% metal; these metal loadings are greater than those typically employed in an anode cermet (40 vol%) [39]. The active layer is attached to the electrolyte, creating a gradual reduction in thermal expansion coefficient from the support to the electrolyte, while providing for high power output. The high porosity, increased sinterability, and low mechanical strength associated with high Ni loadings are the weakness in this SOFC system.

Other metal systems have also been examined [40]. For application in an anode-supported design, the metals must have stable oxide forms to survive the conventional YSZ processing temperature. Copper, silver and gold would melt below the processing temperature; group IIIB, IVB, VB and IIIA metals are liquid or toxic. Only iron, cobalt and nickel are viable at conventional processing conditions. However, iron is difficult to remain reduced, and cobalt volatilizes too easily.

The porous host technique for anode development has enabled new metals to be tested. Gold-ceria has demonstrated similar performance as Cu/ceria [41]. Mixed metal combinations such as Cu-Ni alloy and Co-Ni composite have also been examined [42]. Coking was problematic in the Cu-Ni system [43]. Catalyst additives (such as gold and molybdenum) have also been explored in the Ni/YSZ cermet to increase the cermet's coke resistance [44].

4.1.3. Anode Design and Material Selection

To allow for direct hydrocarbon feeds, our anode design would substitute nickel with alternative electronic conductors that might be less prone to coking. Initial efforts were focused on conductive ceramics that would be more robust in reactor cycling than metallic systems. Chromate and titanate perovskites would be developed; they exhibit no physical changes upon reduction and oxidation, have the appropriate thermal expansion coefficient, and possess high electronic conductivity. These conductors would be mixed with ceria instead of YSZ to form a composite anode. Since reduced ceria has demonstrated electrochemical activity but insufficient conductivity, it might out-perform YSZ in this application. If required, transition metals would be added at low levels to promote ceria's reduction with hydrocarbon feeds.

To avoid interfacial reactions with YSZ and ceria, the strontium content in the ceramic conductors should be minimized. Therefore, the lanthanum chromate selected would utilize magnesium doping at the B-site rather than Sr doping at the A-site. Mg doping at the B-site

would also produce a lower thermal expansion coefficient ($9.5x10^{-6}$ mm/mm/K) that might counteract the higher thermal expansion ($12.3x10^{-6}$ mm/mm/K) of ceria [45]. For this formulation, La doping of ceria might occur, but should lead to improved reducibility [23,46,47]. However, La doping would give rise to lower ionic conductivity than conventional dopants [11].

For the titanate system, La-doped calcium titanate was selected over La-doped strontium titanate. This was because the segregated calcium oxide during oxidative sintering would be less reactive with YSZ. Secondly, calcium titanate has demonstrated a high conductivity even after oxidative sintering and subsequent reduction at 900°C [48]. This has not been reported for the strontium titanate system. In fact, it has been debated whether complete strontium insertion could occur once this structure has been air-fired due to the very low cation mobility [49]. For application in an anode-supported cell fired in an oxidative environment, the La-doped calcium titanate was expected to be a better anode candidate than La-doped strontium titanate.

Finally, an alloy system would be developed for the cermet anode for direct hydrocarbon SOFC. The key in this design would be to minimize coking, which was the major problem with the nickel-based system. Nickel would incorporate carbon at high temperatures to form nickel carbide. The carbon would then be expelled as a crystalline carbon whisker [50]. To prevent such carbide formation, a nickel alloy with tin would be developed. Tin is in the same column as carbon in the periodic table. Tin alloying with nickel might suppress the high-temperature carbide formation, thus preventing the whisker formation.

Tin and other elements have been introduced to nickel catalyst to reduce coke formation in the steam reforming of methane [51] (see Table 4.1). For anode-supported SOFC, the oxide form of the additives must not melt below YSZ's sintering temperature (1400°C). Zinc and tin oxides have sufficiently high melting points, but zinc oxide is highly volatile and might cause desintering. Tin oxide is quite stable, but metallic tin has a low melting point. However, alloys containing $\leq$ 40 mol% tin would not melt below 850°C [52]. Tin doping might also improve the sulfur tolerance of the anode material [53].

Anode-supported SOFC would be developed for the chromate, titanate and Ni-Sn alloy systems. As traditional ceramic processing would be employed, the anode formulation must be highly compatible with YSZ processing and not react with the electrolyte. The anode must also have sufficient electrical conductivity with well-matched mechanical properties in support of the ultrathin electrolyte.

Table 4.1. Material properties of potential anode additives to improve the coke tolerance of Ni/YSZ cermets.

Dopant (1 at%)	Pt	Ir	Cu	Ag	Zn	Ge	Sn	Pb	As	Sb	Bi
Coke Mitigation [52]				+	+		+	+	+	+	+
Oxide Melting Point (°C)			1235		1975	937	1630	886	312	656	860
Metal Melting Point (°C)	1772	2410	1083	962	420	1086	232	328	613s	631	271

4.2. Experimental

4.2.1. Synthesis

Nickel oxide and tin oxide were obtained from J.T. Baker and Alfa Aesar, respectively. $(La_{0.8}Sr_{0.2})_{0.98}MnO_3$, LSM and La-doped calcium titanate ($La_{0.2}Ca_{0.8}TiO_{3.1}$) were obtained from Praxair Specialty Oxides with a median particle size of 0.8 μm. Alfa Aesar glassy carbon particles (20–50 μm) were used as the porogen for the support. Carbon black, Cabot BP-120, was used to create fine porosity in the electrochemical active layer. YSZ powders were obtained from Unitec and Tosoh (see Table 4.2). Tosoh powders are hard agglomerates of fine crystallites, whereas Unitec powders are dense fragments with higher tapping densities. High tapping density would facilitate a high green density for wet-coated laminates, reducing their shrinkage during densification. The densification temperatures listed in Table 4.2 referred to those observed for thin films deposited on anode supports that were not pre-sintered. The shrinkage resulting from anode densification would facilitate YSZ sintering. Thick ceramic preforms of YSZ would tend to require slightly higher sintering temperatures than anode-supported YSZ.

Table 4.2. Characteristics of commercial YSZ powders prepared by grinding (Unitec) and chemical coprecipitation (Tosoh).

Source	Average Size (μm)	Tapping Density (g/ml)	Densification Temperature (°C)
Tosoh 8YS	0.4	1.6	1350
Unitec-1	0.28	1.8	1350
Unitec-2	0.65	2.1	1400
Unitec-10	1.73	2.5	> 1450

Tosoh 8YS and Unitec-10 YSZ were used for the anode preparation. YSZ particle size has been shown to affect the conductivity, stability, porosity, strength, reoxidation ability and

thermal expansion of nickel/YSZ cermets [54,55,56]. For the electrolyte and cathode processing, Unitec-1 YSZ powder was preferred over the Tosoh 8YS YSZ powder.

Lanthanum chromate anodes were synthesized by coprecipitation of the nitrate precursor solution (0.2 M, Sigma). To prepare a composite, cerium salts were added to the lanthanum chromate precursor solution. The nitrate solution was slowly added to an aqueous tetraethylammonium hydroxide (TEAH) solution (35 wt%), which was dissolved in isopropanol (0.2 M). TEAH was used to precipitate the composite because ammonium hydroxide would complex with transition metal hydroxides and the alkaline bases would introduce metal impurities (e.g. Na). After aging for over 24 h, the particles were collected, rinsed several times in isopropanol, and dried. The samples were then fired to 800°C, unless surface area modifications were required to control support shrinkage.

In preparing Sm-doped ceria, the metal nitrate precursor solution (0.8 M) was first added to a 0.4 M TEAH solution in isopropanol. The base-to-nitrate molar ratio was 1.5 based on the +3 valence state of the cerium salt. The mixture was aged for 30 min and centrifuged. The precipitate collected was rinsed three times in methanol using an IKA homogenizer. After the third rinse, the well-dispersed hydroxide suspension became difficult to centrifuge. After redispersion, the slurry was added to the chromate precipitate in methanol, and homogenized for 10 min.

For the SOFC tests, the anode support material was milled with a carbon pore former and polyvinyl butyral (PVB) binder, pressed uniaxially into a pellet, and calcined at 1000°C to provide for green strength. A slurry of the anode material was prepared by ball milling, and was applied with an air brush onto the anode support to serve as the electrochemical active layer, which was then calcined to 1000°C. Lastly, a dispersion of YSZ electrolyte was prepared by ball milling, and was applied with an air brush. The resulting half-cell was then densified at 1350–1450°C in a box furnace. Subsequently, the cathode material was ball-milled, applied with an air brush, and subjected to 1-h calcination at 1250°C. A mask was used to limit the cathode's electrochemical area to a diameter of 0.5". The slurry was metered with a syringe pump to obtain a controlled calcined cathode thickness of 20 μm. The cathode layer might crack and delaminate if its thickness was above 50 μm since the other components have already been sintered.

4.2.2. Characterization

Catalytic characterization of the anode materials was performed in a packed bed reactor. The reactor consisted of a 1/4"-OD quartz tube suspended in an 18"-long single-zone furnace. The temperature was controlled using a quartz-sheathed K-type thermocouple located just below the catalyst bed. The catalyst was held in place between two quartz wool plugs. The feed streams were introduced using MKS mass flow controllers, and the product stream was analyzed with an Agilent 6890 gas chromatograph. The studies were conducted under a fuel-rich condition (methane-to-oxygen molar ratio = 2), whereby full selectivity to combustion products would correspond to a maximum methane conversion of 25%. Selectivity to synthesis gas could increase the methane conversion to 100%.

The anode materials were characterized by X-ray diffraction (XRD) (Siemens D5000). Crystalline plane spacings were calculated by Bragg's law, using an internal silver standard for peak reference. Porosity was measured using the Archimedes principle. SOFC microstructure was examined by scanning electron microscopy (SEM) (JEOL 5910). Dynamic light scattering (DLS) was used to analyze the particle size of the precipitates. The ceramic composites were also characterized by 4-point conductivity tests (Keithley 236) in an atmosphere controlled by MKS mass flow controllers.

The SOFC systems were sealed using a glass composite, a 50:50 mixture (by weight) of Ferro F1040 glass and 8-μm YSZ (MEI). The powder mixture was made into a slurry using water glass, and applied around the edges of the cell to bind them to the alumina tube. The sealing was performed for 2 h at 900°C, above the melting point of the glass. The cell was then cooled to the operating temperature of 800°C for testing. This sealant has numerous advantages over the commonly used Aremco cements. The thermal expansion of the alumina tube was problematic when a μm-thick YSZ membrane was bonded directly to the alumina. Commercially available cements would result in cell damage and a low testing yield of ~ 20%.

Cell testing was initiated with a humidified 5% hydrogen stream at the operating temperature for 4 h. The feed was then changed to humidified 97% hydrogen for 30 min. Next, 0.5" plungers covered with gold or platinum mesh were lowered to the contact pads on the fuel cell. The contact pads on the cathode and anode were made from Pt paste (Engelhard A3788A) and Au paste (Engelhard T10112), respectively. The fuel and air flow rates were 150 ml/min

and 550 ml/min [10], respectively. Electrochemical performance of the fuel cells was characterized using a Solartron 1287 pontentiostat.

4.2.3. Experimental Design

For the Ni-Sn/YSZ system, the following synthesis parameters were investigated: the mol% Sn in the alloy, the vol% alloy in the cermet, and the weight fraction of Unitec-10 coarse-grained YSZ vs. Tosoh fine-grained YSZ (see Table 4.3). The Sn content was limited to 40 mol%, above which the Ni-Sn alloy might form a liquid at the operating temperatures. The various samples were examined for shrinkage, porosity, % densification, grain coarsening, conductivity, oxidation resistance, and coke tolerance. The anode materials that demonstrated sufficient stability in reaction with dry methane were subjected to electrochemical testing.

Table 4.3. Range of parameters investigated in developing the Ni-Sn/YSZ cermet.

	Mol% Sn	Vol% Alloy	Wt% Coarse YSZ
Parameter Space	0–40	40–70	0–100
Optimal Parameter	40	35–45	0–100

4.3. Results and Discussion

4.3.1. Development of Ceria/$LaCrO_3$ Anode

4.3.1.1. Catalytic Conversion of Methane over Doped Ceria

For direct hydrocarbon fuel cells that did not rely on internal reforming, the current density obtained was significantly lower using a hydrocarbon feed vs. a hydrogen feed. For example, the current density of the Cu/ceria cermet at 0.7 V decreased by a factor of 4 when operating on methane [57]. Clearly, the electrochemical fuel conversion was a limiting process for direct hydrocarbon systems. For the all-ceramic anode systems, it would be important that ceria provides sufficient catalytic activity for methane conversion so that the power production would not be limited. To improve catalytic activity, ceria was first doped with 20 at% Y, Zr, Sc and Ca since the resulting doped ceria materials were known to be stable solid solutions up to 1200°C [58]. The doped ceria materials (0.02 g) were examined for the oxidation of 3% CH_4 in 1.5% O_2 at 65,000 h^{-1}. Methane was combusted over all the doped ceria catalysts; only a small

amount of hydrogen was generated at the higher temperatures. Figure 4.3 shows that none of the non-lanthanide dopants studied enhanced ceria's activity towards methane conversion.

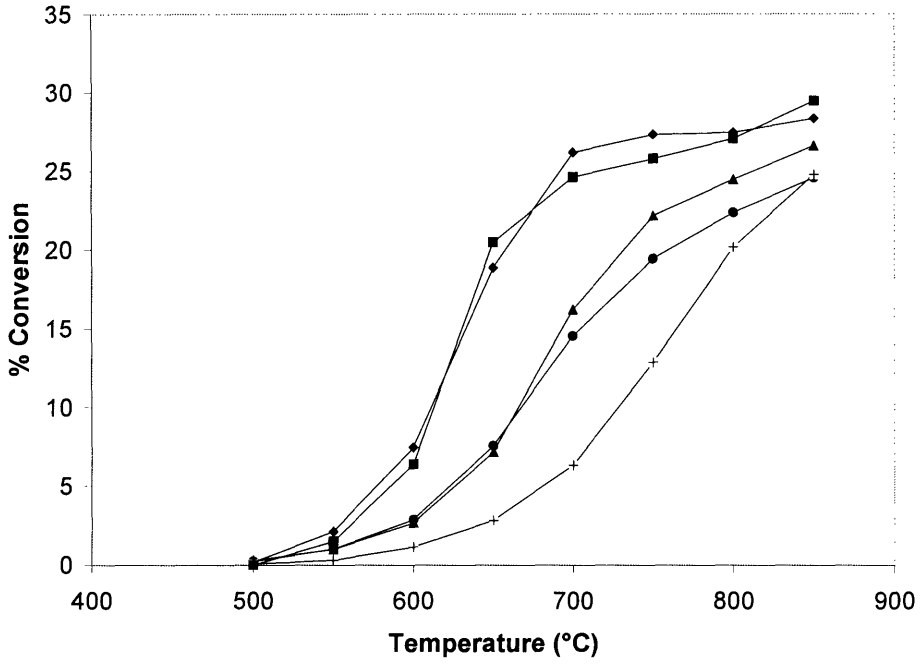

Figure 4.3. Methane conversion over (■) undoped ceria, and ceria doped with 20 at% (♦) Y, (▲) Zr, (●) Sc and (+) Ca at 65,000 hr^{-1} with a CH_4/O_2 molar ratio of 2.

Ceria was then doped with lanthanides such as Pr and Tb, since praseodymia and terbia have the same crystal structure as ceria and form a single-phase fluorite structure with ceria. Sm was also examined as it has been the most common dopant for increasing ceria's ionic conductivity. Figure 4.4 shows that ceria's activity and stability were increased with Pr, Tb and Sm doping. These materials all catalyzed the combustion reaction, producing only a small amount of hydrogen at elevated temperatures. The low-temperature activity was correlated to the reducibility of the doped ceria. The lanthanide dopants lowered the temperature required for oxygen extraction from ceria, leading to improved methane oxidation.

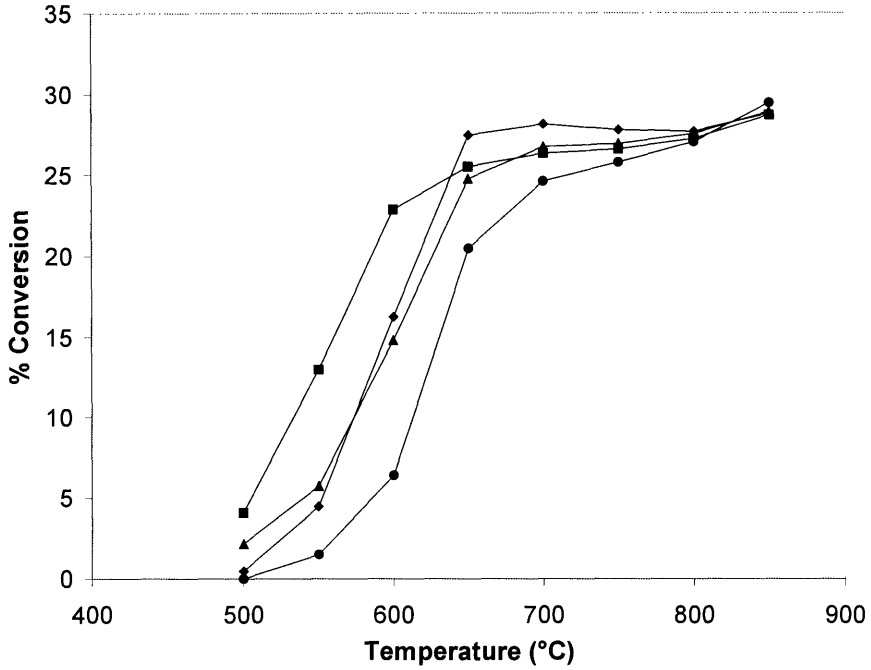

Figure 4.4. Methane conversion over (●) undoped ceria, and ceria doped with 20 at% (■) Pr, (♦) Sm and (▲) Tb at 65,000 hr^{-1} with a CH_4/O_2 molar ratio of 2.

Differential rates were obtained for the doped ceria materials at 750°C by diluting the catalysts with alumina to obtain an effective space velocity of 1,500,000 h^{-1}. The rates were reproduced by varying the catalyst loading and adjusting the reactant flow rate while maintaining the same space velocity. This indicated that the homogeneous reactions were limited. The surface area normalized rates in Table 4.4 illustrated the effectiveness of lanthanide doping on ceria. To understand how these rates might affect the maximum power density obtained from the resulting SOFC system, the reaction rates were converted into current densities. The calculation was based on the oxygen flow required to maintain the methane reaction rate over a ceria laminate with the same surface area as the electrolyte. Three-dimensionally active electrodes would increase the active area available for reaction beyond this assumption. The calculated current densities were slightly higher than those experimentally obtained with methane over the Cu/ceria-based anodes. However, they were well below those obtained over the best hydrogen-fed SOFC systems. Besides doping, it might be important to include metal catalysts to achieve high power densities in the all-ceramic anodes.

Table 4.4. Rate of methane conversion at 750°C and a CH_4/O_2 molar ratio of 2.

Catalyst	Reaction Rate (mol/s/g)	Reaction Rate ($mol/s/m^2$)	Equivalent Current Density (A/cm^2)
Ceria	0.30	0.0086	0.66
Praseodymia	0.46	0.022	1.7
20 at% Tb-CeO_2	0.51	0.014	1.1
20 at% Sm-CeO_2	0.57	0.015	1.2
20 at% Pr-CeO_2	0.72	0.014	1.1

To measure the conductivity of doped ceria, dense sample bars were compacted by cold isostatic pressing at 50,000 psi and sintered at 1400°C. Doped praseodymia samples were also included due to the high reaction rate of pure praseodymia (see Table 4.4). However, the Pr-containing pellets all underwent severe cracking upon cooling (see Table 4.5). Firing in nitrogen helped alleviate the cracking problem, but the pellets degraded to a powder upon storage at room temperature. Only pure, Tb-doped and Sm-doped ceria pellets were successfully densified.

Table 4.5. Effect of processing atmosphere on the mechanical stability of pure and doped ceria and praseodymia.

	Ceria				Praseodymia			
Dopant	–	20% Sm	20% Tb	20% Pr	–	20% Sm	20% Tb	20% Ce
O_2-Fired	Dense	Dense	Dense	Cracked	Cracked	Cracked	Cracked	Cracked
N_2-Fired	Dense	Dense	Dense	Cracked	Dense	Dense	Dense	Cracked
% Porosity	1.4	1.6	1.1	N/A	N/A	N/A	N/A	N/A

XRD was used to investigate the phase changes in praseodymia during thermal treatment. Figure 4.5 shows that praseodymia could be prepared in a pure PrO_2 phase and a mixed PrO_2/Pr_6O_{11} phase by firing at 800°C in pure oxygen and air, respectively. Sintering at 1400°C in air resulted in a pure Pr_6O_{11} phase, with a lattice volume increase of 4%. This lattice expansion might have caused the cracking of Pr-containing pellets.

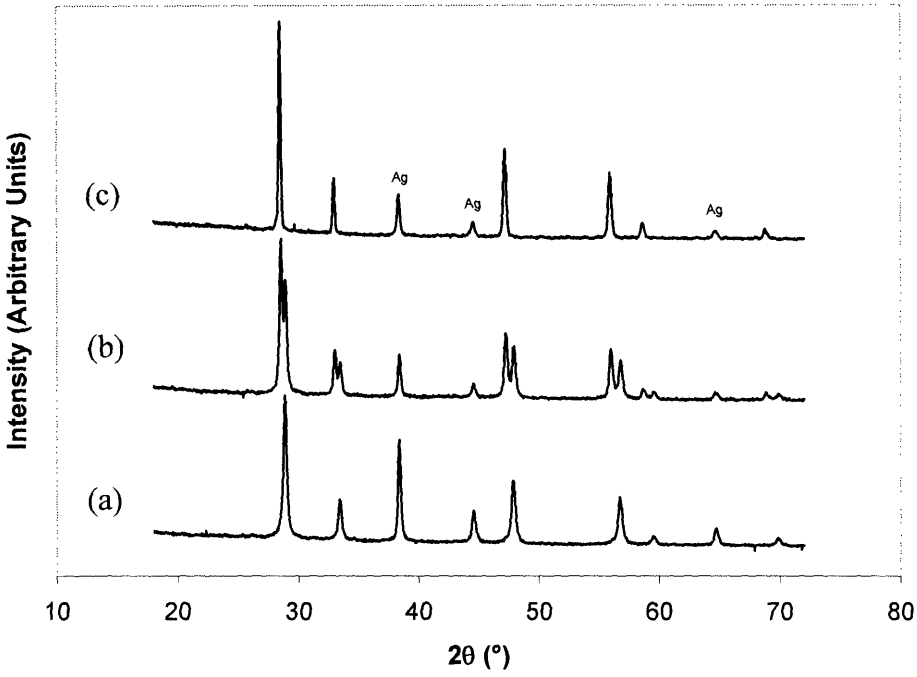

Figure 4.5. XRD patterns of praseodymia (a) as-prepared (pure PrO_2 phase), (b) after firing at 800°C in air (mixed PrO_2 and Pr_6O_{11} phases), and (c) after sintering at 1400°C in air (pure Pr_6O_{11} phase). A silver internal standard was used.

4.3.1.2. Co-Precipitation of $CeO_2/LaCrO_3$ Nanocomposites

Conductivity measurements confirmed that the doped ceria materials were not conductive enough to serve as an anode support. Therefore, lanthanum chromate was mixed with ceria to provide the electrical conduit in the resulting ceramic composite anode. To achieve a highly dispersed composite, chemical co-precipitation was employed instead of physical mixing of different oxide powders. Figure 4.6 shows that ceria and lanthanum chromate phases were successfully achieved by co-precipitation for the various $CeO_2/LaCrO_3$ composites. The grain size of the ceria and lanthanum chromate phases were analyzed after calcination at 800°C in air and in hydrogen (see Figure 4.7). Finer CeO_2 and $LaCrO_3$ grains were obtained in the nanocomposites than in the respective pure oxides, indicating the successful suppression of grain growth in the presence of a secondary phase. The $CeO_2/LaCrO_3$ nanocomposites also demonstrated increased ceria stability towards reduction. For pure ceria, the grain size nearly tripled when exposed to dry 7% hydrogen at 800°C for 3 h. In the $CeO_2/LaCrO_3$ nanocomposite with 60 vol% $LaCrO_3$, ceria's grain growth was limited to ~ 35%.

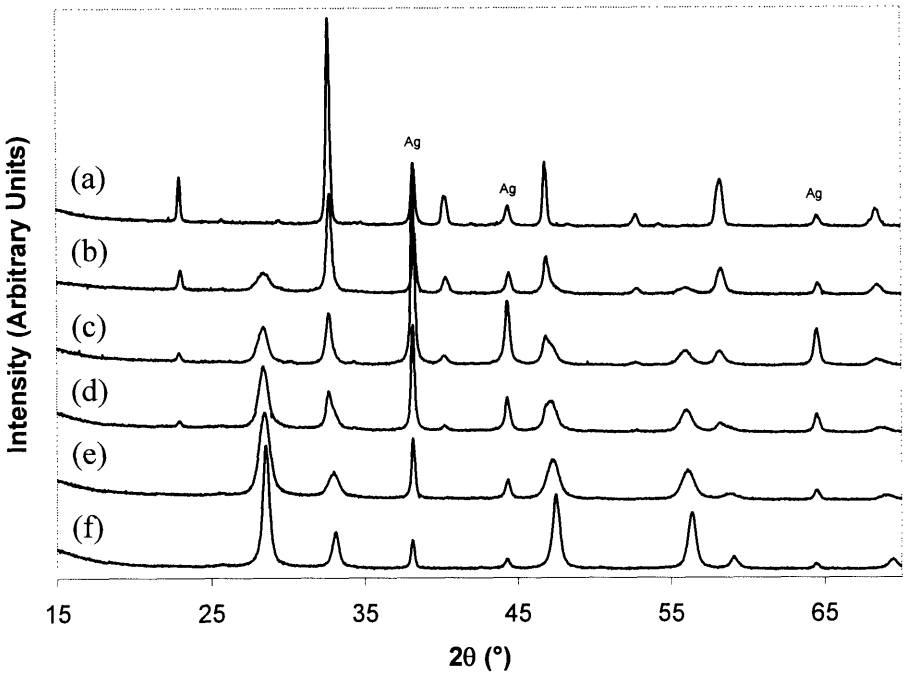

Figure 4.6. XRD patterns of 800°C-calcined $CeO_2/LaCrO_3$ composites with (a) 100, (b) 80, (c) 60, (d) 40, (e) 20 and (f) 0 vol% $LaCrO_3$. A silver internal standard was used.

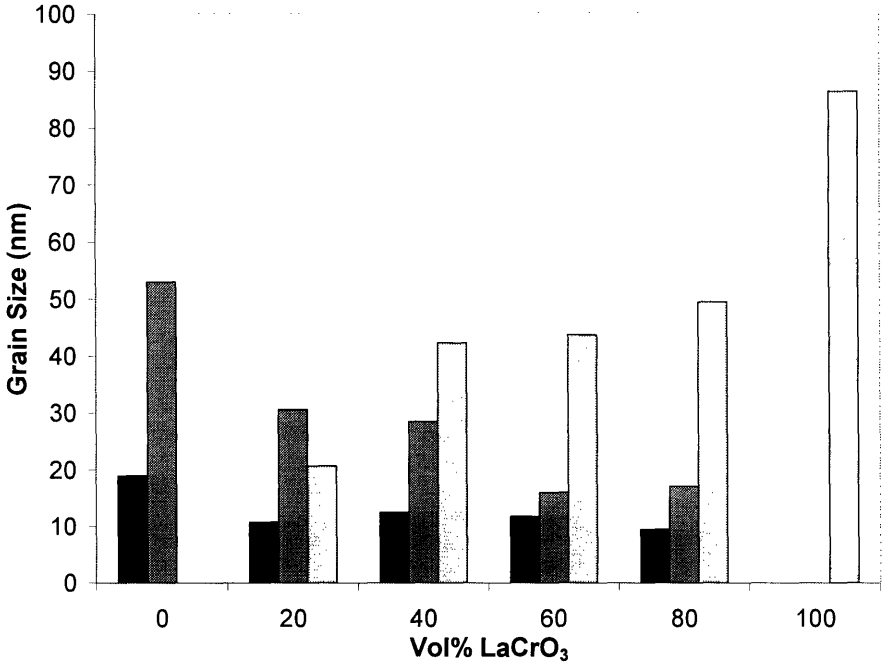

Figure 4.7. Grains sizes of CeO_2 (black) in $CeO_2/LaCrO_3$ nanocomposites calcined at 800°C in air, and CeO_2 (dark grey) and $LaCrO_3$ (light grey) in $CeO_2/LaCrO_3$ nanocomposites reduced at 800°C in hydrogen.

Silver was added as an internal standard to allow for peak shift analysis of ceria (111) (2θ ~ 28°) in the XRD patterns of $CeO_2/LaCrO_3$ composites. La^{+3} doping would expand ceria's fluorite lattice since it has a larger ionic radii (1.18 Å) than Ce^{+4} (0.97 Å). Figure 4.8 shows that ceria's lattice parameter increased linearly with $LaCrO_3$ loading in the 1400°C-sintered $CeO_2/LaCrO_3$ composites. This indicated an increased La doping in ceria with increasing $LaCrO_3$ loading in the composite, which would in turn correspond to an A-site deficiency in the $LaCrO_3$ perovskite. La-doped ceria might provide for increased catalytic activity for methane conversion. However, large excess in La might lead to lanthanum zirconate formation at the interface with YSZ electrolyte. Therefore, it would be desirable to have a synthetic technique that allowed for the incorporation of less reactive dopants such as Sm.

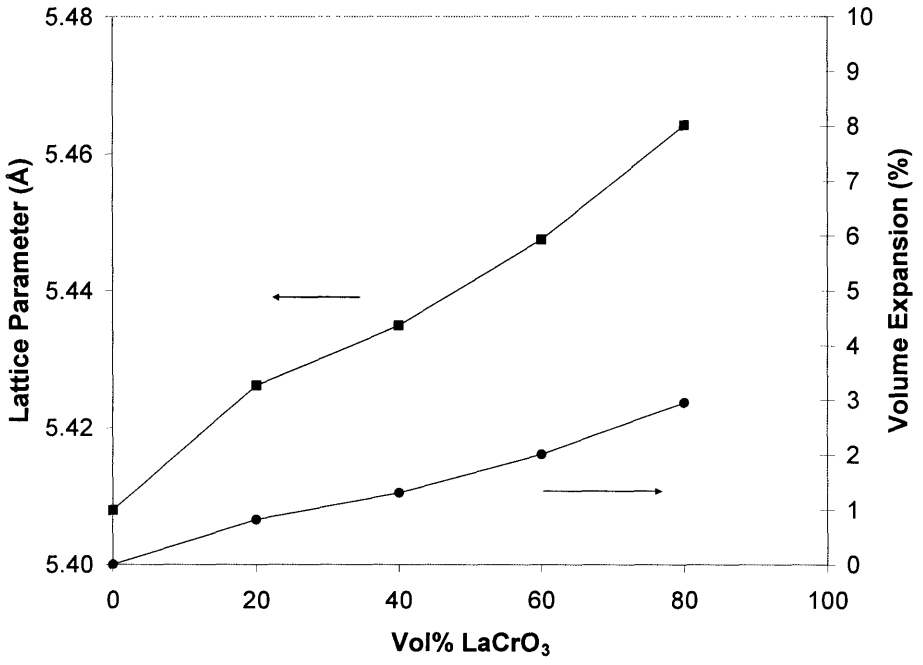

Figure 4.8. (■) Cubic lattice parameter and (●) volume expansion in ceria for the 1400°C-sintered $CeO_2/LaCrO_3$ composites.

4.3.1.3. Synthesis of Doped Ceria Dispersions

As the alternative lanthanide dopants for ceria could also be doped into the perovskite structure, it would be important that doped ceria and lanthanum chromate be prepared separately. This could be achieved by synthesizing two separate hydroxide slurries, and combining them right before the drying and agglomeration steps. Mixing the materials in the form of well-

dispersed hydroxide slurries would provide a more intimate mixture than the physical mixing of calcined oxide powders.

Ce(IV) oxide sols have been prepared by the peptization of hydroxide precipitates in hot nitric acid [59,60]. However, lanthanide(III) dopants such as Sm would leach out from the sol during peptization [61]. Furthermore, addition of an acidic sol to the basic hydroxide precursor of lanthanum chromate would result in dissolution.

The approach developed in Chapter 2 [62] is readily applied to basic hydroxides. In this case, the isoelectric point of the precursor would be crossed by rinsing in methanol even though the precipitation was performed in excess base. To prepare Sm-doped cerium hydroxide, an aqueous solution of Ce(III) and Sm(III) nitrates (0.8 M) was added to a 0.4 M solution of TEAH in isopropanol. The base excess used was 1.5 based on the Ce(III) ion. Upon rinsing in methanol, a suspension of 100-nm particles was obtained.

The powders obtained by this synthesis were quite different from the conventional powders. To illustrate the effect of dispersion on textural properties, a large quantity of Sm-doped cerium hydroxide was prepared and subjected to four different treatments. In all four cases, the precipitate was initially collected by centrifugation. It was then rinsed three times in methanol (M) or isopropanol (I) using a homogenizer. Unlike the isopropanol rinses, methanol rinses resulted in a suspension that became difficult to centrifuge. After rinsing, the powders were collected by room-temperature drying of the centrifuge cake (C) or the homogenized slurry (H). The properties of the IC and IH samples were essentially identical since a stable dispersion was not produced from isopropanol rinses. MC and MH samples have slightly different properties; they were very different from the IC and IH samples (see Figure 4.9). The dispersed hydroxides (obtained from methanol rinses) produced powders (MC and MH) that could be more tightly packed than the flocculated systems (obtained from isopropanol rinses). The dispersed hydroxide that was dried slowly in the form of a homogenized slurry (MH) gave rise to the smallest pore radius. The differences in the pore size distributions of these doped ceria particles led to large differences in the microscopic and macroscopic properties.

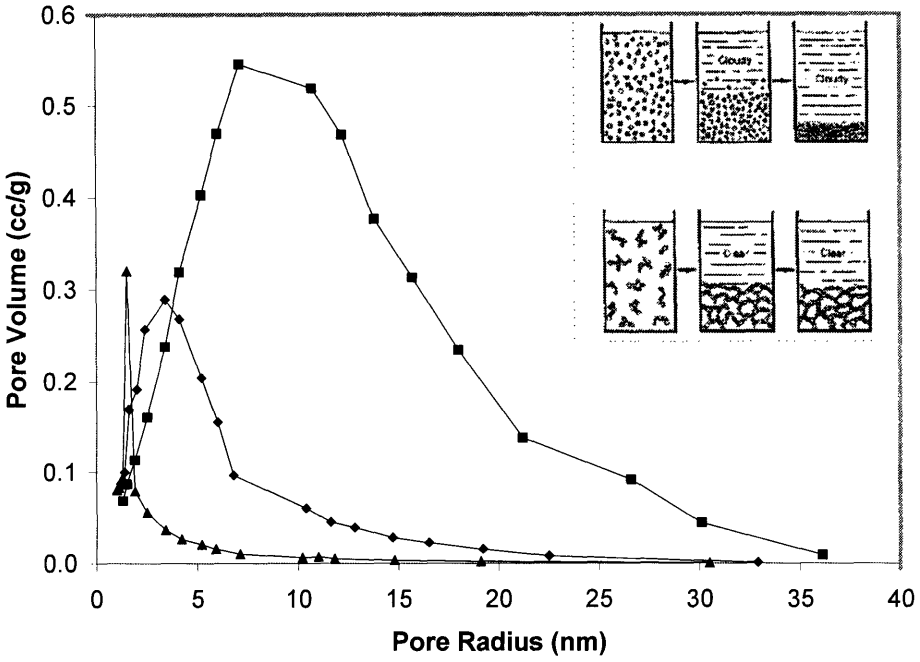

Figure 4.9. Pore size distributions of 400°C-calcined Sm-doped ceria particles subjected to (■) IC, (♦) MC and (▲) MH treatments. Inset: Illustration of oxide sedimentation from a dispersed state (top) and a flocculated state (bottom) [63].

The flocculated sample (IC) at 400°C has a high surface area of 143 m^2/g and a high pore volume of 0.411 cc/g. The well-dispersed sample (MH) also has a high surface area (94 m^2/g), but a low pore volume (0.08 cc/g). The MC sample has an intermediate surface area of 123 m^2/g and an intermediate pore volume of 0.19 cc/g. The pore volume also affected the tapping density of the collected powders (see Figure 4.10). The MH particles have a tapping density of 33% at 400°C, whereas the ceramic-grade Sm-doped ceria (NexTech) only has a tapping density of 15% and a surface area of 14 m^2/g. At 800°C, the MH sample lost almost all of its surface area since its small pores could be easily removed during sintering. Overall, the well-dispersed Sm-doped ceria system (MH) has similar textural properties as pure ceria derived by conventional sol processing [61]. Our new approach would be very useful since it could be easily applied to the synthesis of multicomponent oxides, without the limitations of conventional sol processing.

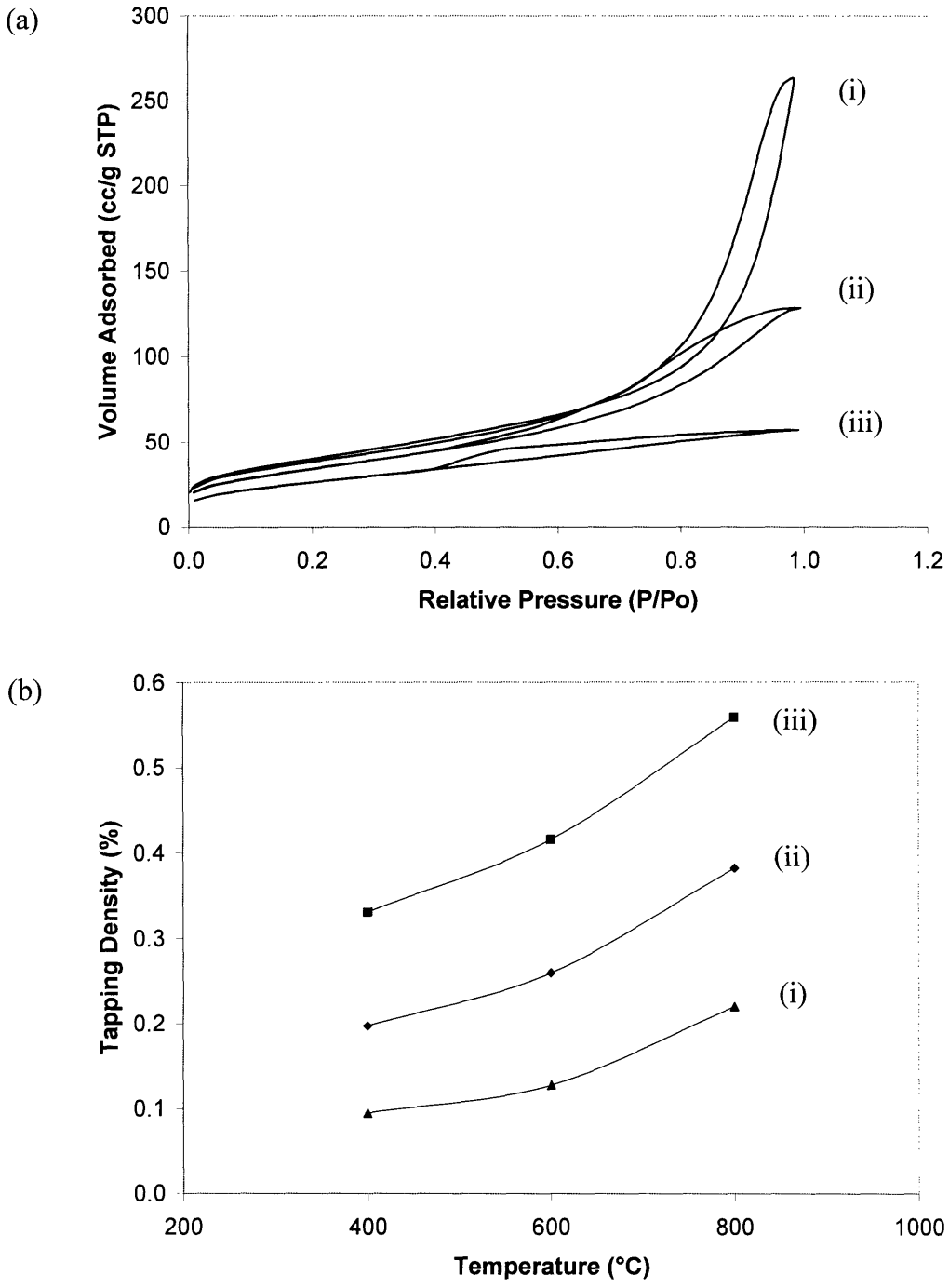

Figure 4.10. (a) Nitrogen adsorption-desorption isotherms and (b) tapping densities of 400°C-calcined Sm-doped ceria particles subjected to (i) IC, (ii) MC and (iii) MH treatments.

4.3.1.4. Application of $CeO_2/LaCrO_3$ Composite to Anode-Supported SOFC

The synthetic methods described in Sections 4.3.1.2 and 4.3.1.3 were successfully applied towards the derivation of $CeO_2/LaCrO_3$ nanocomposites. However, the mixture of Ce(IV) oxide and Cr(III) oxide led to substantial formation of Cr(VI). In solution, Ce^{+4}/Ce^{+3} has a higher standard electrode potential than Cr^{+6}/Cr^{+3} (1.78 V vs. 1.36 V) [64]. Ce(IV) was a stronger oxidizer, and Cr(III) oxidation was pervasive even when a physical mixture of CeO_2 and $LaCrO_3$ powders was used. Due to the toxicity of Cr(VI), La-doped $CaTiO_3$ was used in further studies instead of $LaCrO_3$.

4.3.2. Development of Sm-CeO_2/La-$CaTiO_3$ Anode

Single-phase La-doped $CaTiO_3$ was developed as the anode support. A thin electrochemically active composite anode interlayer was then applied to introduce the doped ceria phase as required for good performance. This separated the variables involved in the cell fabrication from those that affected the electrochemical performance.

By carefully controlling the processing of commercially derived La-doped $CaTiO_3$, a sintering curve was obtained (Figure 4.11). To complete the SOFC fabrication, an interlayer was applied and calcined to the same temperature as the anode support. The precalcination temperature was determined by the sintering curve of the YSZ applied on the anode interlayer. The shrinkage required to obtain a dense YSZ layer was 16.8% for this system. This resulted in sufficiently flat button cells that could be tested. As the doped ceria and doped $CaTiO_3$ mixture sintered quite readily along with the YSZ electrolyte, porosity was introduced to the anode support using 20–50 μm glassy carbon.

To introduce porosity into the anode interlayer, carbon black with a large particle size (75 nm) was employed. The resulting pore size was small enough to be partially sintered, so extra shrinkage was introduced in these green bodies. The sintering curve of the oxide host would remain unchanged only when the pore size generated by porogen was large enough not to be affected by the sintering process [65]. The 20 wt% carbon black addition resulted in a fine porosity with acceptable X-Y shrinkage for the desired thin films. However, cracking was noted when it was applied to films of > 50 μm-thick. Figure 4.12 shows the microstructure of the La-$CaTiO_3$-supported fuel cell, with a Sm-CeO_2/La-$CaTiO_3$ composite anode interlayer that contained 35 vol% Sm-CeO_2.

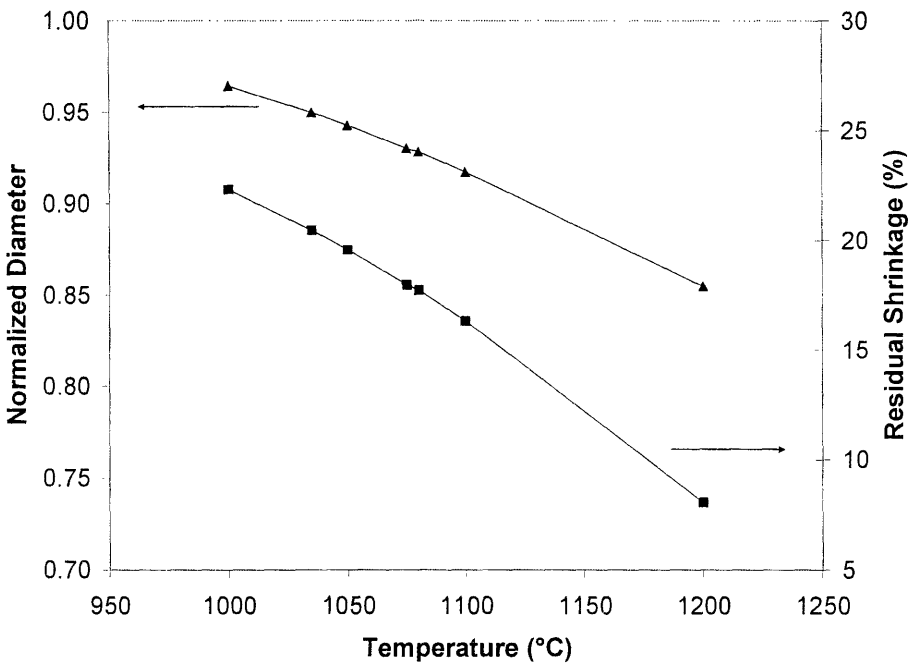

Figure 4.11. (▲) Normalized diameter and (■) % residual shrinkage of calcium titanate anode support as a function of processing temperature.

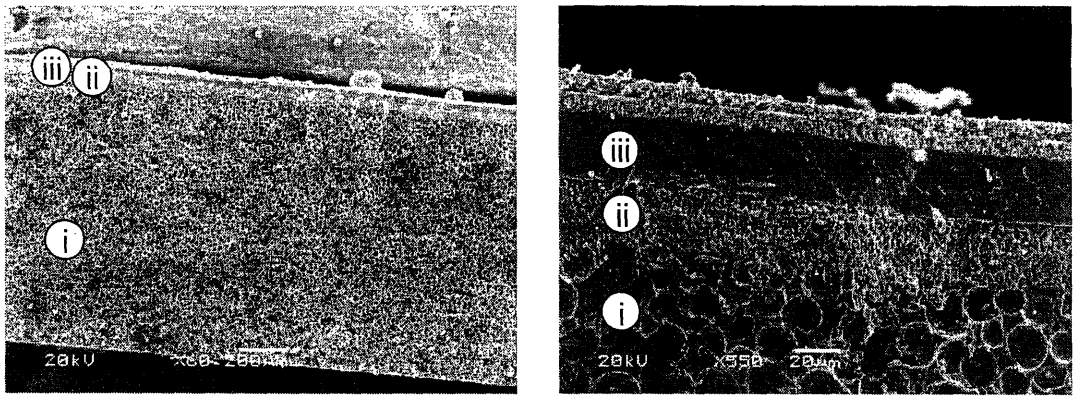

Figure 4.12. Cross-sections of an anode-supported SOFC: (i) La-$CaTiO_3$ anode, (ii) Sm-CeO_2/La-$CaTiO_3$ composite anode interlayer, and (iii) YSZ electrolyte.

For cell testing, low levels of transition metal catalysts (e.g. copper, nickel and cobalt) were added to the electrochemical layer by impregnating the ceria powder with the respective nitrate precursor dissolved in methanol. While nickel could be added in high quantities, only low loadings of cobalt and copper could be used without cell damage due to their volatility and melting, respectively, at the YSZ sintering temperature.

The electrochemical performance of these cells was investigated at 900°C in humidified hydrogen (see Figure 4.13). The interlayer with nickel demonstrated the highest open-circuit potential. The interlayers containing copper and cobalt showed very low open-circuit potentials; the higher metal contents led to lower open-circuit potentials. The vaporization of cobalt or melting of copper oxides in the YSZ electrolyte during densification might have introduced some electronic conductivity. Overall, the power densities illustrated in Figure 4.13 were quite low; the values obtained were essentially the same as that achieved over La-$SrTiO_3$ without ceria addition in an electrolyte-supported design [33]. The major limitation of this anode material was the low conductivity of the La-$CaTiO_3$ support. Although the conductivity for air-sintered La-$CaTiO_3$ was reported at 12 S/cm after reduction at 900°C [49], our samples exhibited only a conductivity of 0.086 S/cm. Since the latter was less than the ionic conductivity of YSZ (0.1 S/cm) at 900°C, and the support:electrolyte thickness ratio was 1000:2, it was critical to address the low conductivity of La-$CaTiO_3$. Elemental and phase analyses verified that the commercially derived La-$CaTiO_3$ was prepared correctly. Various dopant and processing schemes were then explored, but did not yield much success. Thermal gravimetric analysis (TGA) indicated that bulk reduction of the titanate occurred above 1000°C. The observed conductivity was likely due to surface reduction of the large calcium titanate grains (2–3 μm) that resulted during air sintering.

To maximize the conductivity of the air-sintered calcium titanate in reducing atmospheres, grain growth has to be suppressed [50] to yield higher surface-to-volume ratios. Finer-grained titanate could be achieved by simply decreasing the anode firing temperature. However, anode-supported systems required a firing temperature of 1400°C. Therefore, this anode formulation would likely find good performance only when applied in a cathode-supported or electrolyte-supported design. To minimize grain growth, the anode firing temperature should be suppressed as much as possible. Although bulk ceria-based anodes would typically adhere to sintered YSZ at 1200°C [15], nanocrystalline ceria could be fully densified by 900°C [66]. A nanocomposite strategy similar to that demonstrated for the $CeO_2/LaCrO_3$ system would minimize grain growth at a given temperature, and might even promote low-temperature adhesion. The co-precipitation technique might provide the required microstructures for the successful application of this material system to a cathode-supported or electrolyte-supported cell.

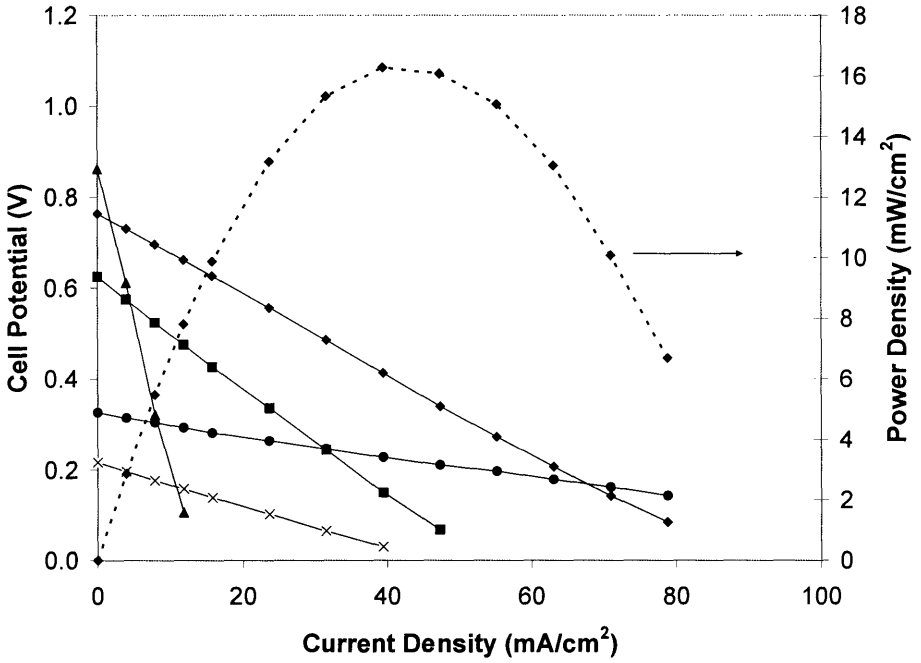

Figure 4.13. Cell potential (solid lines) and power density (dashed line) as a function of current density at 900°C for Sm-CeO_2/La-$CaTiO_3$ composite anode interlayer containing (▲) 2.5 wt% Ni, (●) 2.5 wt% Co, (×) 2.5 wt% Cu, and (♦, ■) 0.5 wt% Cu. The studies were conducted in humidified hydrogen (▲, ●, ×, ♦) or humidified methane (■).

4.3.3. Development of Ni-Sn/YSZ Cermet Anode

To overcome the low conductivity of the ceramic anode supports developed thus far, a cermet system was examined. The goal was to produce a thick anode structure that exhibited no volume changes upon exposure to dry methane at 800°C for 1.5 h [67]. The strategy was to prevent coke formation by using an alloy. After an initial study of the parameter space (see Table 4.3), it was determined that the best anode structures for this application would have ~ 40 mol% Sn in the Ni-Sn alloy, and ~ 40 vol% alloy in the Ni-Sn/YSZ cermet.

Figure 4.14(a) shows that the desired Ni-Sn alloy was successfully obtained by reducing a nickel-tin-zirconium oxide composite, even though the latter has been subjected to significant grain growth and sintering at 1400°C. Only the XRD peaks for the alloy was detected; no separate Ni or Sn diffraction peaks were noted. Unlike the Ni/YSZ cermet (Figure 4.14(c), no graphitic crystalline carbon peak was observed at $2\theta = 26°$ when the Ni-Sn/YSZ cermet was exposed to dry methane at 800°C for 1.5 h (Figure 4.14(b)).

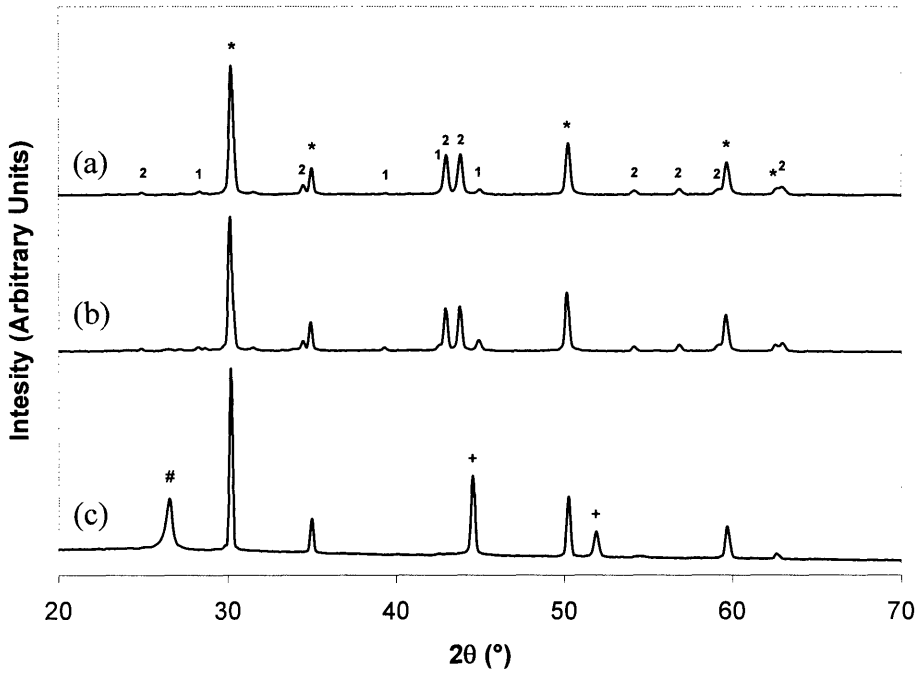

Figure 4.14. XRD patterns for (a) Ni-Sn/YSZ cermet prepared by reduction of the oxide composite, and (b) Ni-Sn/YSZ cermet and (c) Ni/YSZ cermet after exposure to dry methane at 800°C. Ni_3Sn_1 (1), Ni_3Sn_2 (2), Ni (+), YSZ (*), and carbon (#) peaks are denoted.

The dimensional stabilities of Ni-Sn/YSZ (with 40 mol% Sn) and Ni/YSZ anodes were compared at various metal loadings (Figure 4.15). Increasing dimensional changes and weight gains were observed in the Ni/YSZ system with increasing metal loading. Although some coking took place over Ni-Sn/YSZ (as revealed by the weight gain), this system only experienced minor dimensional expansion above 40 vol% alloy loading. It appeared that the strength of the YSZ matrix was also an important variable in stabilizing the system against coking problems. Interestingly, the optimized direct hydrocarbon Cu/ceria cermet contained only 14.4 vol% metal. Metal loadings below 30 vol% led to poor percolation in the cermet and low conductivity [37]. The power output of the Cu/ceria system was tripled after intentional coking, which improved the metal connectivity in the cermet [68]. The stability of our Ni-Sn/YSZ cermet against structural damage in methane exposure at 800°C was remarkable (see Figure 4.16), especially considering its high metal loading of 40 vol%.

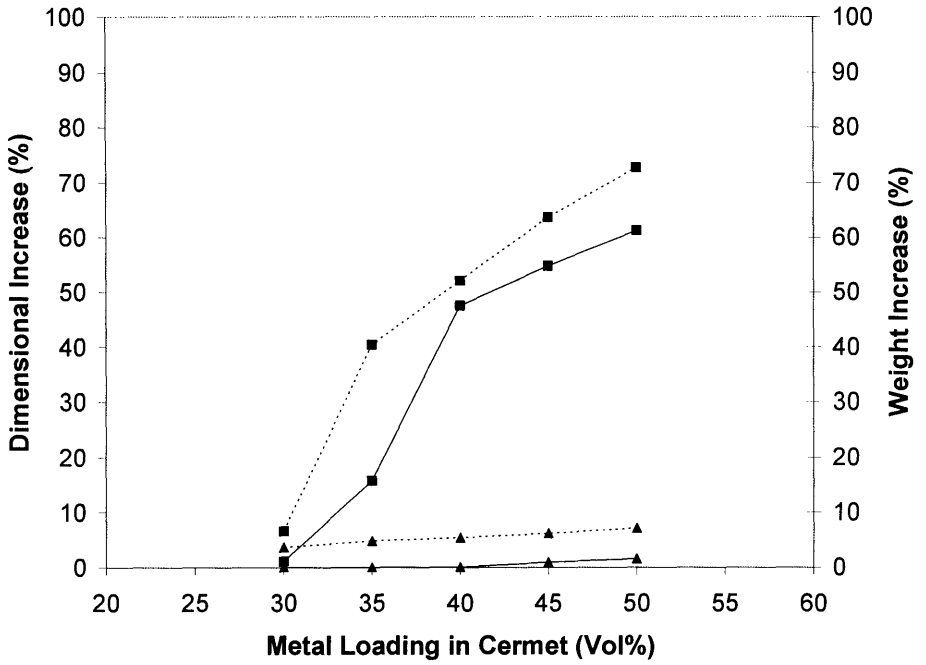

Figure 4.15. Dimensional increase (solid lines) and weight increase (dashed lines) in (■) Ni/YSZ and (▲) Ni-Sn/YSZ cermet anodes after exposure to dry methane at 800°C for 1.5 h.

Figure 4.16. Optical micrograph of Ni-Sn/YSZ anode-supported YSZ electrolyte (a) before and (b) after exposure to dry methane at 800°C for 1.5 h. Cells are 2 cm in diameter.

Figure 4.17 shows that the electrical conductivities of the Ni-Sn/YSZ cermets were very high compared to the ceramic systems initially explored (i.e. 400 S/cm at 40 vol% alloy). The effect of the YSZ particle size on initial conductivity was minor compared to the metal loading. However, the YSZ particle size has been shown to be important in the retardation of Ni sintering during the aging of Ni/YSZ. For a Ni/YSZ (40 vol% Ni) system with coarse-grained YSZ, the conductivity has been shown to be reduced from 1000 S/cm to 10 S/cm after 300 h at 1000°C [54]. Although highly conductive, Ni-Sn/YSZ was less conductive than the similarly fabricated Ni/YSZ (1060 S/cm at 40 vol% Ni). Since the Ni-Sn alloy was produced from a liquid precursor,

an agglomerated microstructure might have developed, similar to that found in an aged Ni/YSZ cermet.

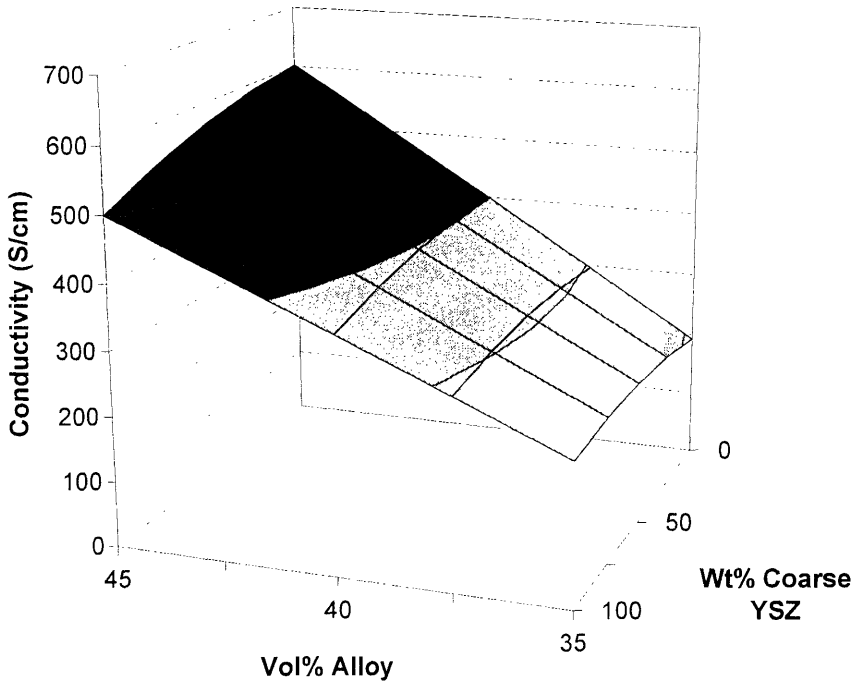

Figure 4.17. Electrical conductivity of the Ni-Sn/YSZ cermet (with 40 mol% Sn) as a function of alloy loading in the cermet and the fraction of coarse-grained YSZ particles used.

A SOFC was fabricated with the optimized Ni-Sn/YSZ anode system. The cross-section of the 1 mm-thick cell is shown in Figure 4.18. The electrochemical activity was examined for three different anode supports synthesized with 40 mol% Sn for the alloy and 40 vol% alloy loading in the cermet. The effect of YSZ particle size on the anode performance was investigated with 0, 50 and 100 wt% coarse-grained powders (Unitec-10). Figure 4.19 shows that a 50:50 mixture of coarse-grained and fine-grained YSZ particles led to the best cell potential and power density. The anode prepared with coarse-grained YSZ particles demonstrated essentially no power. As in the aged Ni/YSZ systems, the use of fine YSZ particles might be required to limit metal agglomeration [54]. The better performance of the anode with 50:50 mixture of coarse-grained and fine-grained YSZ compared to that with 100 wt% fine-grained YSZ could be due to a moderate enhancement in anode porosity observed through SEM.

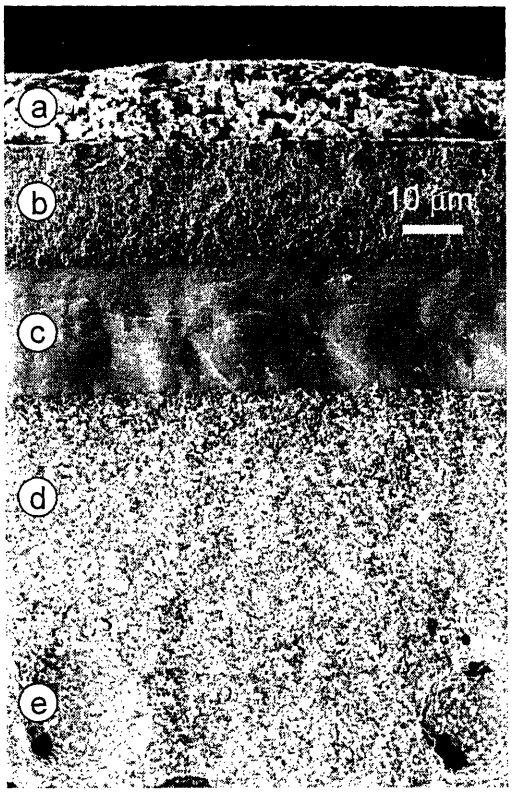

Figure 4.18. Cross-section of a reduced anode-supported SOFC with (a) Pt contact layer, (b) LSM/YSZ composite cathode, (c) YSZ electrolyte, (d) Ni-Sn/YSZ anode interlayer, and (e) Ni-Sn/YSZ anode support.

The performance of the optimized Ni-Sn/YSZ anode (produced with a mixture of 50:50 coarse-grained and fine-grained YSZ particles) was also sensitive to the reduction environment. When the system was reduced at too high a temperature or hydrogen concentration, a poor performance would result similar to that with 100% coarse-grained YSZ. Flooding of the cermet with liquid tin during alloy formation should be avoided. Optimal reduction involved the use of a humidified 5% hydrogen at the operating temperature (800°C). The highest power density achieved by the Ni-Sn/YSZ anode at 800°C in humidified hydrogen was 210 mW/cm^2 (Figure 4.20(a)), which was similar to that obtained with the optimized Cu/ceria cermet [69]. In comparison, a Ni/YSZ anode was able to produce a maximum power density of 520 mW/cm^2 (Figure 4.20(b)) using similar processing techniques.

The maximum power density achieved by the Ni-Sn/YSZ anode with humidified methane was 140 mW/cm^2 at 800°C (see Figure 4.21). This was several times higher than our best calcium titanate-based anode.

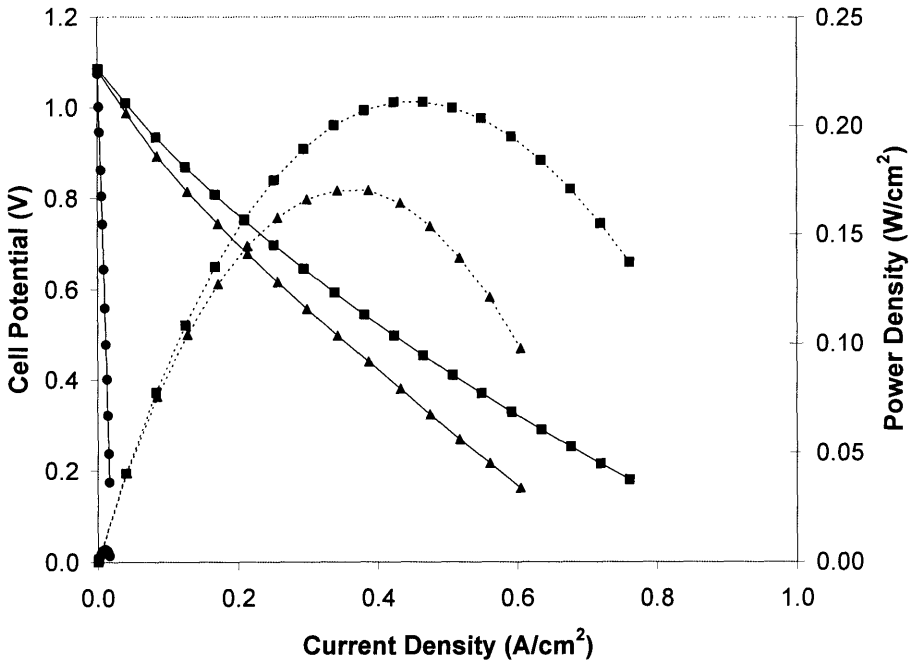

Figure 4.19. Cell potential (solid lines) and power density (dashed lines) for Ni-Sn/YSZ anodes synthesized using (●) 100 wt%, (■) 50 wt% and (▲) 0 wt% coarse-grained powders for YSZ. The studies were conducted in humidified hydrogen at 800°C.

Lastly, the ability of the Ni-Sn/YSZ anode to be reoxidized was examined. After complete reduction in 5% hydrogen at 900°C, the anode systems were reoxidized in air at 800°C. The increase in dimension associated with reoxidation was examined as a function of the alloy loading in the cermet and the fraction of coarse-grained YSZ particles used (Figure 4.22). The most significant improvement in cell stability resulted from the use of coarse YSZ particles. As expected, like other cermet anodes, the Ni-Sn/YSZ system could not be reoxidized once it has been reduced. Other strategies would need to be developed so that a cermet-based anode could be easily shutdown in a non-inert atmosphere.

On the overall, our novel anode system demonstrated great promise. It is one of the few non-Ni/YSZ electrode-supported cells fabricated entirely by conventional ceramic processing. It further exhibited exceptional dimensional stability and good power generation when operated on humidified methane at high temperatures.

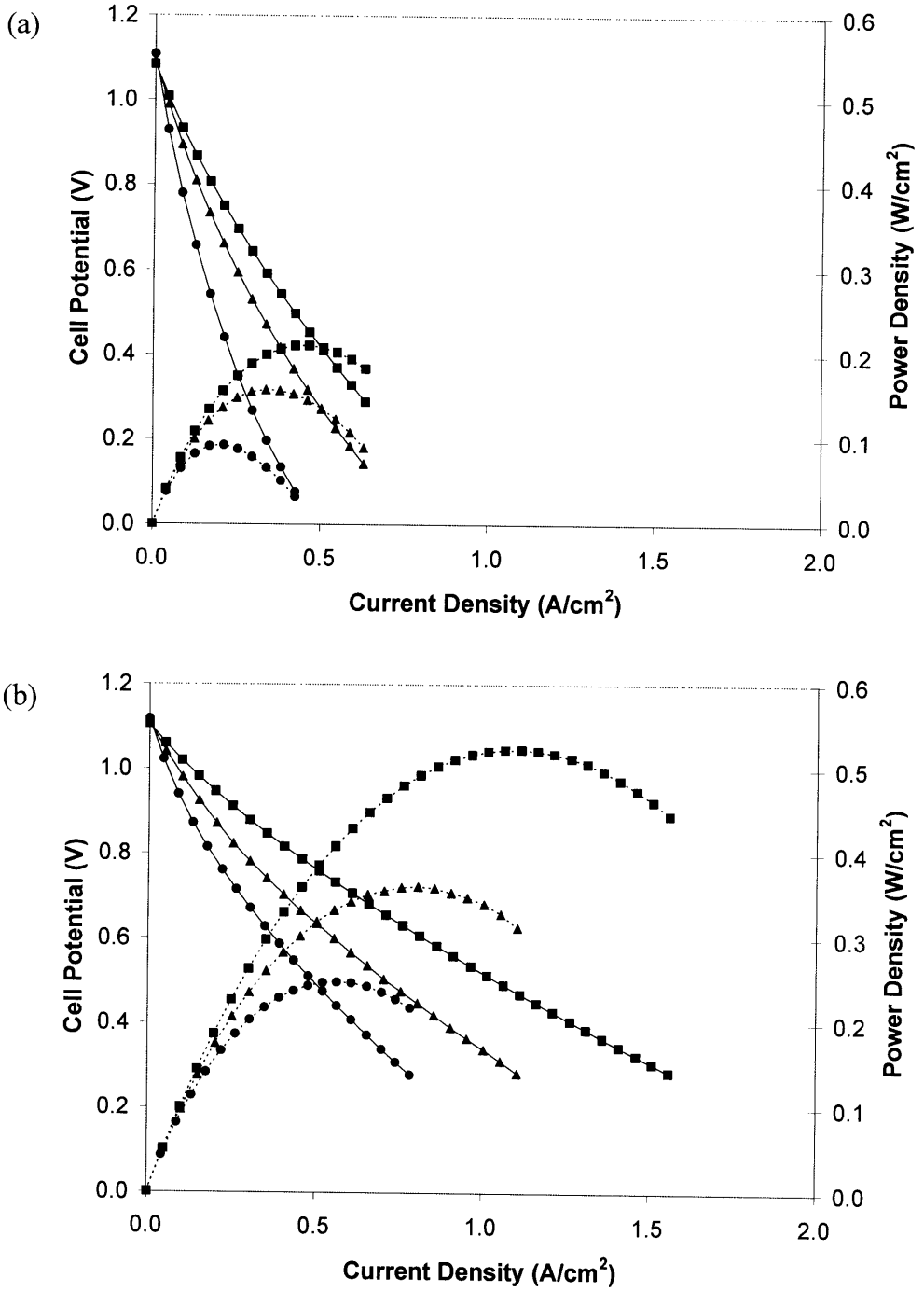

Figure 4.20. Cell potential (solid lines) and power density (dashed lines) for (a) Ni-Sn/YSZ and (b) Ni/YSZ anodes in humidified hydrogen at (●) 700°C, (▲) 750°C and (■) 800°C.

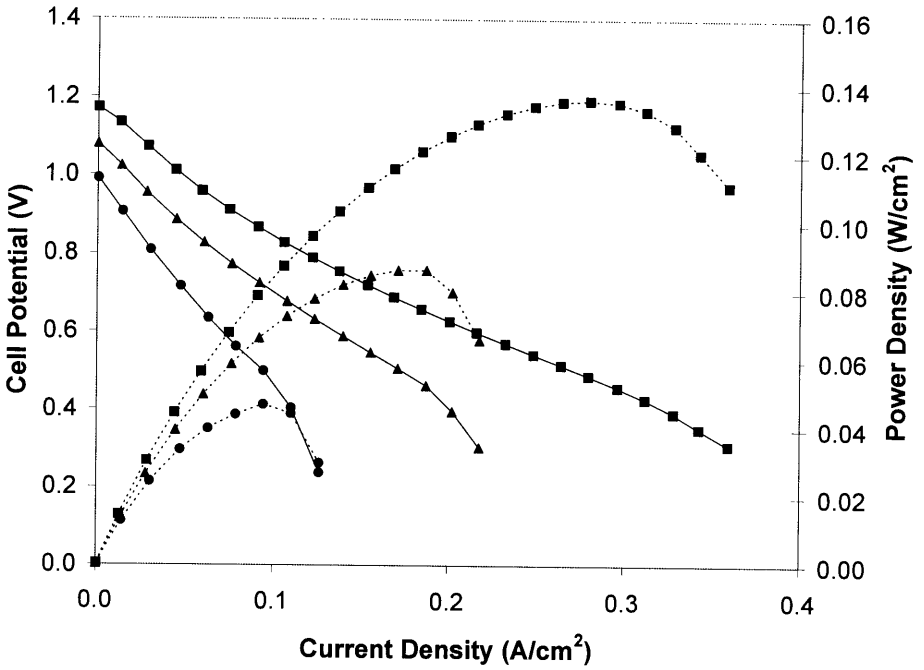

Figure 4.21. Cell potential (solid lines) and power density (dashed lines) for Ni-Sn/YSZ anode-supported cell in humidified methane at (●) 700°C, (▲) 750°C and (■) 800°C.

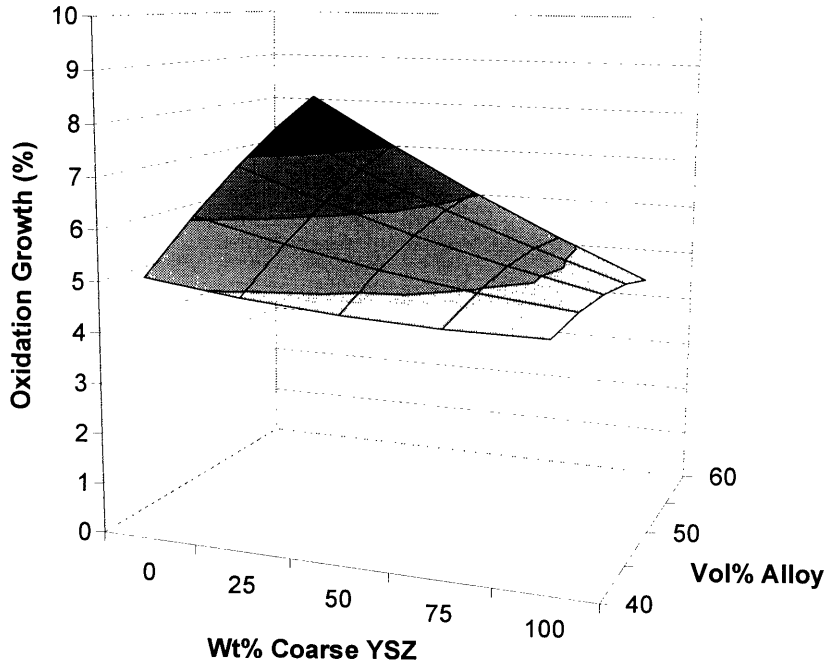

Figure 4.22. Oxidation growth of the Ni-Sn/YSZ cermet (with 40 mol% Sn) at 800°C as a function of the alloy loading in the cermet and the fraction of coarse-grained YSZ particles used.

4.4. Conclusions

To electrochemically oxidize dry fuels, existing anode systems have to meet challenges such as high electrical conductivity, ionic conductivity, catalytic activity, chemical and mechanical compatibility with the electrolyte, and low cost. Ceramic systems, metallic systems, as well as cermet systems have been examined by various researchers. Unfortunately, none of these materials have been found to meet all of the requirements. The most promising anode designs reported in the literature involved composite cermet systems.

Three anode systems have been explored in this work. The first two systems aimed at creating a composite ceramic anode support. Doped ceria was used to provide the electrochemical activity, while a chromate or titanate ceramic conductor was used as the current collector. A new synthesis was developed to co-precipitate separate ceria and chromate phases simultaneously. An alternative approach that allowed more control over the doping of ceria was also investigated. However, large quantities of Cr(VI) were produced from the synthesis of the ceramic support. Consequently, lanthanum chromate was replaced by La-doped calcium titanate for the composite anode system. The Sm-CeO_2/La-$CaTiO_3$ system provided very limited electrical conductivity when sintered at high temperatures in air. The resulting anode-supported cells showed low power densities.

Thirdly, a Ni-Sn/YSZ anode system was developed. This cermet could be easily fabricated into an anode-supported architecture using conventional ceramic processing techniques. The use of a Ni-Sn alloy in place of Ni prevented the formation of crystalline carbon, and provided for long-term dimensional stability in dry methane at 800°C. Power densities of 210 mW/cm^2 and 140 mW/cm^2 were achieved with humidified hydrogen and methane, respectively. However, like other cermets, Ni-Sn/YSZ anode could not be reoxidized once it has been formed. Thus, it would be limited to applications in controlled atmospheres.

4.5. References

[1] Ogden, J.M., *Annu. Rev. Energy Environ.* **24**, 227 (1999).
[2] Achenbach, E., *J. Power Sources* **49**, 333 (1994).
[3] Liu, J., Barnett, S.A., *Solid State Ionics* **158**, 11 (2003).
[4] Park, S., Vohs, J.M., Gorte, R.J., *Nature* **404**, 265 (2000).
[5] Gorte, R.J., Vohs, J.M., *J. Catal.* **216**, 477 (2003).
[6] Dahm, K.D., "Hydrocarbon Pyrolysis: Experiments and Graph Theoretic Modeling." Ph.D. Thesis, Massachusetts Institute of Technology, 1998.

[7] Steele, B.C.H., Heinzel, A., *Nature* **414**, 345 (2001).
[8] Will, J., Mitterdorfer, A., Kleinlogel, C.M., Perednis, D., Gauckler, L.J., *Solid State Ionics* **131**, 79 (2000).
[9] Souza, S., Visco, S.J., De Jonghe, L.C., *Solid State Ionics* **98**, 57 (1997).
[10] Jiang, Y., Virkar, A.V., *J. Electrochem. Soc.* **150**, A942 (2003).
[11] Eguchi, K., Setoguchi, T., Inoue, T., Arai, H., *Solid State Ionics* **52**, 165 (1992).
[12] Schneider, D., Godickemeier, M., Gauckler, L.J., *J. Electroceram.* **1**, 165 (1997).
[13] Tuller, H.L., Nowick, A.S., *J. Phys. Chem. Solids* **38**, 859 (1974).
[14] Marina, O.A., Mogensen, M., *Appl. Catal. A* **189**, 117 (1999).
[15] Marina, O.A., Bagger, C., Primdahl, S., Mogensen, M., *Solid State Ionics* **123**, 199 (1999).
[16] Yao, H.C., Yao, Y.F., *J. Catal.* **86**, 254 (1984).
[17] Kundakovic, L., Flytzani-Stephanopoulos, M., *Appl. Catal. A* **171**, 13 (1998).
[18] Descorme, C., Duprez, D., *Appl. Catal. A* **202**, 231 (2000).
[19] Perrichon, V., Laachir, A., Abouarnadasse, S., Touret, O., Blanchard, G., *Appl. Catal. A* **129**, 69 (1995).
[20] Vidal, H., Kaspar, J., Pijolat, M., Colon, G., Bernal, S., Cordon, A., Perrichon, V., Fally, F., *Appl. Catal. B* **27**, 49 (2000).
[21] Trovarelli, A., *Catal. Rev.* **38**, 439 (1996).
[22] Tschöpe, A., Liu, W., Flytzani-Stephanopoulos, M., Ying, J.Y., *J. Catal.* **157**, 42 (1995).
[23] Mogensen, M., Sammes, N.M., Tompsett, G.A., *Solid State Ionics* **129**, 63 (2000).
[24] Tejuca, L.G., Fierro, L.G., Tascon, M.D., *Adv. Catal.* **36**, 237 (1989).
[25] Weston, M., Metcalfe, I.S., *Solid State Ionics* **113**, 247 (1998).
[26] Tao, S., Irvine, J.T.S., *Nature Mater.* **2**, 320 (2003).
[27] Vernoux, P., Djurado, E., Guillodo, M., *J. Am. Ceram. Soc.* **84**, 2289 (2001).
[28] Sauvet, A.L., Fouletier, J., *Electrochim. Acta.* **47**, 987 (2001).
[29] Primdahl, S., Hansen, J.R., Grahl-Madsen, L., Larsen, P.H., *J. Electrochem. Soc.* **148**, A74 (2001).
[30] Liu, J., Madsen, B.D., Ji, Z.Q., Barnett, S.A., *Electrochem. Solid State Lett.* **5**, A122 (2002).
[31] Akin, F.T., Lin, Y.S., *AIChE J.* **48**, 2298 (2002).
[32] Platon, C.E., Thomson, W.J., *Ind. Eng. Chem. Res.* **41,** 6637 (2002).
[33] Marina, O.A., Canfield, N.L., Stevenson, J.W., *Solid State Ionics* **149**, 21 (2002).
[34] Meyer, R., Waser, R., Helmbold, J., Borchardt, G., *J. Electroceram.* **9**, 101 (2002).
[35] Hui, S.Q., Petric, A., *Solid State Ionics* **143**, 275 (2001).
[36] Lashtabeg, A., Irvine, J.T.S., Feighery, A.J., *Ionics* **9**, 220 (2003).
[37] Koide, H., Someya, Y., Yoshida, T., *Solid State Ionics* **132**, 253 (2000).
[38] Kim, J., Fung, K., Virkar, A.V., US Patent 6,228,521, 2001.
[39] Simwonis, D., Tietz, F., Stover, D., *Solid State Ionics* **132**, 241 (2000).
[40] Hammou, A., Guindet, J., "The CRC Handbook of Solid State Electrochemistry," (P.J. Gellings and H.J.M. Bouwmeester, Eds.) p. 419, CRC Press, Boca Raton, 1997.
[41] Lu, C., Worrel, W.L., Vohs, J.M., Gorte, R.G., *J. Electrochem. Soc.* **150**, A1357 (2003).
[42] Lee, I.S., Ahn, K., Vohs, J.M., Gorte, R.J., *J. Electrochem. Soc.* **151**, A1319 (2004).
[43] McIntosh, S., Gorte, R.J., *Chem. Rev.* **104**, 4845 (2004).
[44] Finnerty, C.M., Coe, N.J., Cunningham, R.H, Ormerod, R.M., *Catal. Today* **46**, 137 (1998).

[45] Srilomsak, S., Schilling, D.P., Anderson, H.U., "Proceedings of the 1st International Symposium on Solid Oxide Fuel Cells," (S.C. Singhal, Ed.) p. 129, The Electrochemical Society, New Jersey, 1989.
[46] Ying, J.Y., Tschöpe, A., *Chem. Eng. J.* **64**, 225 (1996).
[47] Trudeau, M.L., Tschöpe, A., Ying, J.Y., *Surf. Interface Anal.* **23**, 219 (1995).
[48] Vashook, V., Vashook, V., Vasylechko, L., Knapp, M., Ullmann, H., Guth, U., *J. Alloy. Compd.* **354**, 13 (2003).
[49] Moos, R., Hardtl, K.H., *J. Am. Ceram. Soc.* **80**, 2549 (1997).
[50] Trimm, D.L., *Catal. Rev.* **16**, 155 (1977).
[51] Trimm, D.L., *Catal. Today* **49**, 3 (1999).
[52] Ghosh, G., *Metall. Mater. Trans. A* **30**, 1481 (1999).
[53] Mukhopadhyay, A.K., Mitra, P., Chatterjee, A.P., Maiti, H.S., *J. Mater. Sci. Lett.* **17**, 625 (1998).
[54] Itoh, H., Yamamoto, T., Mori, M., Horita, T., Sakai, N., Yokokawa, H., Dokiya, M., *J. Electrochem. Soc.* **144**, 641 (1997).
[55] Robert, G., Kaiser, A., Batawi, E., "Proceedings of the 6th European Solid Oxide Fuel Cell Forum," p. 193, European Fuel Cell Forum, Switzerland, 2004.
[56] Muller, A.C., Herbstritt, D., Tifflee, E.I., *Solid State Ionics* **152**, 537 (2002).
[57] Gorte, R.J., Park, S., Vohs, J.M., Wang, C., *Adv. Mater.* **12**, 1465 (2000).
[58] J. Sweeney, "Novel Metal Oxide Nanocomposites for Oxygen Storage, Sulfur Dioxide Adsorption and Hydrogen Sulfide Absorption," Ph.D. Thesis, Massachusetts Institute of Technology, 2003.
[59] Atkinson, A., Guppy, R.M., *J. Mater. Sci.* **26**, 3869 (1991).
[60] Zou, H., Lin, Y.S., Rane, N., He, T., *Ind. Eng. Chem. Res.* **43**, 3019 (2004).
[61] Woodhead, J.L., US Patent 3,761,571, 1973.
[62] Weiss, S., Ying, J.Y., to be submitted.
[63] Reed, J.S., "Introduction to the Principles of Ceramic Processing," p. 148, John Wiley & Sons, New York, 1988.
[64] Bard, A.J., Faulkner, L.R., "Electrochemical Methods, Fundamentals and Applications," p. 808, Wiley, New York, 2001.
[65] Park, S., Gorte, R.J., Vohs, J.M., *J. Electrochem. Soc.* **148**, A443 (2001).
[66] Kleinlogel, C.M., Gauckler, L.J., *J. Electroceram.* **5**, 231 (2000).
[67] Kim, H., Park, S.D., Vohs, J.M., Gorte, R.J., *J. Electrochem. Soc.* **148**, A693 (2001).
[68] McIntosh, S., Vohs, J.M., Gorte, R.J., *J. Electrochem. Soc.* **150**, A470 (2003).
[69] Wang, C., Worrell, W.L., Park, S., Vohs, J.M., Gorte, R.J., *J. Electrochem. Soc.* **148**, A864 (2001).

Chapter 5 – Conclusions and Recommendations for Future Work

5.1. Conclusions

This thesis was focused on materials development for emerging fuel cell technologies. For PEM fuel cell applications, a microreactor system was designed with novel catalysts and Pd membrane for hydrogen generation and purification. Highly active La-based perovskite catalysts were created for the autothermal oxidative conversion of methanol to hydrogen. The new catalyst and reaction scheme avoided the use of pyrophoric copper and expensive noble metal catalysts. CO-free hydrogen generation was successfully achieved on the micro-scale with the use of Pd membrane.

For micro-solid oxide fuel cells, thin electrode films were processed by adapting catalyst wash-coat technologies. To promote low-temperature adhesion to the support, we have developed inorganic binders that could form the relevant oxides for SOFC applications upon calcination. Oxide films that adhered well to the support were successfully produced at temperatures as low as 400°C, but they did not provide for sufficiently high electrical conductivity. As an alternative, porous noble metal films were developed for cathode applications. By etching away the Ni porogen, thin Pt films were successfully attained with ultrafine pores. A porous polymer template was also developed to assist porous film deposition by sputtering.

Lastly, novel anode materials were examined for direct hydrocarbon SOFC applications. Particular noteworthy was the development of Ni-Sn/YSZ cermet, which could be easily fabricated into an anode-supported architecture using conventional ceramic processing techniques. The use of a Ni-Sn alloy instead of Ni prevented the formation of crystalline carbon, and provided for long-term dimensional stability in dry methane at 800°C. Significant power outputs that were comparable to other direct hydrocarbon SOFC systems were attained by this novel cermet anode. Further advances could be expected with additional improvements in materials processing.

5.2. Recommendations for Future Work

In Chapter 2, non-noble metal catalysts were developed that could sustain the autothermal methanol partial oxidation to hydrogen. However, when applied to the

microreactor system, autothermal conversion was not achieved. Additional work needs to be conducted to redesign the microreactor to incorporate more catalysts and to include side-wall insulation. Further catalyst development should be devoted towards the partial oxidation of hydrocarbon fuels that have significant vapor pressures, such as propane and butane.

In Chapter 3, the development of electrode materials was significantly hindered by the poor mechanical stability of ultrathin YSZ electrolytes. This would likely remain a major obstacle, and it is recommended that future research be directed towards protonic ceramic fuel cells (PCFC). PCFC is a subset of SOFC whereby protons instead of oxy-anions are conducted through the ceramic matrix. In PCFC, dense Pd membranes can be used as the anode. As the Pd membrane reactor has shown great mechanical stability, it would serve well as the fabrication platform. The electrolyte could then be deposited on the dense Pd surface by using semiconducting processing or sol-gel processing (as described in Chapter 2) [1].

The Ni-Sn/YSZ system was developed in Chapter 4 for anode-supported SOFC applications. This material is worthy of further optimization studies. For example, the current anode structure is quite dense. Porosity may be introduced using the carbon black technique developed for the all-ceramic anodes described in Section 4.3.2. The YSZ particle size should be kept fine to prevent alloy agglomeration during reduction. The effect of ceria addition should also be explored. Ceria is one of the best carbon combustion catalysts, and has been examined for diesel soot combustion applications [2]. It may further increase the coke tolerance of the anode catalyst, and provide for a higher overall power density.

Lastly, for further improvements on SOFC designs, it would be important to develop better cathode systems. For example, ultrafine lanthanum strontium manganate (LSM) can be prepared by chemical precipitation for use with YSZ. Microstructural effects are relatively easy to retain in the cathode compared to the anode due to the lower firing temperature involved. Utilization of high surface area, nanostructured cathode materials may further decrease the required firing temperatures. The activity of the cathode system may also be increased by impregnating the LSM scaffold with active species such as cobalt and nickel. The combination of microstructural control and

activity control would likely lead to significant improvements in the cathode performance.

5.3. References

[1] Yamaguchi, S., Yamamoto, S., Shishido, T., Omori, M., Okubo, A., *J. Power Sources* **129**, 4 (2004).

[2] Makkee, M., Jelles, S.J., Moulijn, J.A., "Catalysis by Ceria and Related Materials," (A. Trovarelli, Ed.) p. 391, Imperial College Press, London, 2002.